

FLOW PATTERNS AND WALL SHEAR RATES IN A  
SERIES OF SYMMETRIC BIFURCATIONS

FLOW PATTERNS AND WALL SHEAR RATES IN A  
SERIES OF SYMMETRIC BIFURCATIONS

By

OSAMA A. A. ELMASRY B.Sc. (Eng.)

A Thesis

Submitted to the Faculty of Graduate Studies

in Partial Fulfilment of the Requirements

for the Degree

Master of Engineering

McMaster University

April 1974

TITLE: FLOW PATTERNS AND WALL SHEAR RATES IN  
A SERIES OF SYMMETRIC BIFURCATIONS

AUTHOR: Osama A. A. ELmasry  
B.Sc. (Eng.), Alexandria University,  
Egypt.

SUPERVISORS: Dr. G. F. Round, Dr. I. A. Feuerstein

NUMBER OF PAGES: xiii, 123

SCOPE AND CONTENTS:

This study investigates the flow patterns and wall shear rate distributions downstream from a series of three glass model symmetric bifurcations, typical of the blood vessels in man. The models have a single included angle of  $75^{\circ}$  and total output to input flow area ratios of 0.75, 1.02 and 1.29, covering the physiological range. The Reynolds numbers studied (based on parent tube) were 400, 800 and 1200 in steady flow.

Local fluid velocities were obtained at a number of axial positions along the bifurcation daughter tube via a neutrally buoyant tracer particle technique utilizing cine photography. This provided sufficient information to determine the three velocity components for each particle. The tangential and radial components were in general less than 6% of the mean axial velocity. In the case of the axial components, an analytical representation of the velocity in polar coordinates was obtained. This analytical function permits evaluation of wall shear rate distribution.

The velocity profiles were found to be symmetric with respect to the plane of the bifurcation. At two diameters downstream from the carina the velocity profiles in the plane of the bifurcation showed a high peak near the inside wall of the branch. With distance downstream the peak was convected tangentially evening out the profile towards an axially symmetric mountain plateau with a dished top.

Wall shear rate as a function of  $\theta$  at constant axial position was represented by displaced cosine function. The highest shear rates always occurred on the inside wall of the daughter tube and the lowest on the outside wall. In general, the largest deviation from developed shear rates occurred close to the carina.

The largest positive deviation in wall shear rate from developed values was found in the small area ratio bifurcation and the lowest wall shear rate value was found in the large area ratio bifurcation ( $\alpha = 1.29$ ) indicating possible flow separation near the carina. The biological implications of the shear rate information generated are discussed.

## TABLE OF CONTENTS

		PAGE
	List of Tables	vi
	List of Figures	vii
	List of Plates	viii
	Nomenclature - Branch Notation	xi
	Acknowledgements	xiii
CHAPTER 1	INTRODUCTION	1
1.1	General	1
1.2	Literature Review	2
CHAPTER 2	EXPERIMENTAL APPROACH AND RATIONALE	5
2.1	Parameter Definition	5
2.2	Branch Geometry	7
2.3	Fluid Velocity Measurement	9
CHAPTER 3	EXPERIMENTAL APPARATUS AND PROCEDURE	13
3.1	Experimental Apparatus	13
3.2	Experimental Procedure	28
3.3	Film Analysis	30
CHAPTER 4	RESULTS	34
4.1	Velocity Profiles	34
4.2	Wall Shear Rate	60
CHAPTER 5	ANALYSIS AND DISCUSSION	70
5.1	Axial Velocity Development	70
5.2	Wall Shear Rate Distribution	78
5.3	Biological Discussion	86

	PAGE
CHAPTER 6 CONCLUSIONS	90
REFERENCES	92
APPENDIX 1 Parent Tube Velocity Profile	94
APPENDIX 2 Error Analysis	97
APPENDIX 3 Tabulated Experimental Data	99

## LIST OF TABLES

			PAGE
TABLE	1	Dimensions of Glass Model Tubes	8
TABLE	2	Properties of Suspending Fluid Components	14
TABLE	3	Experimental Identification	31
TABLE	4	Experimental Operating Parameters	34
TABLE	5	Mean Value and Standard Deviations for $V_{\theta}^+$ and $V_r^+$	37
TABLE	6	Parameter Estimation (Outer Boundary Region)	40
TABLE	7	Parameter Estimation (Central Core Region)	43
TABLE	8	Values of $\frac{(V_m)_c}{V_m}$	61
TABLE	9	Coefficients of Shear Rate Equations	63
TABLE	10	Developed Wall Shear Rate Values	79
TABLES	11-24	Velocity Data for Experiments	100

## LIST OF FIGURES

		PAGE
FIGURE 1	Refractive Index-Temperature Curve for Suspending Fluid	16
FIGURE 2	Viscosity-Temperature Curve for Suspending Fluid	17
FIGURE 3	Schematic Diagram of Flow System	19
FIGURE 4	Flowmeter Calibration Curve	21
FIGURE 5	Hycam Speed Curve	27
FIGURE 6	Film Analysis	33
FIGURES 7-21	Non-dimensional Velocity Profiles	45
FIGURES 22-26	Wall Shear Rate Distributions around the Daughter Tube	65
FIGURES 27-31	Axial Velocity Development	71
FIGURES 32-36	Longitudinal Wall Shear Rate Distributions	80
FIGURE 37	Velocity Profiles in the Parent Tube	96

## LIST OF PLATES

			PAGE
PLATE	1	Front View of Symmetrical Bifurcation Model	10
PLATE	2	Side View of Symmetrical Bifurcation Model	11
PLATE	3	Viewing Cell	23
PLATE	4	Front Surface Reflecting, Mirror Positioned Parallel to Daughter Tube	25

## NOMENCLATURE

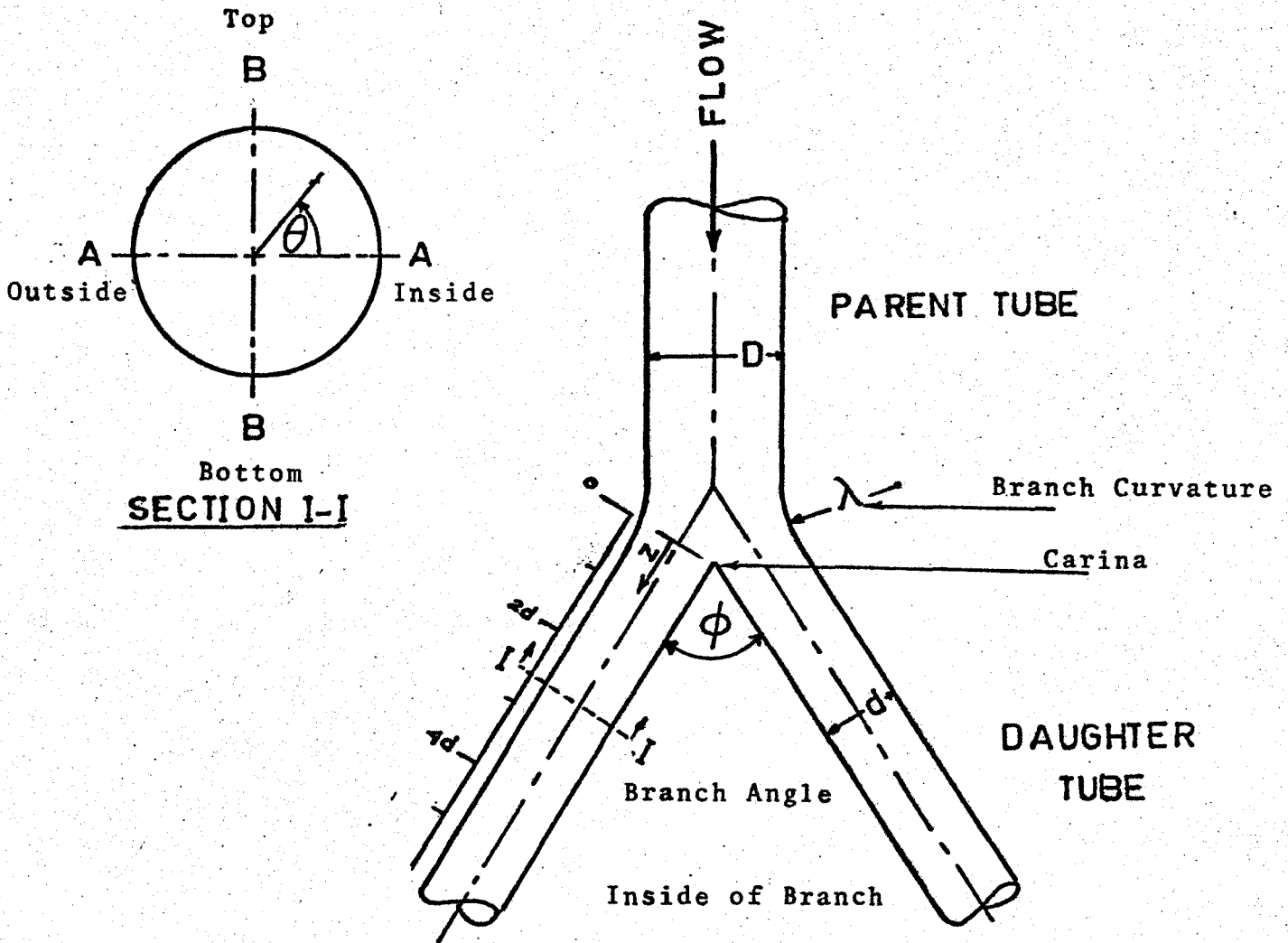
### DIMENSIONAL

$r$	radial coordinate
$\theta$	tangential coordinate
$z$	axial coordinate
$R$	daughter tube radius
$d$	daughter tube diameter
$D$	parent tube diameter
$V_m$	mean fluid velocity
$(V_m)_c$	calculated mean fluid velocity
$V_r$	radial velocity component
$V_\theta$	tangential velocity component
$V_z$	axial velocity component
$Z$	distance from the carina
$Q_d, Q_D$	volumetric flow rate in daughter and parent tube respectively
$\mu$	dynamic viscosity
$n$	refractive index
$\Delta r$	radial displacement
$\Delta s$	tangential displacement
$\Delta z$	axial displacement
$\Delta T$	time increment
$\lambda$	branch curvature
$\phi$	branch angle
$\dot{\omega}$	shear rate

## NON-DIMENSIONAL

$\alpha$	total-output to input flow area ratio, $2d^2/D^2$
$d/D$	diameter ratio
$Re_N$	Reynolds number based on mean fluid velocity in parent tube
$(Re_N)_d$	Reynolds number based on mean velocity in daughter tube
$Z/d$	non-dimensional distance from the carina
$\eta$	non-dimensional radial coordinate, $r/R$
$V_r^+$	non-dimensional radial velocity, $V_r/V_m$
$V_\theta^+$	non-dimensional tangential velocity, $V_\theta/V_m$
$V_z^+$	non-dimensional axial velocity, $V_z/V_m$

# BRANCH NOTATION



With reference to the figure above, the inlet tube is known as the parent tube and each of the diverging tubes are known as daughter tubes. The angle between the two daughter

tubes is the branch angle  $\phi$  and the region between the two daughter tubes is the inside of the branch. The apex of the branch, where the two daughter tubes meet, is known as the carina. The outside curvature of the branch is the branch curvature ( $\lambda$ ).

Looking at the daughter tube, the longitudinal distance  $Z$  is measured from the carina downstream. Plane A-A is the bifurcation plane ( $\theta=0, \pi$ ) and Plane B-B is the plane normal to the bifurcation plane ( $\theta = \frac{\pi}{2}, \frac{3\pi}{2}$ ).

## ACKNOWLEDGEMENTS

The author expresses his gratitude to his supervisors Dr. I. A. Feuerstein and Dr. G. F. Round for their invaluable advice and constant encouragement throughout this work.

Appreciation is also expressed for the help given by the Chemical Engineering technicians in constructing the experimental apparatus.

Thanks are due to Ms. BettyAnne Bedell for her expert typing of the manuscript.

Financial support from the National and Medical Research Councils of Canada is sincerely appreciated.

# CHAPTER I

## INTRODUCTION

### 1.1. General

Studies of the flow of viscous fluids in circular, branched tubes are of increasing importance in connection with studies of blood flow in the human cardiovascular system. The blood flowing in the system travels through a large number of bifurcations. A fundamental understanding of the mechanism of bifurcation flows is of importance to understand the defects and diseases of the cardiovascular system.

Several workers have indicated that fluid mechanics in general and wall shear rate in particular may be determining factors in early atheromatic plaque formation. Atherosclerosis is defined as hardening and narrowing of the inside wall of blood vessels caused by deposition of a fatty material known as atheroma. The accumulation of such deposits reduces the flow of blood in the vessels affected and can lead to very detrimental effects in organs and tissues supplied. The fluid dynamic effect on the formation of atheromatic plaques is given support by the fact that early plaques generally occur at sites of curvature and branches, however, the fluid dynamic processes which may help deposits to form are not as yet defined.

Because of the extremely complicated nature of flow in branches, the problem is relatively unsolved. This work

has been undertaken in order to provide some detailed analysis of the velocity field and wall shear rate distribution in bifurcations which are a particular type of branch geometry.

## 1.2. Literature Review

Very little detailed study of the flow in branches has been made. Knox, 1962 (1) has investigated the pressure drop downstream of side branches and has studied the effect of branch angle and area ratio on the developed flow recovery lengths. Schroter and Sudlow, 1969 (2) have studied the axial velocity profiles downstream of several bifurcation junctions using a hot-wire anemometer. The motivation for their work was to understand the mechanism of lung function and the effect of bifurcation geometry on lung air flow. In 1970, Pedley et al. (3) used these velocity profiles to estimate the viscous dissipation in branched vessels and to predict the pressure drop within the human bronchial airways.

In order to understand the mechanism of atheromatic deposit formation some workers have proposed a relationship between fluid mechanics of blood flow in bifurcations and the formation of such deposits. Fox and Hugh, 1966 (4) have suggested that boundary layer separation may help in forming these deposits. Mitchell and Schwartz, 1965 (5) have implicated turbulence as being causative. Caro et al. (6) have shown that the distribution of early atheroma in man is coincident with those regions in which arterial wall shear rate is expected

to be relatively low. They have suggested that the development of atheroma is associated with shear dependent mass transport. Such a correlation is inconsistent with the proposals made by other workers [French, 1970 (7) and Texon, 1960 (8)] who believe that plaques occur in high shear regions. In 1970, Brech (9) studied experimentally the velocity profiles and shear stress downstream of the branch carina in one particular shape of symmetrical bifurcation (area ratio = 1.15 and branch angle = 90°). He used a specially designed hot-film anemometer to obtain both the local axial velocity and wall shear rate.

Analytical approaches to the problem have been recently carried out by Lew (10), (11), (12). He has solved the Navier-Stokes equations for the case of two-dimensional flow with low Reynolds number and zero bifurcation angle. Lynn et al., 1972 (13) have computed stream functions and vorticity profiles for two-dimensional branching flow. Zamir and Roach, 1973 (14) have solved the two-dimensional Navier-Stokes equations for high Reynolds number flow in a zero bifurcation angle system. In general, the velocity profiles obtained from these analytical solutions do not show the multiple peaks and inflection points of the velocity profiles obtained experimentally by Schroter and Sudlow (2) and Brech (9). This could be attributable to the simplifications incorporated into these analytical models.

In the present work a detailed analysis of steady flow in a series of symmetrical bifurcations has been carried

out using rigid-walled glass models, typical of the blood vessels in man. The parameters under investigation were Reynolds number and total-output to input flow area ratio. A detailed study of the velocity field downstream of the carina has been done via a tracer particle technique. Wall shear rate distributions at a number of stations along the bifurcation daughter tube have also been obtained.

## CHAPTER 2

### EXPERIMENTAL APPROACH AND RATIONALE

#### 2.1. Parameter Definition

Many geometric and flow parameters affect the flow patterns within a branch. In this work, effects of Reynolds number and cross-sectional area ratio on the velocity field and wall shear rate distribution have been studied. This study has been carried out at a number of stations along the bifurcation daughter tubes. Flow was always fully-developed with parabolic profile upon entering the bifurcation region from the parent tube.

##### 2.1.1. Reynolds Number ( $Re_N$ )

Reynolds number is a non-dimensional index of the ratio of inertial to viscous forces acting on a moving fluid. In all experiments conducted in this work, Reynolds number is based upon conditions in the parent tube upstream of the carina. The physiological range of Reynolds number in large arteries is (140-1900), [Whitmore (15)]. This range is based on a blood viscosity of 3.5-5.4 centipoise, blood density of 1.048-1.066 gm./cm<sup>3</sup>, vessel diameter of .4-2.1 cm and blood mean velocity of 18-30 cm/sec. Three Reynolds numbers of 400, 800 and 1200 have been selected covering a wide portion of the physiological range, to examine the effect of

Reynolds number on the velocity field and wall shear rate distribution in the daughter tubes.

### 2.1.2. Area Ratio ( $\alpha$ )

Branch area ratio is defined as the ratio of the combined cross-sectional area of daughter tubes to the cross-sectional area of the parent tube. Caro et al. (6) have measured the diameters of the parent and daughter arteries at 45 junctions in man and have given values for  $\alpha$  in the range of (0.52-1.39). It was therefore appropriate to select three values of 0.75, 1.02 and 1.29 for the area ratios to be studied. These three values are representative of the physiological range.

### 2.1.3. Branch Angle ( $\phi$ )

Branch angle is defined as the angle between the two daughter tubes. Measurement of the branch angle in man presents considerable difficulty since blood vessels frequently curve sharply after branching, and no detailed work on this aspect appears to have been published. Schroter and Sudlow (2) have chosen an angle of 70 degrees for their symmetric branch models and Brech (9) has used a 90 degree branch angle in his investigation. A value of 75 degrees was therefore chosen as a compromise and maintained constant for all the three experimental models.

#### 2.1.4. Branch Curvature ( $\lambda$ )

Branch curvature is the outside curvature of the branch joining the parent tube with each daughter tube. Its value is potentially important with respect to possible flow separation. A value of  $\lambda$  equal to the upstream tube diameter (D) has been selected and kept constant for all three branch models used in this study.

#### 2.1.5. Flow Division Ratio

Flow in any branching system can be divided from all flow in one daughter tube to all flow in the other daughter tube. This depends upon the needs of the downstream systemic circulations. It was decided to use equally divided flow since this case is representative and easily controllable.

#### 2.2. Branch Geometry

Three symmetrical bifurcation models were blown by an expert glass blower from Pyrex glass. These models have a sharp carina and rounded transition region indicative of the aortic bifurcation. The area ratios and diameter ratios for the three models are given in Table 1. These values were calculated from the tube internal diameters measured with the aid of a vernier caliper at the end of each tube. The internal diameters of both the daughter and parent tubes were also determined photographically. The tubes were found to be of uniform diameter.

MODEL	I	II	III
Mean Inner Diameter of Parent Tube, D(cm)	1.867	1.867	1.867
Mean Inner Diameter of Daughter Tube, d(cm)	1.501	1.339	1.142
Diameter Ratio (d/D)	.80	.71	.61
Area Ratio (output area/input area)	1.29	1.02	.75

Table 1. Dimensions of Glass Model Tubes

Special care was taken to ensure that the bifurcation models were symmetric and that the flowrate in the parent tube was divided equally between the two daughter tubes. An independent test in an open system was carried out, for each of the three models, to check the flow division as a measure of symmetry. The individual daughter tube flowrates were measured with the aid of a stopwatch and two large graduated cylinders. Values obtained in this way were within 3% of those values expected. Thus it may be concluded that the three models were suitably symmetric.

The region of experimental interest extended from the branch carina to a position six daughter tube diameters downstream. Three lines were marked on the daughter tube at  $Z/d$  equal to 2, 4 and 6. These lines located the three positions selected for study.

The three models with area ratio .75, 1.02 and 1.29 were given the identifying codes I, II and III respectively. Plates 1 and 2 show front view and side view of one of these models (Model III,  $\alpha = 1.29$ ).

### 2.3. Fluid Velocity Measurement

There are many techniques available for measuring local point velocities of fluids in motion. Spinning vanes, the pitot tube, hot-wire anemometer and laser doppler techniques may be used under certain circumstances for measuring local velocities.

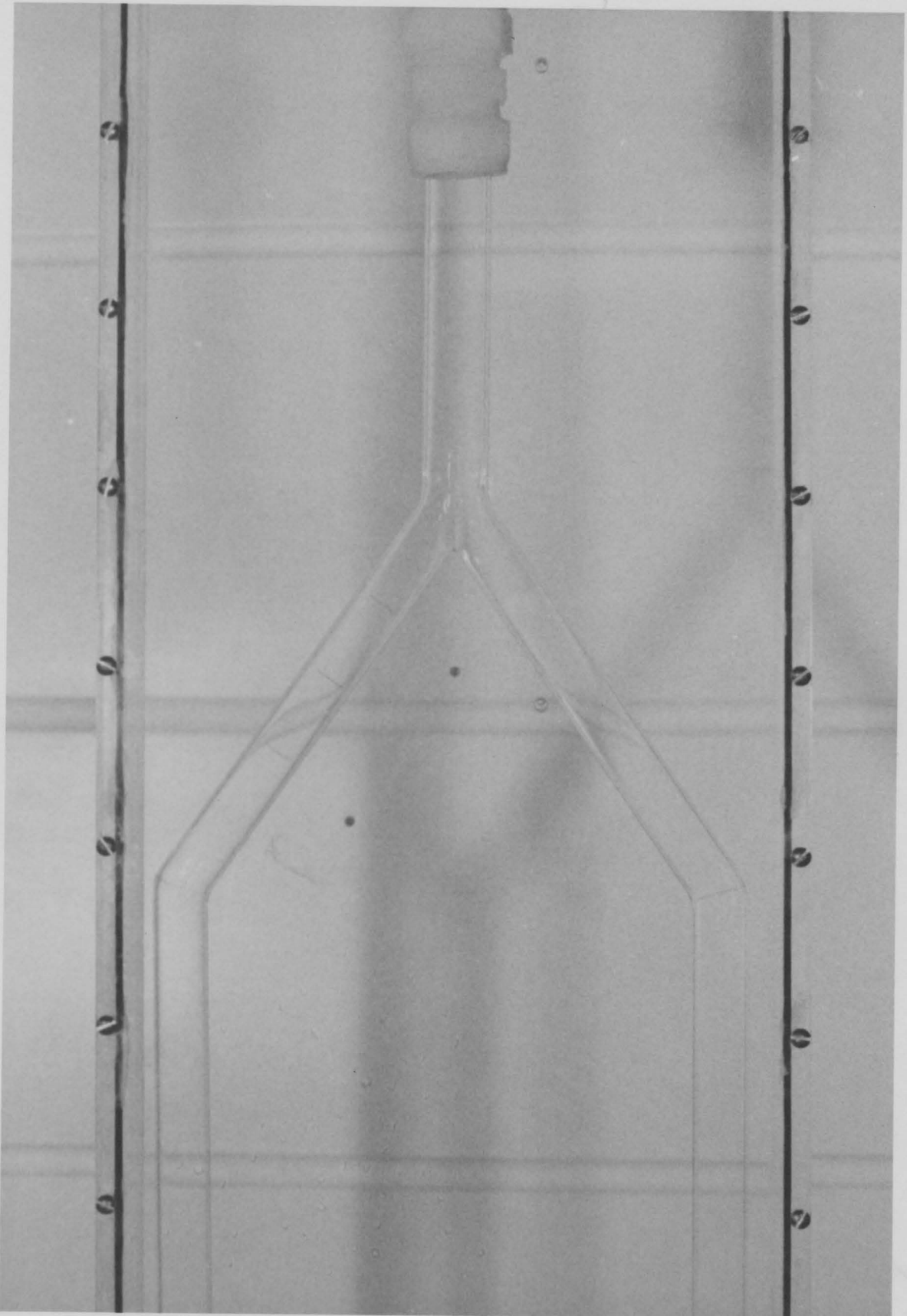


Plate 1. Front View of Symmetrical Bifurcation Model  
(Area Ratio = 1.29)

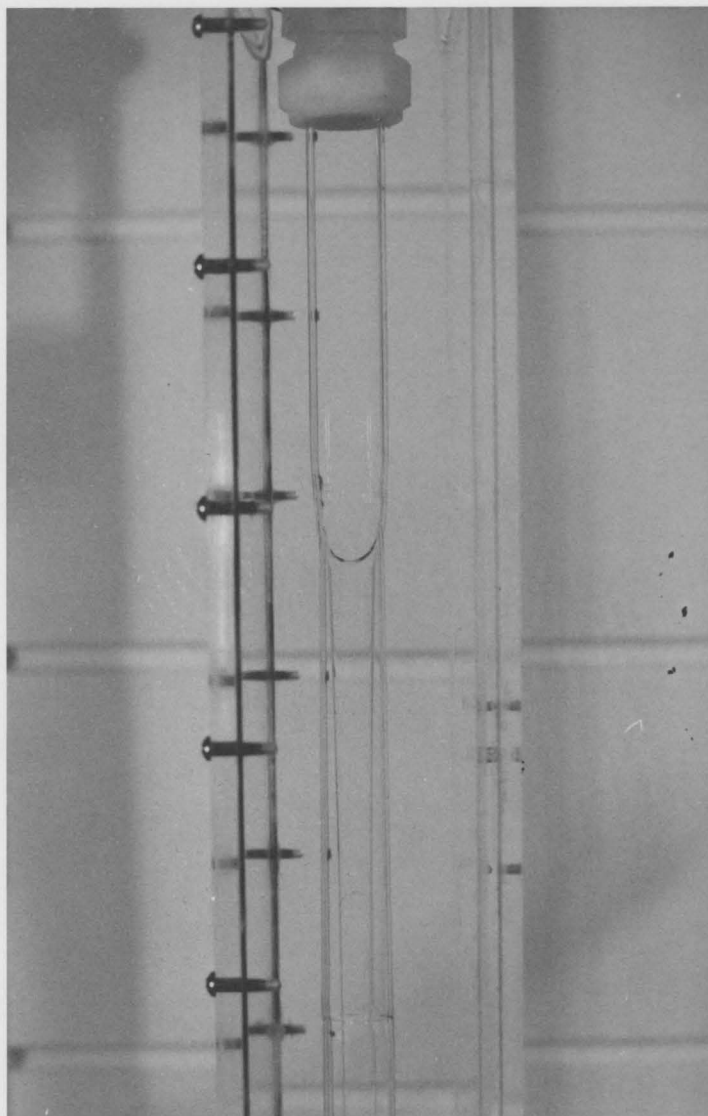


Plate 2. Side View of Symmetrical  
Bifurcation Model  
(Area Ratio = 1.29)

Neutrally bouyant tracer particles are very useful in the construction of fluid streamlines and for obtaining local velocity profiles. This technique has the capability of obtaining local velocity components for complicated flows.

Goldsmith (16) has measured the local velocity profile in concentrated suspensions of red cell ghosts using normal red blood cell tracers. Knowles et al. (17) used the same technique to define velocity profiles within a hydrocyclone. For this application an anisole-water suspension system was used and individual point velocity components were obtained. Pike (18) has developed the technique and used it to study the flow patterns generated by an abrupt expansion in a circular section conduit.

In order to use neutrally buoyant particles as tracers in complex flows, one must determine if these particles can be considered to be replacements for the fluid. In fact, the ratio of particle radius to tube radius and the ratio of particle radius to distance from the tube wall are important dimensionless groups for describing the deviation between particle velocities and fluid velocities. Feuerstein and Woods (19) have shown that results which do not vary with particle size do not contain errors due to the presence of particles, assuming a particle-size ratio of at least 2. Using particle sizes (100-300  $\mu$ ) in tube radius of 1 cm., Pike (18) has shown that particle inertia effect was negligible for the range of Reynolds number (200-750).

CHAPTER 3  
EXPERIMENTAL APPARATUS  
AND PROCEDURE

3.1. Experimental Apparatus

The experimental apparatus was designed to provide for continuous steady flow of fluid suspension through the branch model. This permits the evaluation of three dimensional velocity components of the flow in the daughter tube via high-speed photography of neutrally buoyant tracer particles suspended in the circulating fluid.

3.1.1. Fluid Suspension

The composition and properties of the suspending fluid components are given in Table 2. This type of solution was used by Pike (18). These properties have been adjusted to provide for:

- (a) Neutral buoyancy of the suspended particles
- (b) Minimal optical distortion of the particles being photographed
- (c) A suitable Reynolds number range (400-1200)

The suspending fluid contained particles of polystyrene whose size was (100-300  $\mu$ ). The particle concentration in the suspension was kept to be less than 3 particles per  $\text{cm}^3$ . The suspending fluid density was adjusted to that of the

	Specific Gravity	Refractive Index	Normal Boiling Point (°C)	Percentage Composition by Volume
Benzyl Alcohol	1.045	1.5387	204.	56%
Ethylene Glycol	1.111	1.4321	198.	20%
Water	1.000	1.3330	100.	20%
N-Amyl Alcohol	0.817	1.4101	137.75	4%

Table 2. Properties of Suspending Fluid Components (at 20°C).

polystyrene particles ( $1.042 \text{ gm./cm}^3$ ) by the addition of n-amyl alcohol. No sedimentation was observed for samples of the suspension at a temperature of  $20^\circ\text{C}$  for a period of 24 hours.

The refractive index of the suspending fluid (Figure 1) was adjusted to be within  $\pm .002$  refractive index units of the refractive index of glass ( $n_g = 1.474$ ). This enabled optical distortion by refraction (the lens effect) to be minimized. More exact matching was not necessary since it was desired to define the tube wall.

The suspending fluid viscosity is given (Figure 2) over a temperature range of ( $16\text{-}24^\circ\text{C}$ ).

### 3.1.2. Flow System

A schematic diagram of the flow system is given in Figure 3. The main components are:

- (a) Motor-pump unit
- (b) Flow meter
- (c) Mixing chamber
- (d) Viewing cell
- (e) Pulsation damper

#### (a) Motor-Pump Unit

A positive displacement Moyno type SSF pump was used to handle the solid/liquid suspension. The pump was driven by a  $1/2$  h.p.-D.C. motor with a 110 volt SCR speed control. To avoid pump corrosion or contamination of fluid,

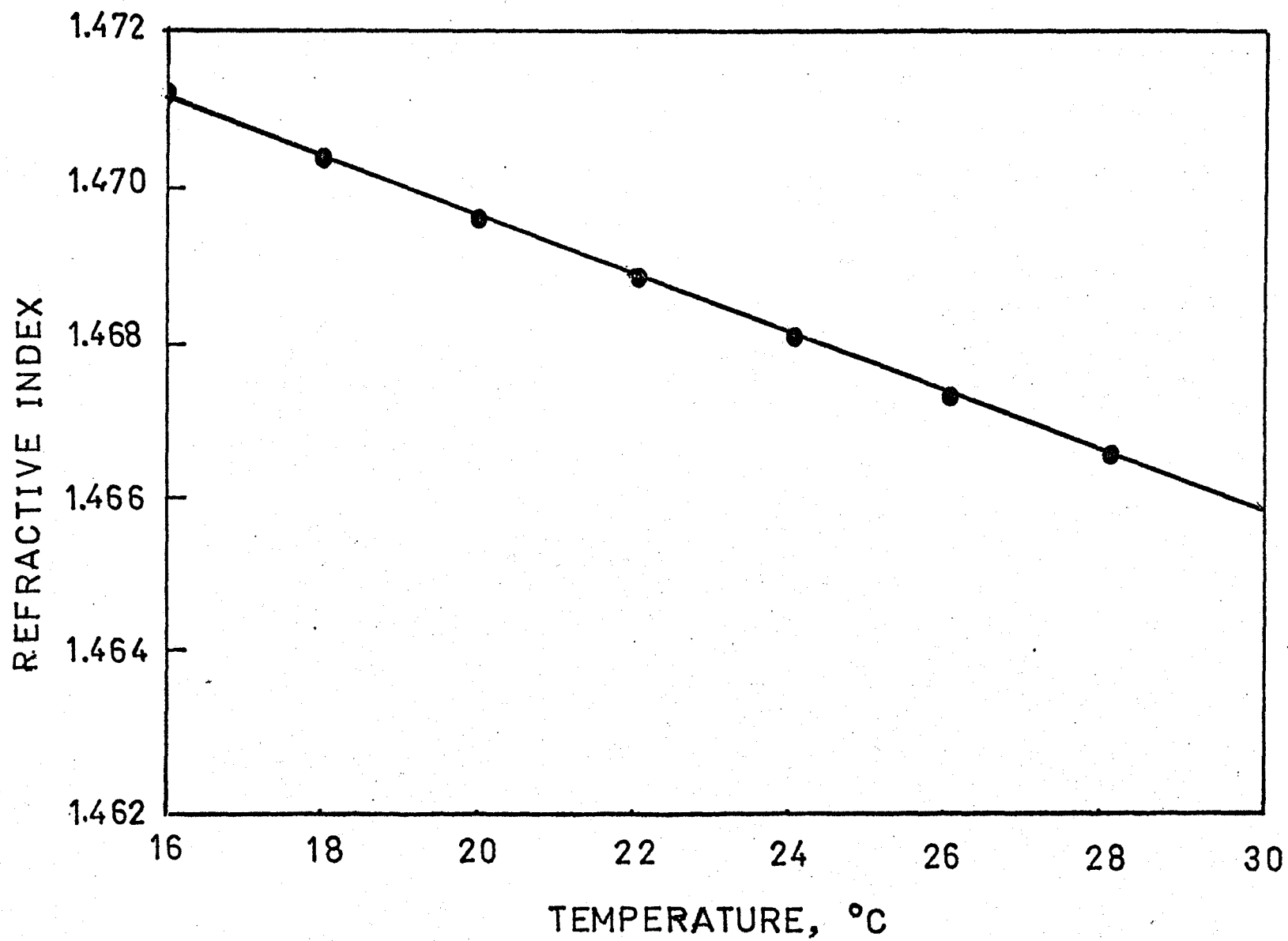


Figure 1. Refractive Index-Temperature Curve for Suspending Fluid.

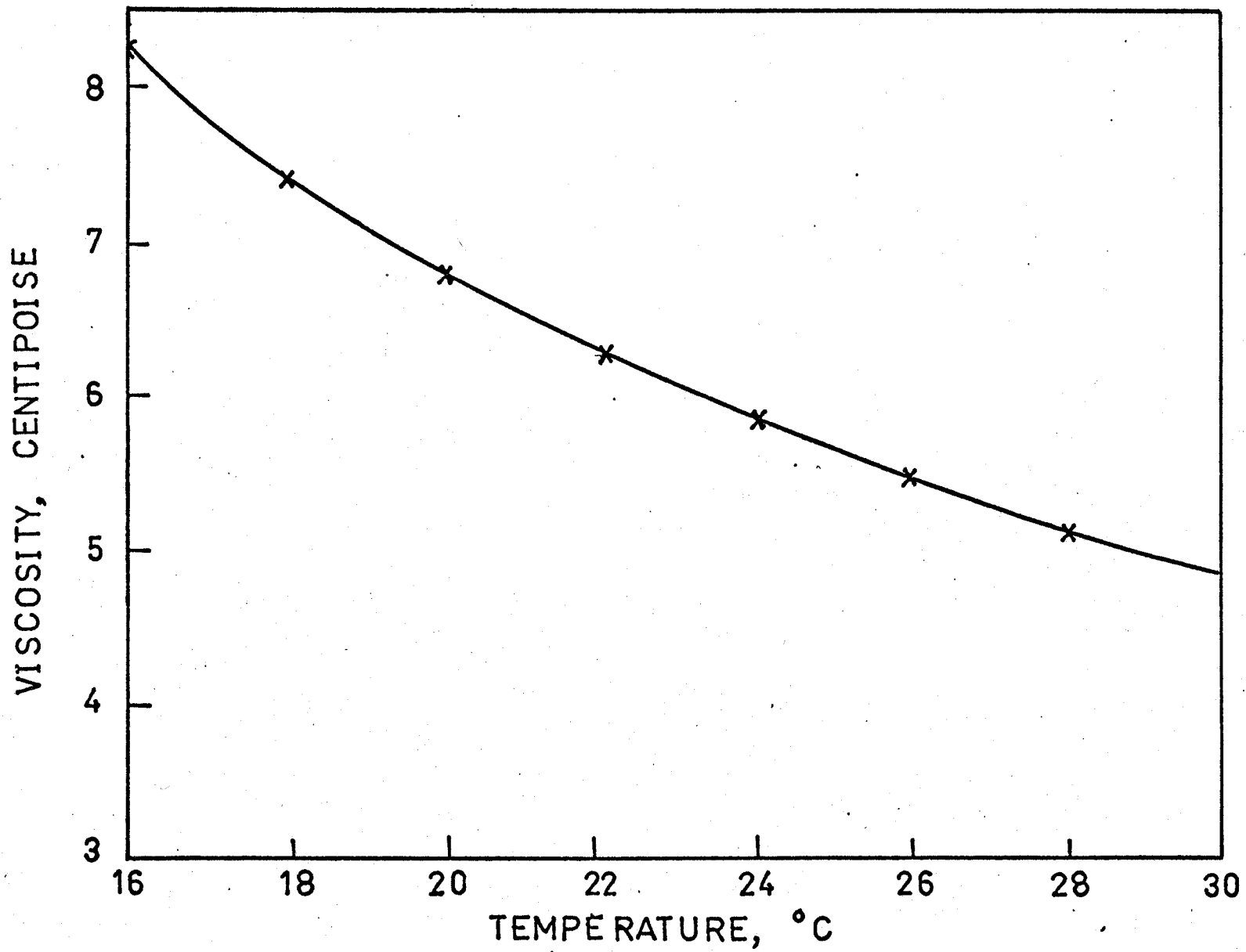


Figure 2. Viscosity-Temperature Curve for Suspending Fluid.

## DESCRIPTION OF SYMBOLS USED IN FIGURE 3

A	Motor
B	Pump
C	Speed control
D	Venturimeter
E	Double U-tube manometer
F	QVF thick wall glass tubing
G	Mixing chamber
H	Viewing cell
I	Branch model
J	Steel table
K	Downstream tank
M	Mercury manometer

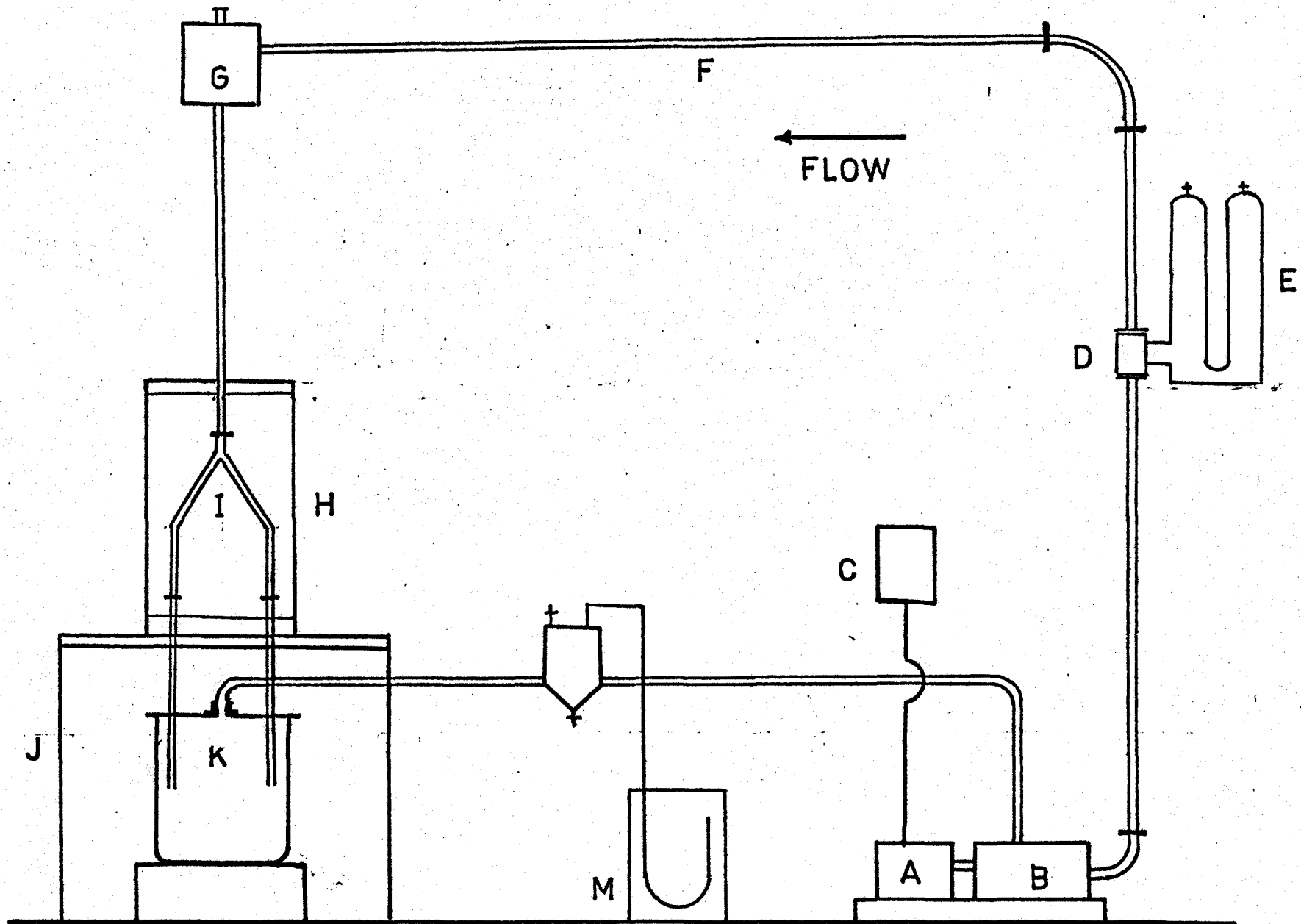


Figure 3. Schematic Diagram of Flow System.

the stator and rotor were constructed of viton and stainless steel respectively.

(b) Flowmeter

An aluminum venturimeter was inserted in the circuit to measure the flowrate. It was used in conjunction with a double U-tube manometer which had two air columns of equal length separating the manometer fluid (water) from the circulating fluid. A detailed construction drawing of the flowmeter can be found in Pike (18). The flowrate ( $\text{cm}^3/\text{sec.}$ ) as a function of the manometer head ( $\text{cm. H}_2\text{O}$ ) is given in Figure 4. This curve gives the theoretical flowrate (from continuity and the Bernoulli equations) for a venturimeter with a throat to main diameter ratio of 0.303. An independent calibration was carried out using water (specific gravity 1.00 c.f. 1.04 for suspending fluid) in an open system, the flowrate being measured with the aid of a stopwatch and a graduated cylinder. Values obtained in this way were within 3% of the theoretical values. A check was also made photographically (Appendix 1).

(c) Mixing Chamber

In order to provide homogeneous mixing of the suspension and remove any small-scale turbulence, an aluminum cylinder was used with stainless steel wire mesh (1/16" mesh size). The cylinder had a provision in the base for an aluminum insert attached to the top of a long glass tube (170 cm.).

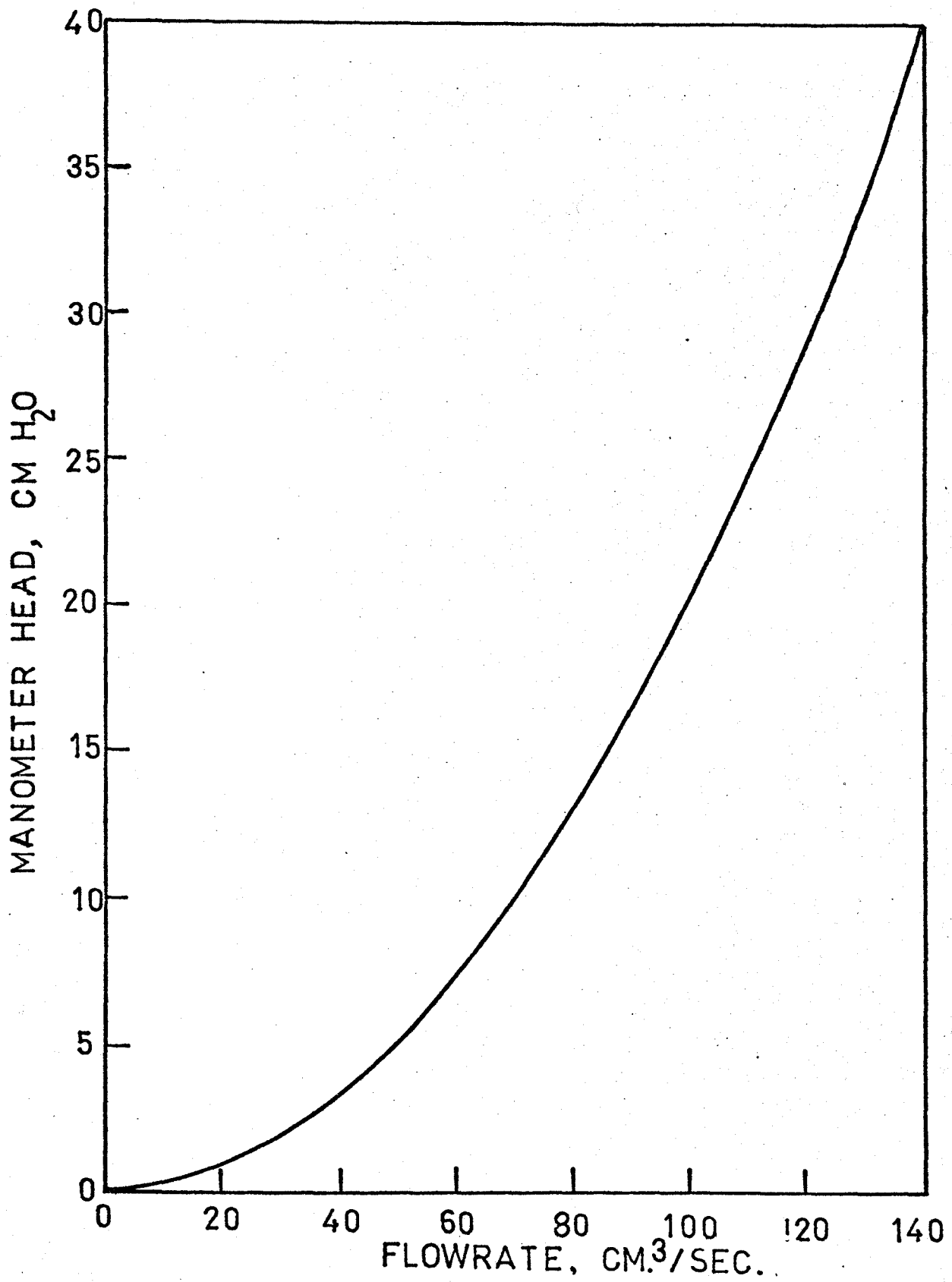


Figure 4. Flowmeter Calibration Curve.

The glass tube served as an extension for the model parent tube with the same inner diameter (1.867 cm). The length of that tube was sufficient to allow the development of a Poiseuille velocity distribution just upstream of the model.

A thermometer with  $0.2^{\circ}\text{C}$  divisions was provided at the top of the chamber to measure the circulating fluid temperature.

(d) Viewing Cell

The model to be studied was enclosed in a rectangular perspex cell, 77.5 cm x 22.8 cm. x 7.3 cm., secured to the top of a steel table (Plate 3). To facilitate changing of the model, the front side of the cell was removable, with sealing provided by .16 cm. diameter rubber cord set in a groove machined around the perimeter of the cell. The model inside the cell was mounted vertically and was attached to the upstream tube and downstream tubes by means of nylon Swagelok fittings. The two downstream tubes were 1.9 cm. in diameter and 60 cm. long each. They discharged the circulating fluid into a large tank. The purpose of this arrangement was to make sure that the pressure drop downstream and flows in each daughter tube were identical.

Within the cell, two front surface reflecting mirrors were positioned to provide a means of obtaining two mutually perpendicular views for both the parent and daughter tubes. The mirror adjacent to the parent tube (7.5 cm x 2.1 cm.) was set in a brass mount with its surface inclined at an angle

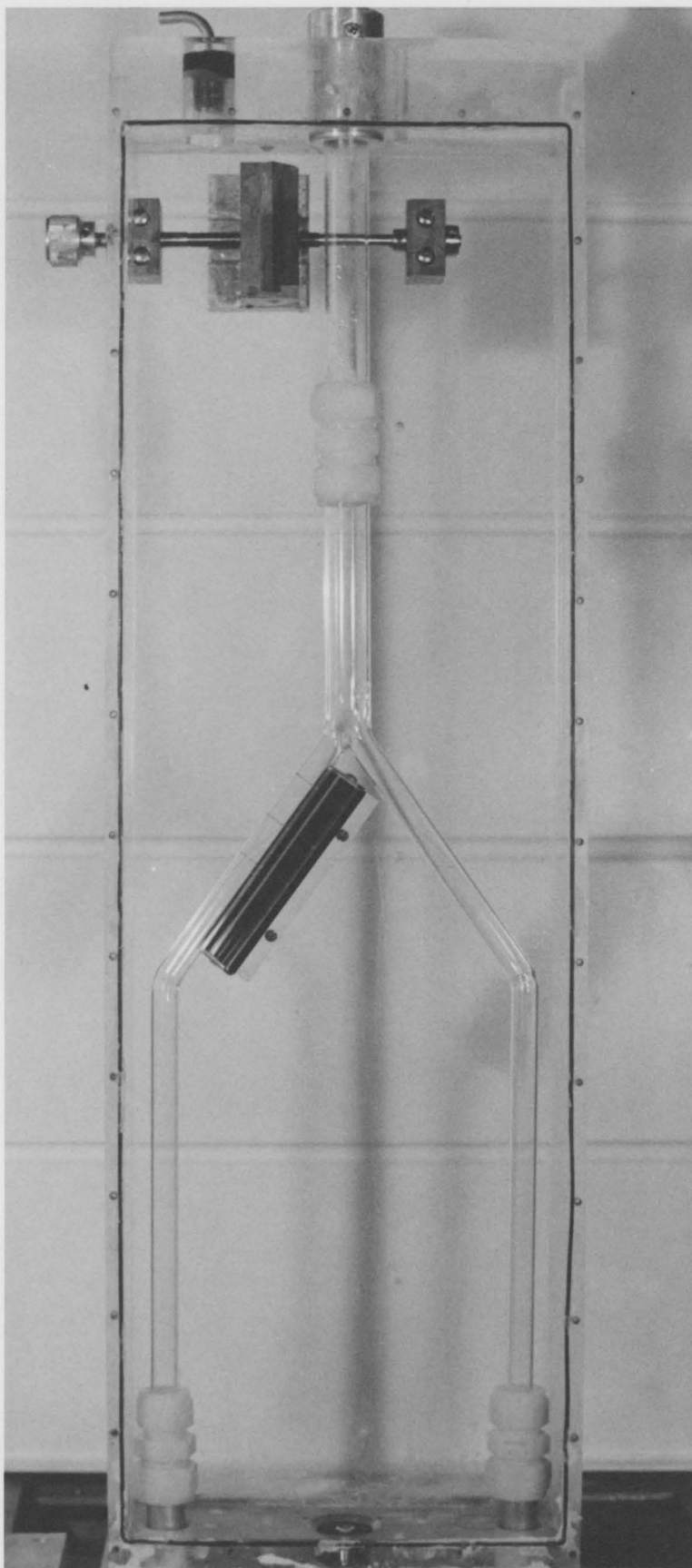


Plate 3. Viewing Cell

of  $45^\circ$  to the base of the mount. Its purpose was to allow a section of the parent tube to be filmed to determine whether the upstream velocity profile was parabolic and also to check the flowrate. (Appendix 1 ). The second mirror (2.4 cm. x 11.5 cm.) was mounted on a perspex mount with its surface inclined at  $45^\circ$  angle to the base of the mount. The mount was positioned parallel to the axis of the left daughter tube of the model (Plate 4).

The cell was filled from the bottom with an aqueous glycerol solution having a refractive index ( $n = 1.469$ ) very close to that of glass and of the circulating fluid.

(e) Pulsation Damper

In order to remove small pressure fluctuations produced by the pump, a damping chamber was used. It consisted of an inverted glass bottle put in series with the pump with an outlet to bleed air to the atmosphere. The air cushion on the top of the liquid in the bottle worked as a damper for the pressure fluctuations.

3.1.3. Photographic Equipment

(a) High-Speed Camera

A rotating prism cine camera (Hycam model number K 2001 R) with a maximum exposure rate of 3,000 full frames per second was used to obtain the photographic data. A 55 mm Asahi Pentax lens was used, together with a small extension tube, to provide an image of area approximately 3 cm. x 4 cm..

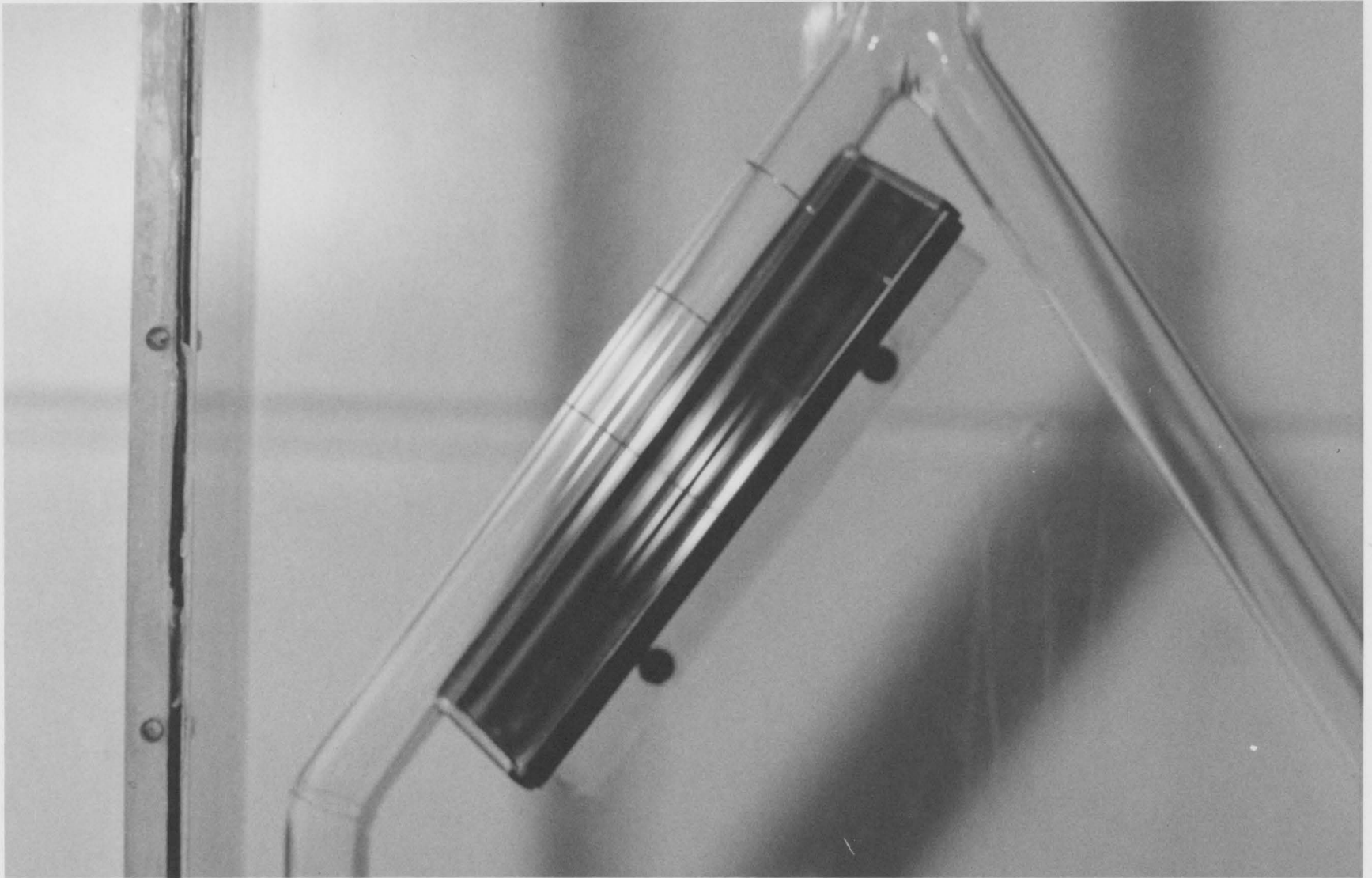


Plate 4. Front Surface Refracting Mirror Positioned  
Parallel to the Daughter Tube Axis

The film used was 16 mm, Eastman Kodak Double-X Negative (7222) on 100 foot reels.

The camera was mounted on a three-point tripod. The tripod allowed for vertical and angular positioning.

(b) Speed Control Unit

It was possible to vary and control the frame rate from 10 to 3,000 full frames per second by using a speed control unit. The frame rate was adjusted to a predetermined setting according to the flowrate in the filmed section.

(c) Pulse Generator

True film speed was obtained by using a Milli-Mile TL9-4 timing light generator which powered a small neon bulb in the camera. The bulb puts blips of light on the side of the film; the time between each is known from the frequency of the pulse generator, which was set at 100 pulses per second throughout all runs. The pulse generator has been calibrated with an oscilloscope and was found to give 100 pulses per second.

Since the camera accelerated to the desired speed relatively slowly, Figure 5 was provided to give the acceleration characteristics throughout the regulated range.

(d) Illumination

The section under investigation was illuminated by two beams of light 5 cm. in diameter, one from the side and

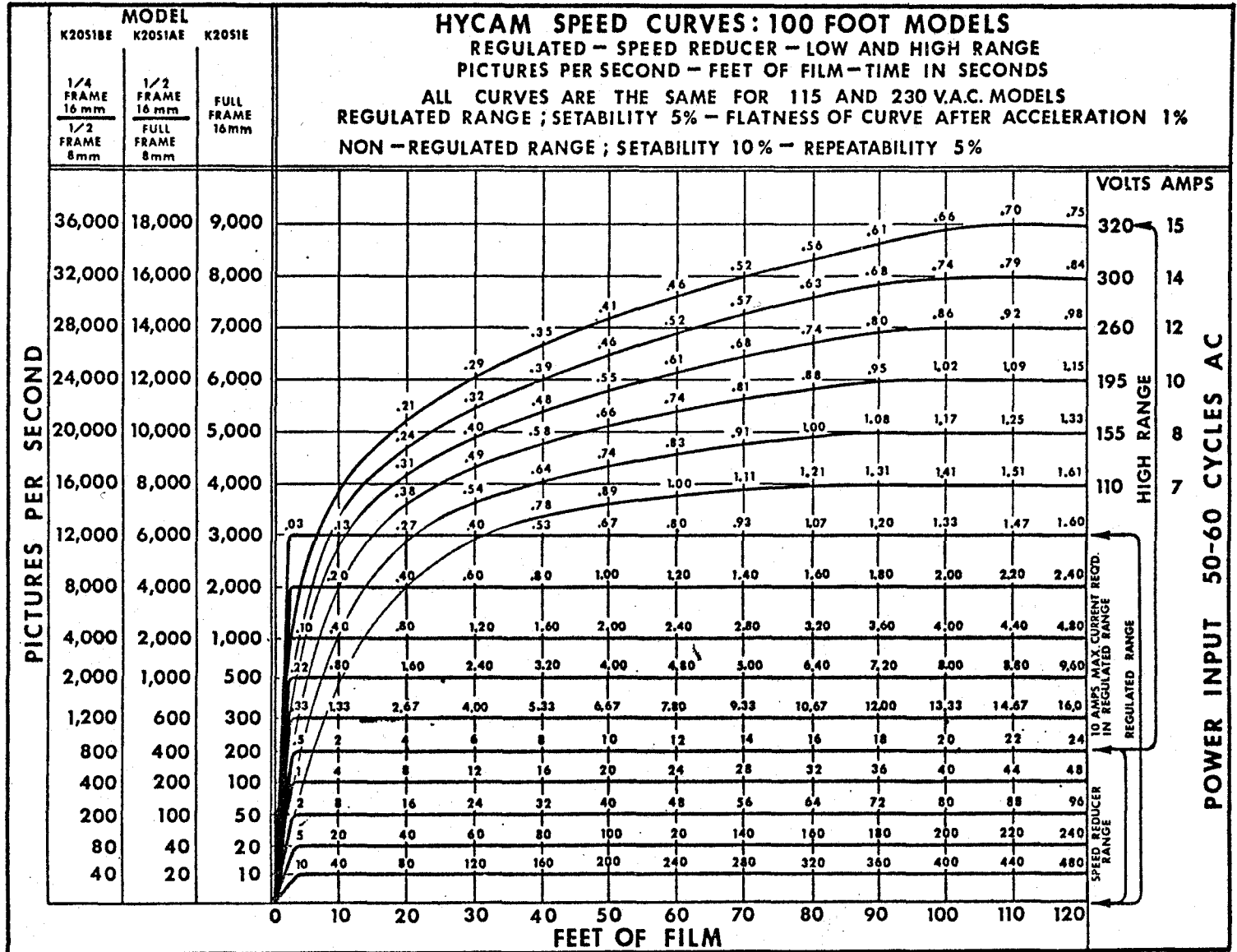


Figure 5. Hycam Speed Curve

the other from the rear, intersecting at right angles. Each beam was produced from a strong point source of light provided by a 100 watt carbon arc lamp and was placed at the focal point of a 16 cm. focal length Plano-convex lens. The lamp and the lens were mounted on an aluminum holder which was fastened to a 2 cm. diameter aluminum rod which could slide vertically in a sleeve attached to the steel table. To facilitate changing the beam angle, the light holder was attached to the rod by a pivot pin.

(e) Photo-optical Data Analyser

A photo-optical data analyser (Model 224-A) was used to analyze the films. It was positioned in a specially constructed rig to allow back projection onto a transparent screen. The frame rate was controlled by a remote hand-held unit.

3.2. Experimental Procedure

For each of the three models, a number of films were exposed. Each film represented an experimental run for one flow Reynolds number at one downstream position. For the sake of continuity, all downstream photography was done on the left limb.

To conduct a run, the arc lamp and plano-convex lens were carefully aligned to produce two mutually perpendicular beams of light intersecting the marked section to be filmed at right angles. The camera was set to view the

tube section and its image in the mirror set at a  $45^\circ$  angle parallel to the tube. Adjustment of the camera position was made using the tripod hand-wheels to move it vertically and incline it to the required angular position. The camera was always positioned such that the front face of the camera was parallel to the front face of the viewing cell.

Through the camera eyepiece, the tube walls appeared parallel to the edge of the film frame and the marking, which locates the distance  $z$  from the carina, appeared in the centre of the field of view on both the tube and its image. Then the object was brought into focus in the normal way.

The frame rate was set to a value at least  $20 V_m/d$ ,  $V_m$  being the mean axial velocity in the daughter tube and  $d$  its diameter. The fastest particle (assuming it to move with an axial velocity equal to  $2 V_m$ ) would then be recorded on at least 10 frames as it moved a distance equal to  $d$  cm. across the field of view. The timing light generator was set to give 100 pulses per second.

The flowrate was adjusted to a predetermined value and the fluid suspension circulated for at least 10 minutes to allow it to become homogeneous. The fluid suspension temperature was then recorded. A 100 foot roll of film was then threaded into the camera and the film was exposed by switching on the camera remote control. The film was subsequently taken out of the camera and returned to a sealed film tin. Finally, the fluid suspension temperature was recorded once more.

In some films, it was observed that some particles were blurred. This may be due to a smaller depth of field than was needed. The depth of the field has been estimated as approximately  $2 \frac{1}{2} d$  ( $d$  being the tube diameter). The camera optical system provided for a depth of field of about 3 cm. when the camera was positioned to view an area of about 4 cm. x 3 cm.

Blurring was only a problem when the largest diameter tube was filmed ( $d = 1.501$  cm.). Some particles, particularly those near the tube wall were fuzzy. To correct this situation three things were done, the camera was moved back and the lens was focused on a line approximately half way through the field of view, the side-light intensity was increased and the lens  $f$  stop was increased.

Table 3 gives a summary of the experimental runs and the identification for each one.

### 3.3. Film Analysis

Two views of the moving particles were recorded adjacent to each other on a number of frames to give the three dimensional flow pattern at the filmed section of the tube. In order to obtain quantitative data from the cine films, each film was projected and analyzed frame by frame using the photo-optical data analyser and back-projection screen. On the screen, the tube walls appeared clearly in each view. The centrelines were constructed for the tube and its image in the mirror. The tube diameter was measured carefully from

Experimental Identification	Model	Area Ratio ( $\alpha$ )	Flow Rate*	Daughter tube Diameter (cm.)	Distance Downstream Z/d
I-L-1	I	.75	L	1.142	2
I-L-2	I	.75	L	1.142	4
I-L-3	I	.75	L	1.142	6
I-M-1	I	.75	M	1.142	2
I-M-2	I	.75	M	1.142	4
I-M-3	I	.75	M	1.142	6
I-H-1	I	.75	H	1.142	2
I-H-2	I	.75	H	1.142	4
I-H-3	I	.75	H	1.142	6
II-M-1	II	1.02	M	1.339	2
II-M-2	II	1.02	M	1.339	4
II-M-3	II	1.02	M	1.339	6
III-M-1	III	1.29	M	1.501	2
III-M-2	III	1.29	M	1.501	4
III-M-3	III	1.29	M	1.501	6

- \* The letter L refers to Low flowrate ( $Re_N = 400$ )  
The letter M refers to Medium flowrate ( $Re_N = 800$ )  
The letter H refers to High flowrate ( $Re_N = 1200$ )

Table 3. Experimental Identification

both views. These values were used to calculate the magnification factor. The horizontal line (marked on tube) appeared in the view defining the  $z$  coordinate. By allowing the particle to move through a vertical distance of about 1/2 to 1 cm. either, side of the horizontal line, it was possible to measure three sets of particle coordinates  $(x_1, y_1, z_1)$  and  $(x_2, y_2, z_2)$  at planes 1 and 2 up and down from the horizontal line respectively and also the particle coordinates  $(x, y, z)$  at the horizontal line plane. (See Figure 6). The corresponding time increment,  $\Delta T$ , for the particle movement between 1 and 2 was obtained from the camera frame rate. The following quantities could then be computed.

The axial displacement  $\Delta z = z_2 - z_1$

The tangential displacement  $\Delta s = r (\theta_2 - \theta_1)$

where  $r = \sqrt{x^2 + y^2}$ ,  $\theta_1 = \tan^{-1} \frac{y_1}{x_1}$  and  $\theta_2 = \tan^{-1} \frac{y_2}{x_2}$

The radial displacement  $\Delta r = r_2 - r_1$

where  $r_1 = \sqrt{x_1^2 + y_1^2}$  and  $r_2 = \sqrt{x_2^2 + y_2^2}$

The three velocity components were calculated as

Axial velocity component  $V_z = \frac{\Delta z}{\Delta T}$

Tangential velocity component  $V_\theta = \frac{\Delta s}{\Delta T}$

Radial velocity component  $V_r = \frac{\Delta r}{\Delta T}$

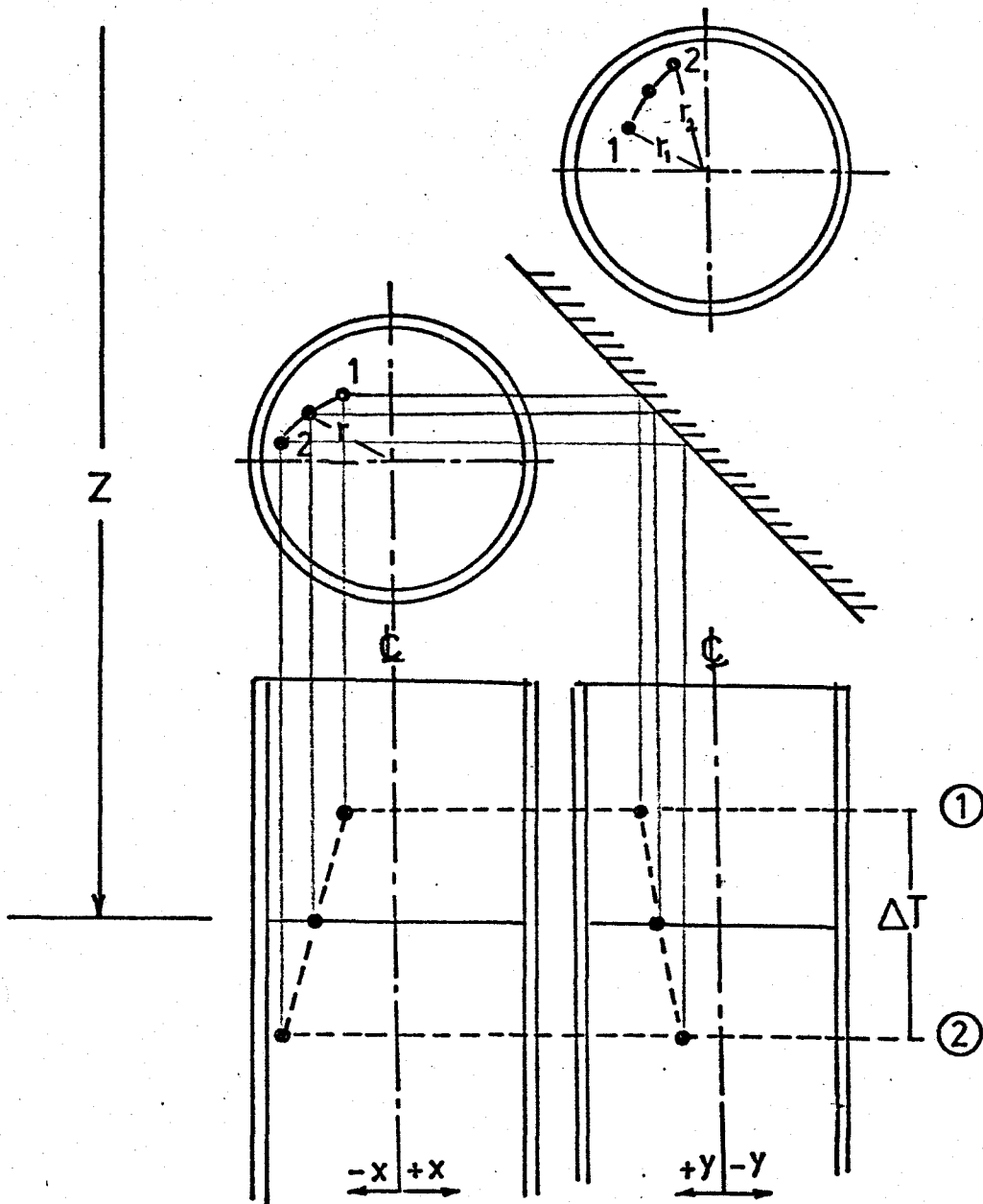


Figure 6 Film Analysis

## CHAPTER 4

### RESULTS

The most difficult factor in studying the flow in branches is the extremely complicated nature of the flow which makes complete theoretical analysis of the problem almost impossible, at least by present-day methods. Solution of the Navier-Stokes equations for two-dimensional flow has been achieved only under certain stringent conditions [Lew (10, 12), Lynn (13) and Zamir (14)]. Whereas the flow through a branch is a three-dimensional flow through curved pipes with varying cross-sectional area. There can therefore be no direct comparison between theoretical treatises and experimental results.

The experimental investigation carried out in this work provides a detailed study of the velocity field and wall shear rate distribution in symmetrical branches, typical of the blood vessels in man.

Table 4 summarizes the experimental runs and the operating parameters for each run.

#### 4.1. Velocity Profiles

For each experimental run a number of particles (45-75) were analyzed as outlined in Section 3.3. These particles were chosen to be well distributed all over the tube cross section. The three velocity components were calculated for each particle and these components were used

Experiment	$\alpha$	d/D	Z(cm)	T(Degree C)	$\mu$ (Centi Poise)	$Q_d$ (cm <sup>3</sup> /sec)	$V_m$ (cm/sec)	$(Re_N)_d$	$Re_N$
I-L-1	.75	.80	2.28	16.5	8.0	22.2	21.7	322	394
I-L-2	.75	.80	4.57	17.0	7.8	22.2	21.7	330	404
I-L-3	.75	.80	6.85	17.0	7.8	22.2	21.7	330	404
I-M-1	.75	.80	2.28	18.0	7.3	42.5	41.3	674	825
I-M-2	.75	.80	4.57	17.5	7.5	42.5	41.3	656	803
I-M-3	.75	.80	6.85	17.5	7.5	42.5	41.3	656	803
I-H-1	.75	.80	2.28	18.3	7.2	61.0	59.4	983	1202
I-H-2	.75	.80	4.57	18.3	7.2	61.0	59.4	983	1202
I-H-3	.75	.80	6.85	18.4	7.1	61.0	59.4	996	1219
II-M-1	1.02	.71	2.68	17.2	7.65	42.5	30.4	548	786
II-M-2	1.02	.71	5.36	17.2	7.65	42.5	30.4	548	786
II-M-3	1.02	.71	8.04	17.4	7.55	42.5	30.4	555	797
III-M-1	1.29	.61	3.00	17.3	7.6	42.5	24.0	493	792
III-M-2	1.29	.61	6.00	17.4	7.55	42.5	24.0	496	797
III-M-3	1.29	.61	9.01	17.5	7.5	42.5	24.0	499	803

Table 4. Experimental Operating Parameters.

to describe the flow pattern at that cross section. The particle location was defined by the non-dimensional radial coordinate ( $\eta$ ) and the angular coordinate ( $\theta$ ). Each particle had three non-dimensional velocity components:

1. Non-dimensional axial velocity component  $V_z^+ = \frac{V_z}{V_m}$
2. Non-dimensional tangential velocity component  $V_\theta^+ = \frac{V_\theta}{V_m}$
3. Non-dimensional radial velocity component  $V_r^+ = \frac{V_r}{V_m}$

where  $\eta = \frac{r}{R}$ ,  $R$  is the daughter tube diameter

$V_m$  is the mean velocity calculated from the flowrate in the daughter tube, assuming the branch divides the flow equally between the two limbs. The flowrate in the parent tube was checked by obtaining the velocity profiles upstream of the branch photographically. Values obtained upon integrating the velocity profiles were consistent with those obtained from the flowmeter (Appendix 1).

In order to characterize the tangential and radial velocity components, a mean value and standard deviation were computed for all values at each location. The mean values for both  $V_\theta^+$  and  $V_r^+$  were found to be zero to 2 decimal places. Standard deviations were in the range (.01-.06) for both tangential and radial velocity components (see Table 5).

In general, both the tangential and radial velocity values were approximately within 6% of the corresponding mean axial velocity in any location studied in this work. In the

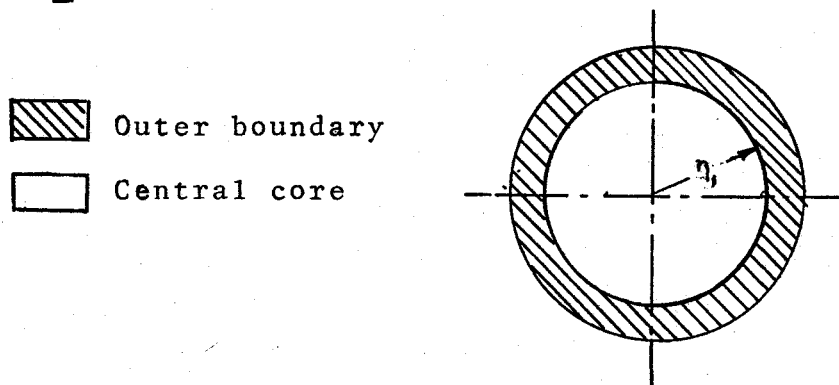
Experiment #	$V_{\theta}^+$		$V_r^+$	
	Mean Value	Standard Deviation	Mean Value	Standard Deviation
I-L-1	0.00	0.02	0.00	0.02
I-L-2	0.00	0.02	0.00	0.02
I-L-3	0.00	0.01	0.00	0.01
I-M-1	0.00	0.06	0.00	0.06
I-M-2	0.00	0.06	0.00	0.05
I-M-3	0.00	0.06	0.00	0.05
I-H-1	0.00	0.03	0.00	0.04
I-H-2	0.00	0.03	0.00	0.04
I-H-3	0.00	0.02	0.00	0.03
II-M-1	0.00	0.02	0.00	0.01
II-M-2	0.00	0.01	0.00	0.02
II-M-3	0.00	0.01	0.00	0.01
III-M-1	0.00	0.04	0.00	0.01
III-M-2	0.00	0.02	0.00	0.02
III-M-3	0.00	0.01	0.00	0.01

Table 5. Mean Value and Standard Deviation for the Non-dimensional Tangential and Radial Velocity Components.

light of this analysis, it was considered that the axial velocity component was the most important component to describe the flow and its development downstream.

In order to represent the axial velocity profile at any location, it was necessary to fit the local velocity values, over the tube cross-section to a mathematical function. This mathematical function should satisfy the velocity boundary conditions and be a function of  $\eta$  and  $\theta$ .

Due to the complex nature of the flow, it was decided to divide the velocity field into two sections. The outer boundary section extended from  $\eta_1$  approximately equal to .7 to the tube wall  $\eta$  equal to 1.0 and around the tube ( $0.0 \leq \theta < 2\pi$ ). The Central Core section extended over



the remainder of the cross-section ( $0 \leq \eta \leq \eta_1$ ), ( $0 \leq \theta \leq 2\pi$ ).

The value of  $\eta_1$ , which was the radius of the circle dividing the cross-section into two sections, was selected as the expected position for a peak velocity. This value was located by examining the tendency of the local velocity to increase or decrease with increasing  $\eta$ .

The axial velocity profile in the outer boundary section was approximated by a function of the form

$$V_z^+ (\eta, \theta) = V_z^+ (\eta) * V_z^+ (\theta) \quad (4.1)$$

where 
$$V_z^+ = \sum_{i=1}^n A_i (1-\eta^i) \quad (n^{\text{th}} \text{ degree polynomial in } \eta)$$

and 
$$V_z^+ (\theta) = 1 + A_{n+1} \cos\theta + A_{n+2} \sin\theta \quad (\text{periodic function of } \theta)$$

or 
$$V_z^+ (\eta, \theta) = \left[ \sum_{i=1}^n A_i (1-\eta^i) \right] * [1 + A_{n+1} \cos\theta + A_{n+2} \sin\theta] \quad (4.2)$$

where  $A_i$ 's,  $A_{n+1}$  and  $A_{n+2}$  are independent parameters to be obtained via non-linear regression. A non-linear least squares curve fitting program using Marquardt's Maximum Neighborhood Method was used to determine the parameter values.

In all the fifteen outer boundary profiles, the first three parameters in the  $n^{\text{th}}$  degree polynomial in  $\eta$  were found to be sufficient to give fairly good fitting results. The highest Residual Root Mean Square was .134 (for data obtained from experiment I-L-2). The R.R.M.S value represents the absolute residual value below which approximately 68% of the data will fall. Table 6 gives the fitting results with values of R.R.M.S. These values (.043-.134) are small when compared to the non-dimensional mean velocity (1.0) which

Experiment	$\eta_1$	Coefficient of Equation (4.3)				R.R.M.S. <sup>+</sup>
		A <sub>1</sub>	A <sub>2</sub>	A <sub>3</sub>	A <sub>4</sub>	
I-L-1	.65	0.0000	-2.2173	3.9196	.513	.118
I-L-2	.6	0.0000	-7.4787	7.8636	.2629	.134
I-L-3	.6	31.4765	-37.7253	16.7304	.1805	.098
I-M-1	.8	162.0341	-202.9782	85.9486	.6221	.010
I-M-2	.75	119.2314	-142.1914	58.5659	.3326	0.071
I-M-3	.75	53.2293	-63.4091	27.3563	.2566	0.065
I-H-1	.8	75.5912	-116.4073	58.2724	.4381	0.128
I-H-2	.75	61.4781	-99.4956	51.5672	.3123	0.100
I-H-3	.7	12.2657	-42.6159	29.8351	.2193	.130
II-M-1	.75	104.4935	-140.9127	63.8741	.6619	.123
II-M-2	.7	106.5696	-128.4994	53.5842	.3368	.043
II-M-3	.7	88.9551	-111.1033	47.9068	.2792	.085
III-M-1	.8	401.4453	-483.7832	194.4951	.7885	.091
III-M-2	.8	442.8327	-501.4716	190.8976	.5167	.116
III-M-3	.8	510.3361	-576.7050	218.6993	.2607	.085

+ Residual Root Mean Square

Table 6. Parameter Estimation of Velocity Profiles in the Outer Boundary Region.

is a good characteristic value to represent the flow.

The parameter  $A_{n+2}$  in Equation (4.1) was found to be very small compared to the parameter  $A_{n+1}$ . This means that the axial velocity profiles were symmetric with respect to plane A-A (see branch notation). This was expected from the geometric symmetry with respect to the plane of the bifurcation (Plate 2 shows this symmetry in one of the glass models used in this study). Therefore the general functional form given by Equation (4.2) reduces to

$$V_z^+ (\eta, \theta) = [A_1 (1-\eta) + A_2 (1-\eta^2) + A_3 (1-\eta^3)] * [1 + A_4 \cos\theta]$$

$$\eta_1 < \eta \leq 1.0$$
(4.3)

Table 6 gives values of parameters  $A_1$ ,  $A_2$ ,  $A_3$  and  $A_4$ .

The axial velocity profile in the central core section was approximated by a function of the form

$$V_z^+ (\eta, \theta) = \left[ \sum_{i=0}^n B_i \eta^i \right] * [1 + \eta (B_{n+1} \cos\theta + B_{n+2} \sin\theta)]$$
(4.4)

where  $B_i$ 's,  $B_{n+1}$  and  $B_{n+2}$  are independent parameters to be obtained from non-linear regression. The above non-linear fitting program was used to determine the parameter values. Values of the parameters with  $i$  greater than 3 were found to be very small compared to the first four parameters. The parameter  $B_{n+2}$  was also small compared to  $B_{n+1}$  confirming the symmetry of the profiles with respect to the plane of the bifurcation. This reduces Equation (4.4) to

$$V_z^+ (\eta, \theta) = [B_0 + B_1 \eta + B_2 \eta^2 + B_3 \eta^3] * [1 + B_4 \eta \cos \theta] \quad (4.5)$$

$$0.0 \leq \eta < \eta_1$$

The fitting results are given in Table 7 with R.R.M.S. values for each profile. The R.R.M.S. values were found to be within the range (.072-.142).

The two functions given by Equations (4.3) and (4.5) represent the axial velocity profile over the tube cross-section. These functions satisfy the following conditions:

1.  $V_z^+ = 0$  at  $\eta = 1.0$  (zero velocity at tube wall)
2.  $V_z^+ = B_0$  at  $\eta = 0.0$  (centreline velocity independent of  $\theta$ )

In order to represent the velocity profiles graphically, the two functional forms were evaluated at the bifurcation plane A-A ( $\theta = 0.0$  and  $\theta = \pi$ ) and at the plane normal to the bifurcation plane B-B ( $\theta = \frac{\pi}{2}$  and  $\theta = \frac{3\pi}{2}$ ), (see branch notation). The two functions did not match exactly at position  $\eta$ , since they were not constrained to do so. Although the matching error was kept to the minimum, the velocity profiles showed a

Experiment	$\eta_1$	Coefficients of Equation (4.5)					R.R.M.S. <sup>+</sup>
		$B_0$	$B_1$	$B_2$	$B_3$	$B_4$	
I-L-1	.65	1.1518	-0.0	0.9453	0.0066	0.4617	.089
I-L-2	.6	1.2619	-0.4047	1.1962	0.0	0.3013	.137
I-L-3	.6	1.37326	-.4500	1.3315	0.0	0.2678	.101
I-M-1	.8	.7563	-.4235	1.1251	0.0	.5041	0.110
I-M-2	.75	.9152	-.3326	1.0746	0.0	.3241	0.098
I-M-3	.7	1.0656	-.2858	1.3972	0.0	.1804	0.072
I-H-1	.8	.9152	-.5715	1.0578	0.0	.5102	0.097
I-H-2	.75	1.2676	-.4551	0.0013	2.5847	.1989	0.143
I-H-3	.7	1.4262	-.4903	0.0004	2.8189	.1865	.130
II-M-1	.75	0.7620	-0.3858	1.8314	0.0	.7366	.146
II-M-2	.7	0.9767	-0.7802	1.8205	0.0	.2301	.094
II-M-3	.7	1.1792	-0.7178	1.2693	0.0	.1713	.075
III-M-1	.8	0.5262	-0.4377	1.7941	0.0	0.8106	.114
III-M-2	.8	0.6464	-0.4292	1.7058	0.0	0.3882	.130
III-M-3	.8	0.9831	-0.4526	1.1588	0.0	0.0702	.146

+ Residual Root Mean Square

Table 7. Parameter Estimation of Velocity Profiles in the Central Core Region.

discontinuity at position  $n_1$ . In order to smooth the two-dimensional profiles, a Fortran program for smoothing a curve through discrete data (more detail may be found in (20)) was used. The smoothing process did not change the profile general shape and the change in the velocity values was very small (maximum change =  $\pm 2\%$ ). The resulting profiles are shown in Figures 7-21.

The flow mean velocity can also be calculated by integrating the velocity functions over the tube cross-section.

$$(V_m)_c = \frac{1}{\pi R^2} \int_0^R \int_0^{2\pi} V_z(r, \theta) r dr d\theta \quad (4.6)$$

or in dimensionless form

$$\frac{(V_m)_c}{V_m} = \frac{1}{\pi} \int_0^{\eta} \int_0^{2\pi} V_z^+(\eta, \theta) \eta d\eta d\theta \quad (4.7)$$

where  $V_m$  is the flow mean velocity in the daughter tube obtained from the flowrate by assuming the branch divides the flow equally between the two limbs.  $V_z^+$  is the non-dimensional axial velocity given by Equations (4.3) and (4.5).

The ratio  $\frac{(V_m)_c}{V_m}$  was on average 5% higher than unity. The discrepancy between  $(V_m)_c$  and  $V_m$  is explained by the fact that  $V_m$  was calculated by assuming half the flow rate in the parent tube goes to each daughter tube, however, it was very possible that small differences in the pressure

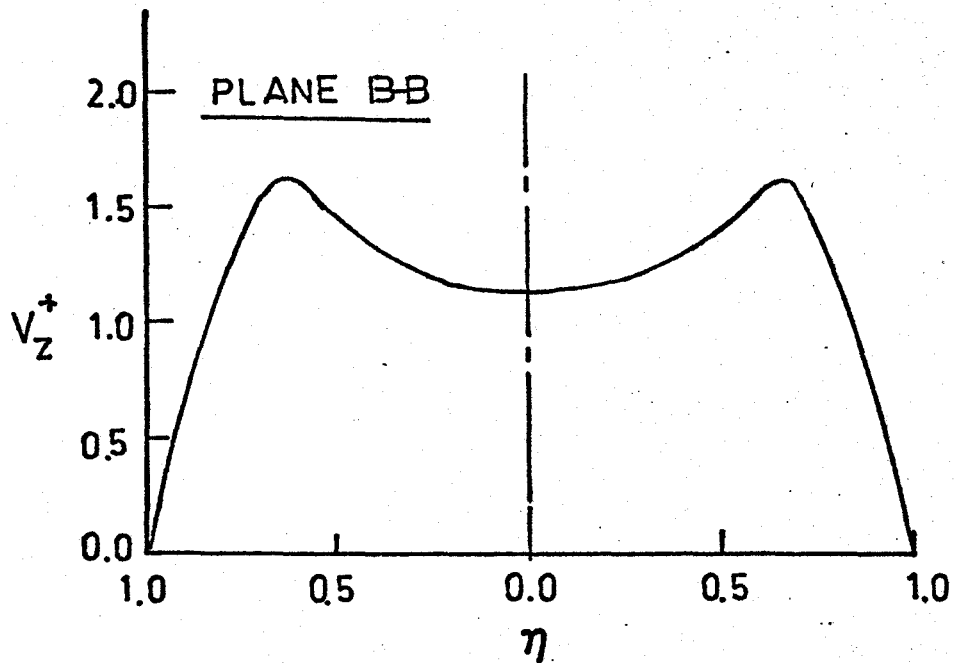
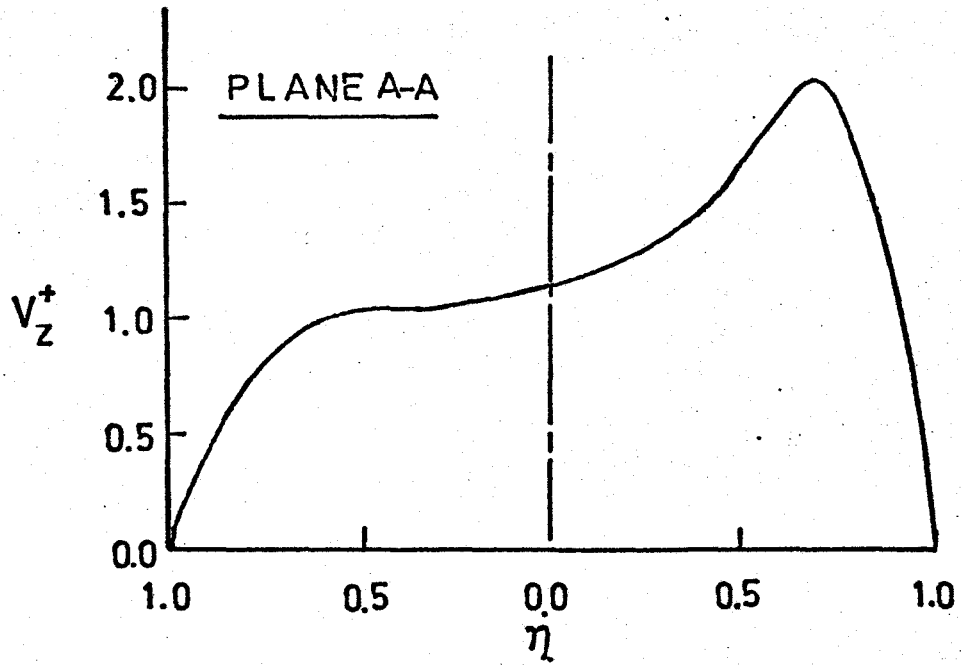


Figure 7. Non-dimensional Velocity Profiles  
for Experiment (I-L-1).  
( $\alpha = .75$ ,  $Re_N = 400$ ,  $Z/d = 2$ )

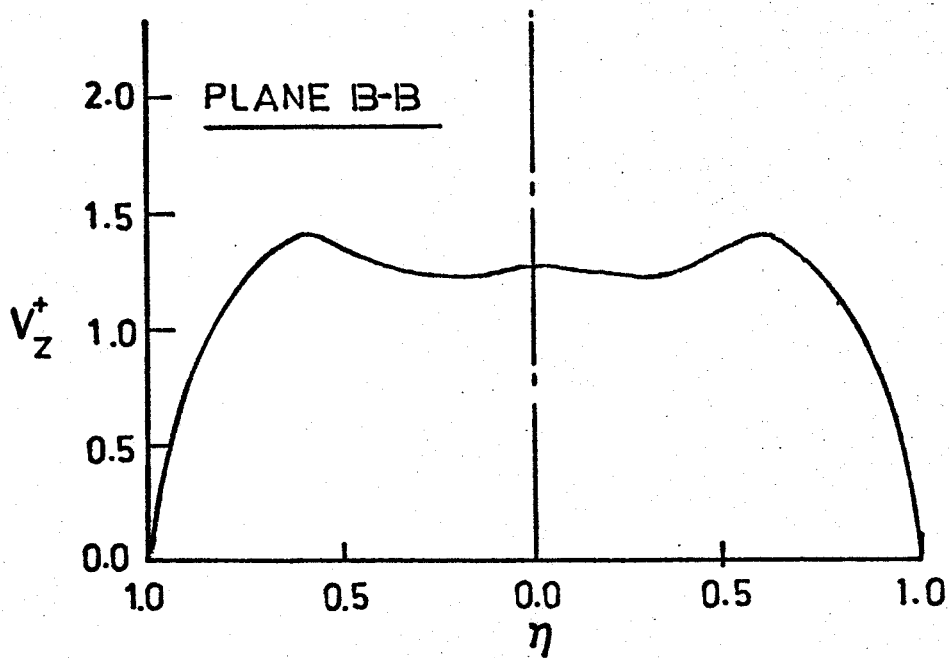
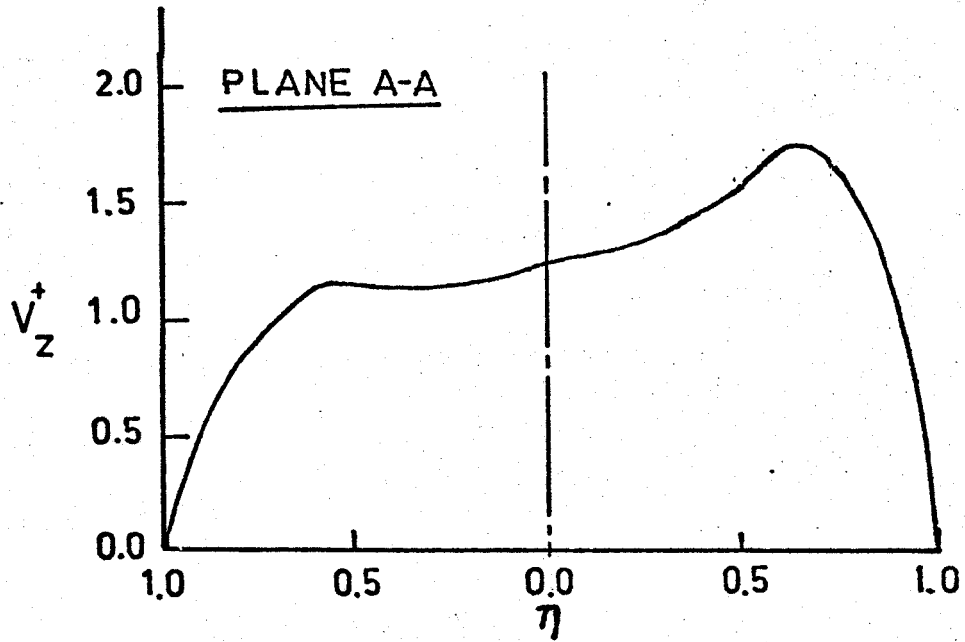


Figure 8. Non-dimensional Velocity Profiles for Experiment (I-L-2).  
( $\alpha = 0.75$ ,  $Re_N = 400$ ,  $Z/d = 4$ )

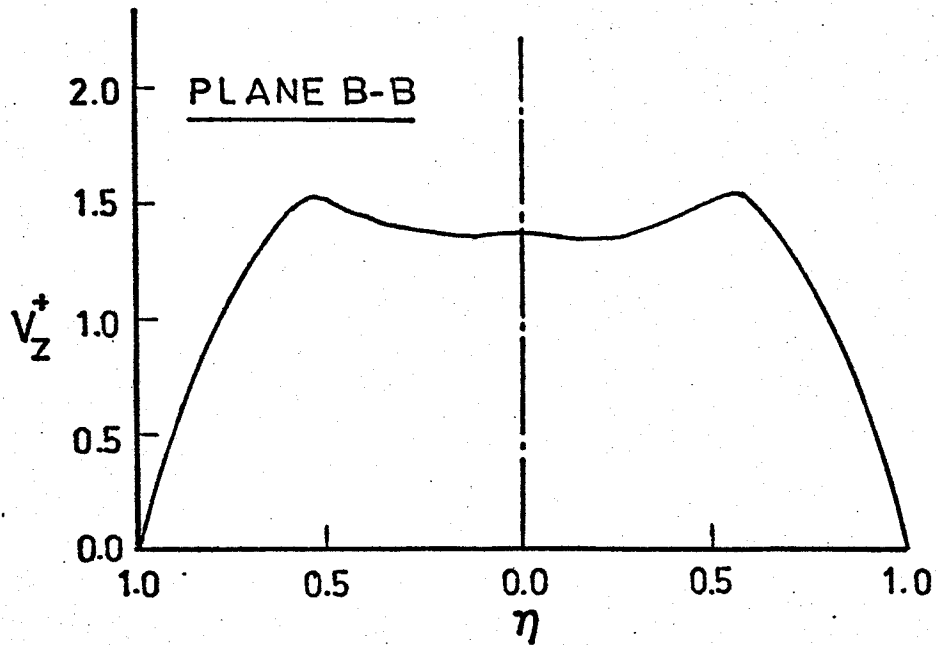
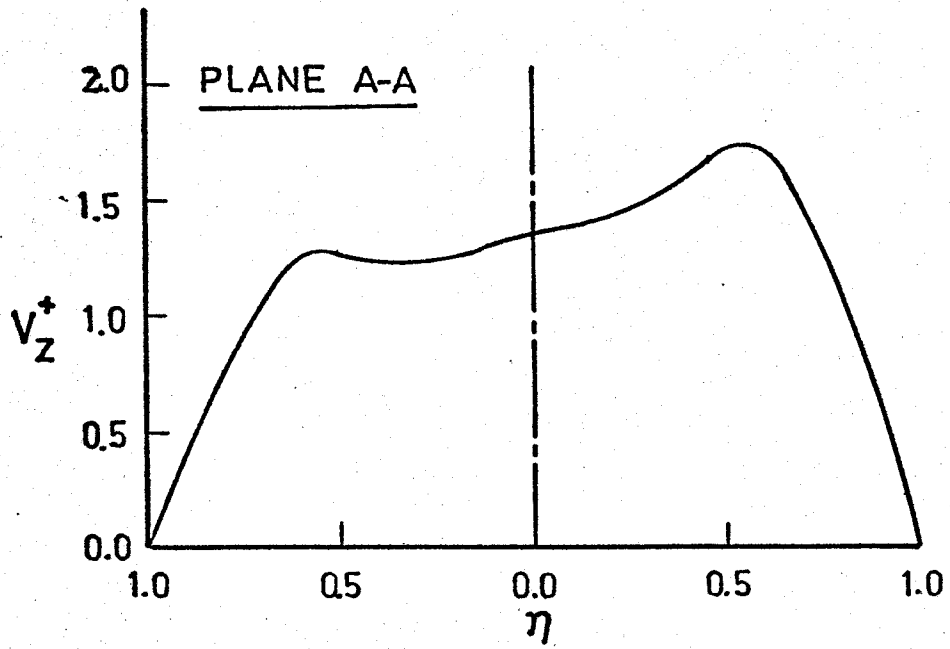


Figure 9. Non-dimensional Velocity Profiles for Experiment (I-L-3).  
( $\alpha = 0.75$ ,  $Re_N = 400$ ,  $Z/d = 6$ )

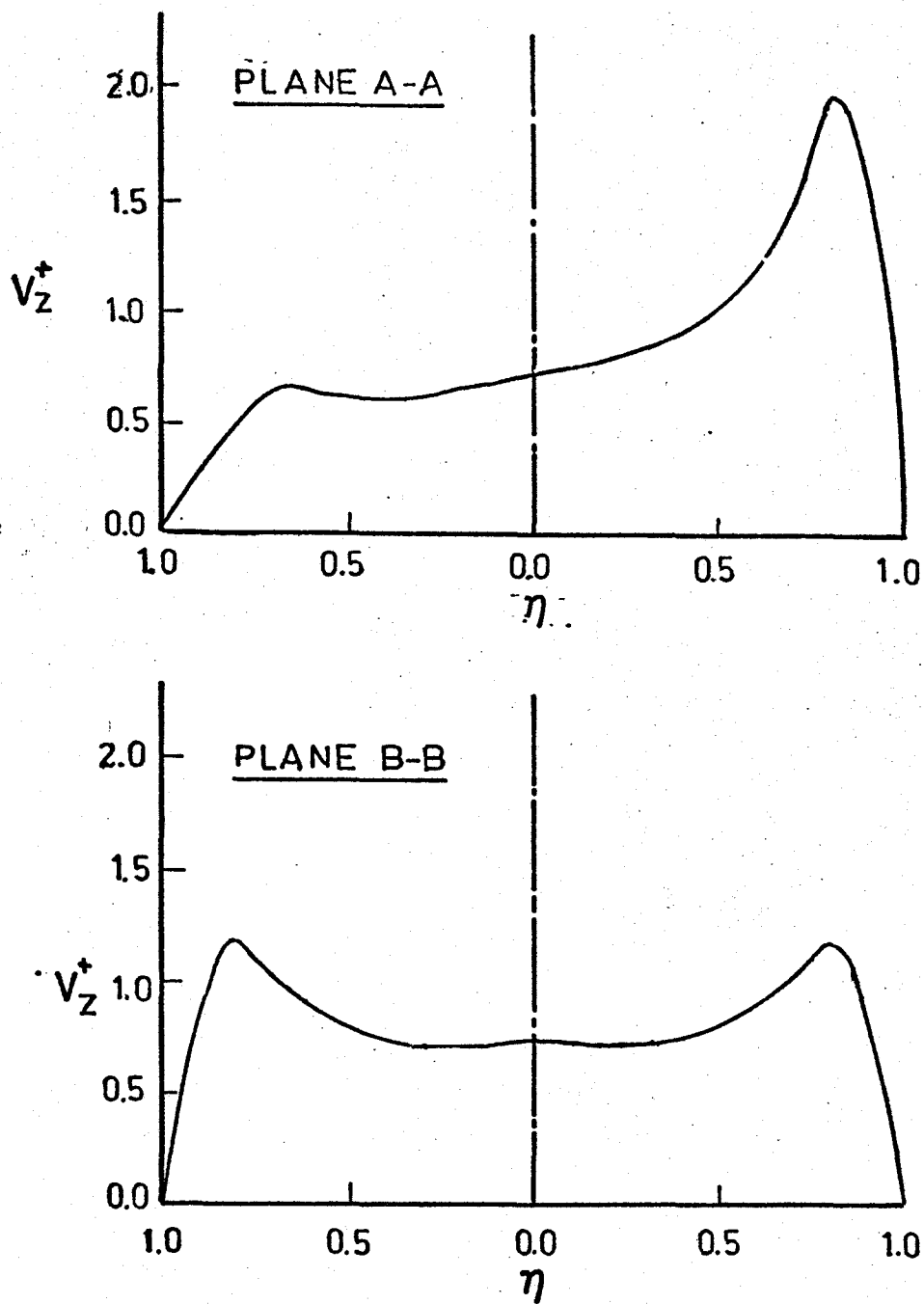


Figure 10. Non-dimensional Velocity Profiles for Experiment (I-M-1).  
 $(\alpha = 0.75, Re_N = 800, z/d = 2)$

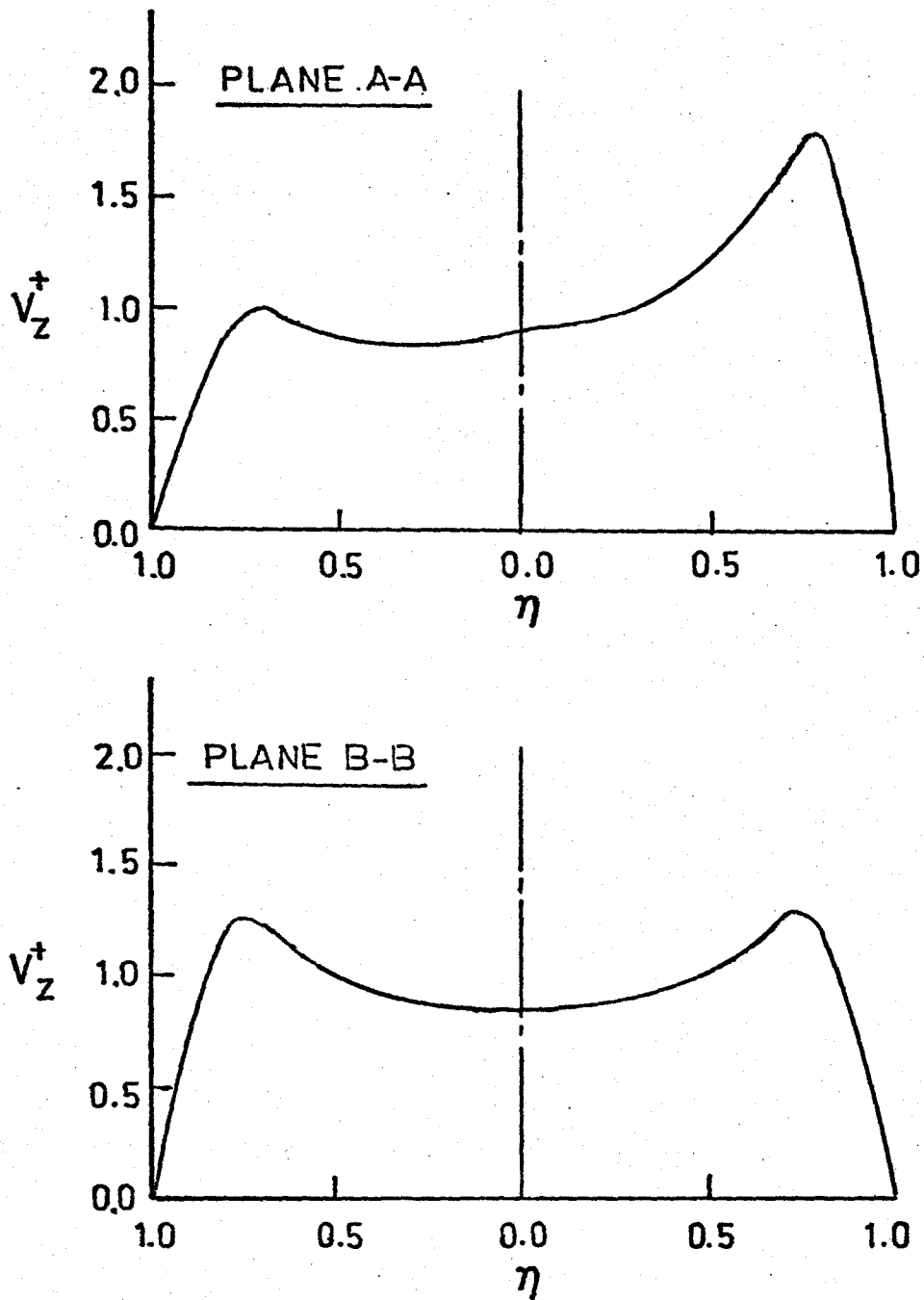


Figure 11. Non-dimensional Velocity Profiles  
for Experiment (I-M-2).  
( $\alpha = 0.75$ ,  $Re_N = 800$ ,  $Z/d = 4$ )

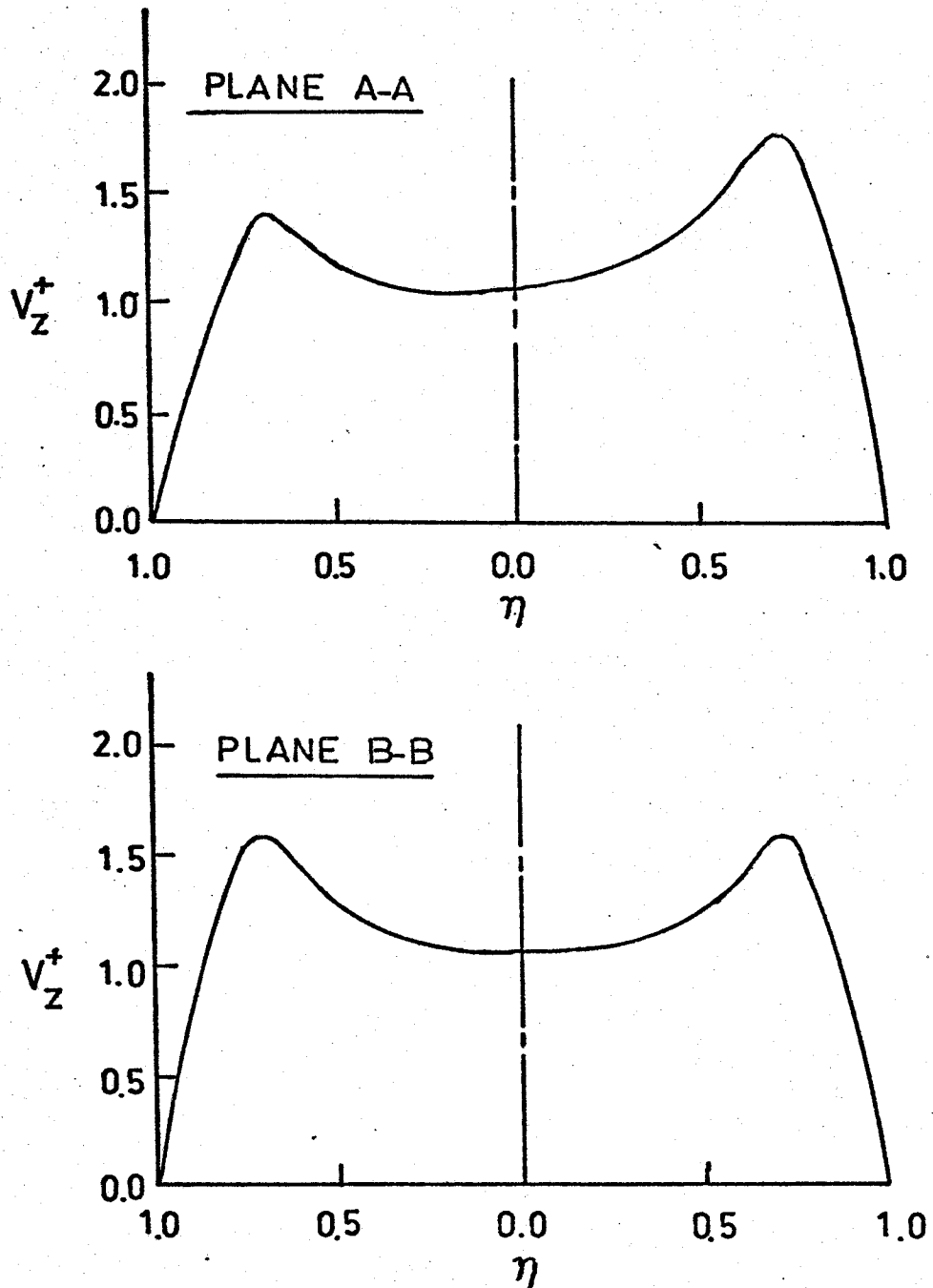


Figure 12. Non-dimensional Velocity Profiles for Experiment (I-M-3).  
( $\alpha = 0.75$ ,  $Re_N = 800$ ,  $Z/d = 6$ )

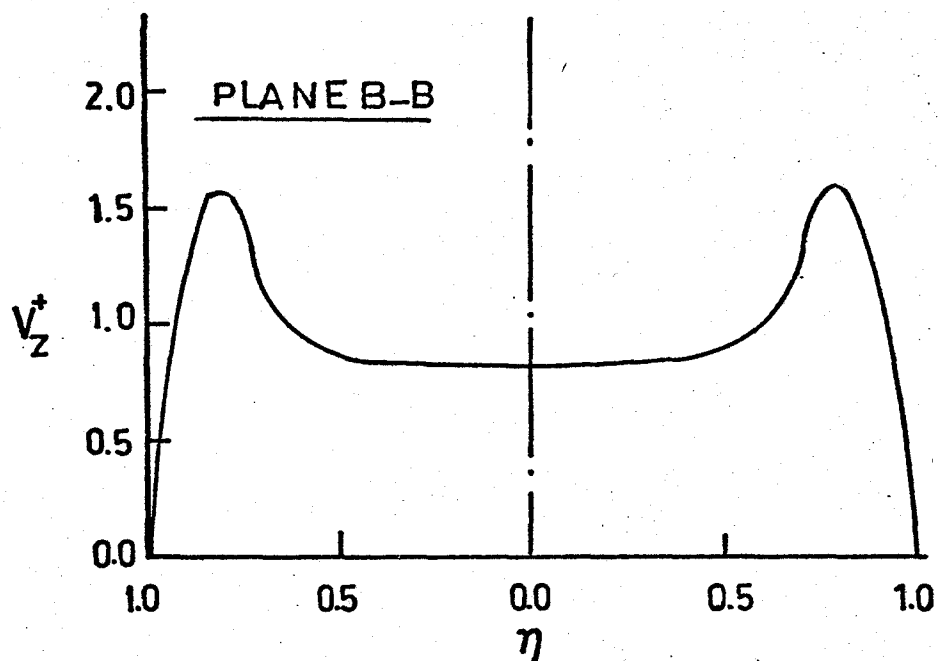
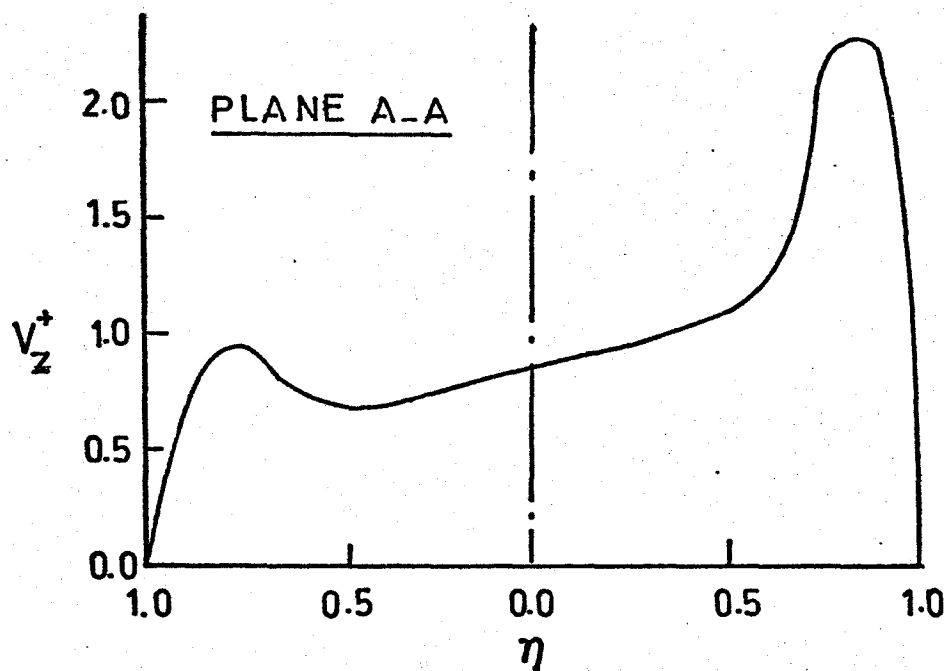


Figure 13. Non-dimensional Velocity Profiles for Experiment (I-H-1).  
( $\alpha = 0.75$ ,  $Re_N = 1200$ ,  $Z/d = 2$ )

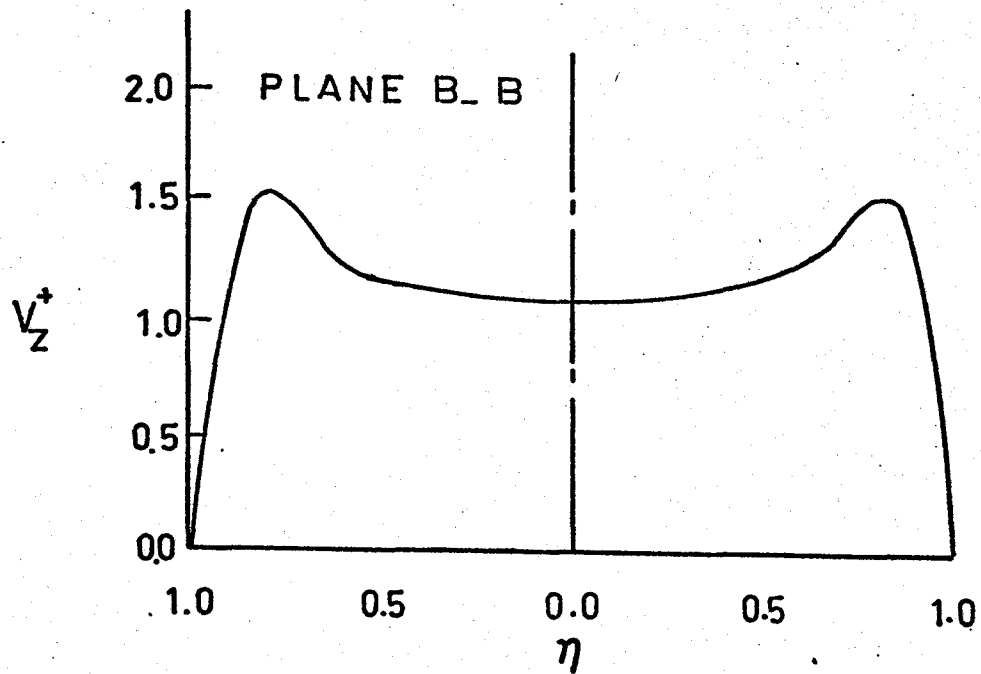
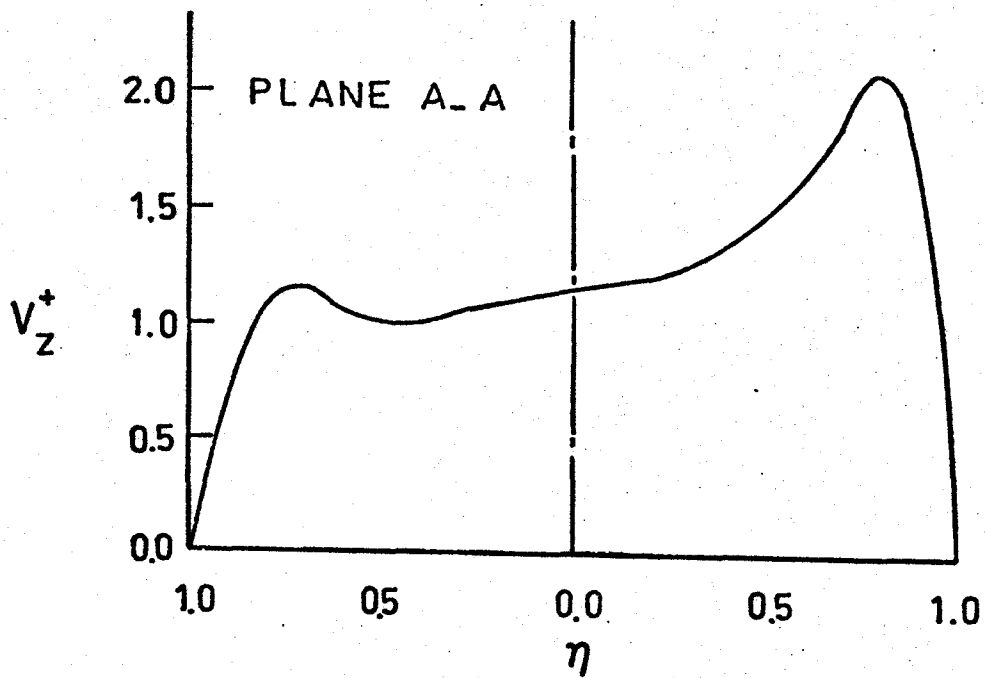


Figure 14. Non-dimensional Velocity Profiles for Experiment (I-H-2).  
( $\alpha = 0.75$ ,  $Re_N = 1200$ ,  $Z/d = 4$ )

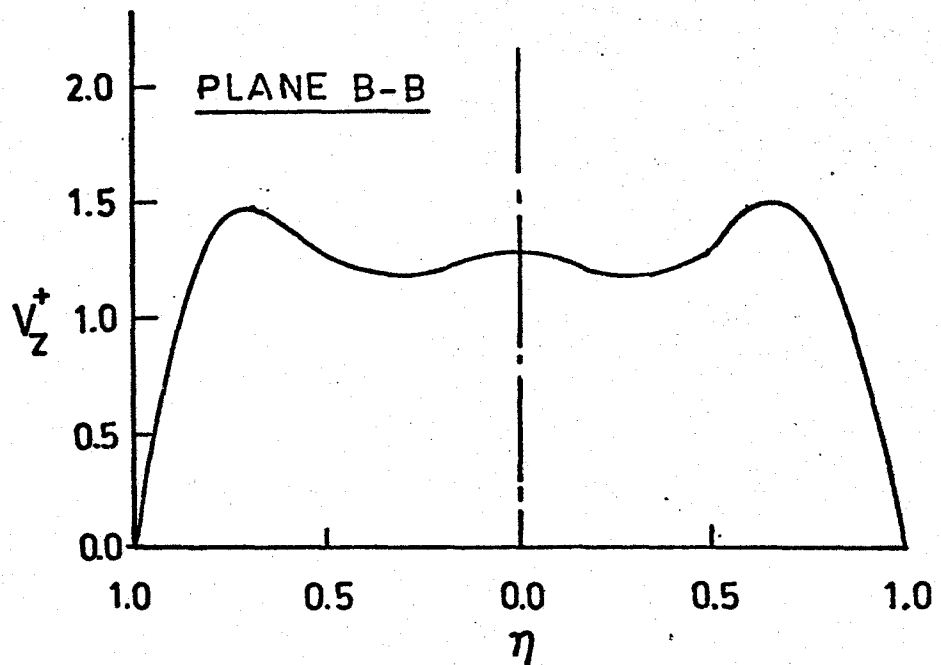
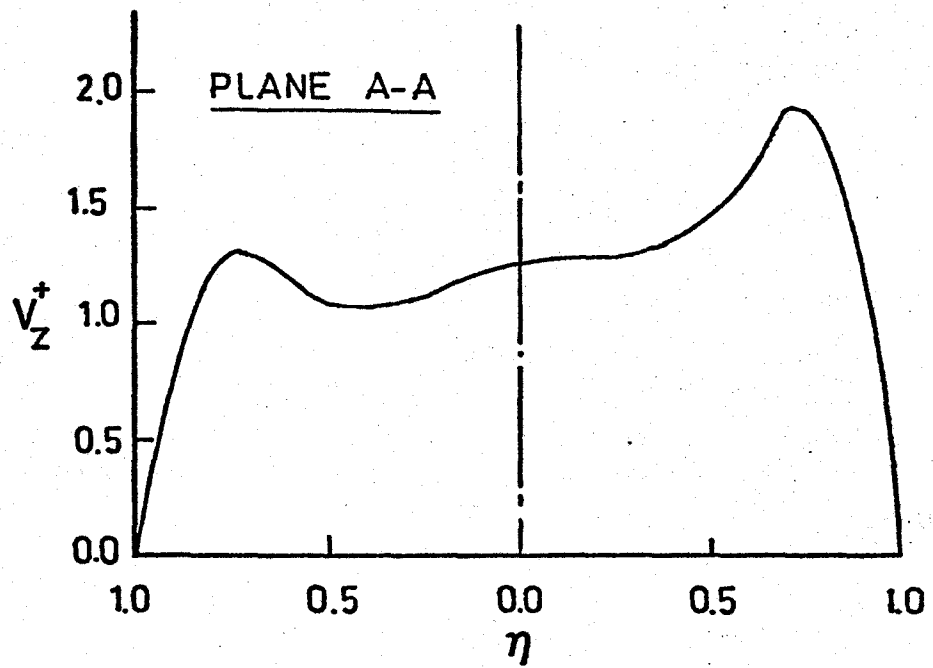


Figure 15. Non-dimensional Velocity Profiles for Experiment (I-H-3).  
( $\alpha = 0.75$ ,  $Re_N = 1200$ ,  $Z/d = 6$ )

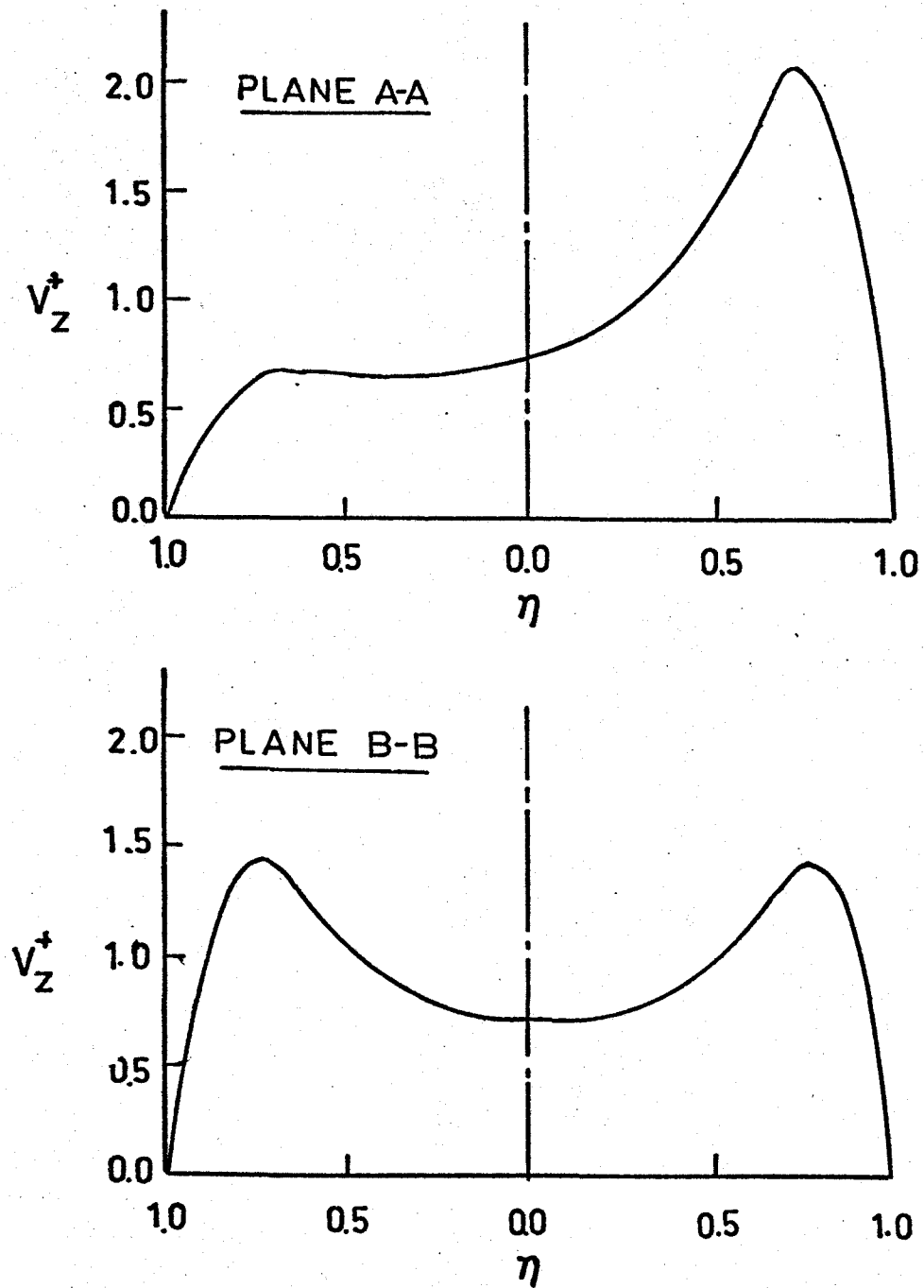


Figure 16. Non-dimensional Velocity Profiles  
for Experiment (II-M-1).  
( $\alpha = 1.02$ ,  $Re_N = 800$ ,  $Z/d = 2$ )

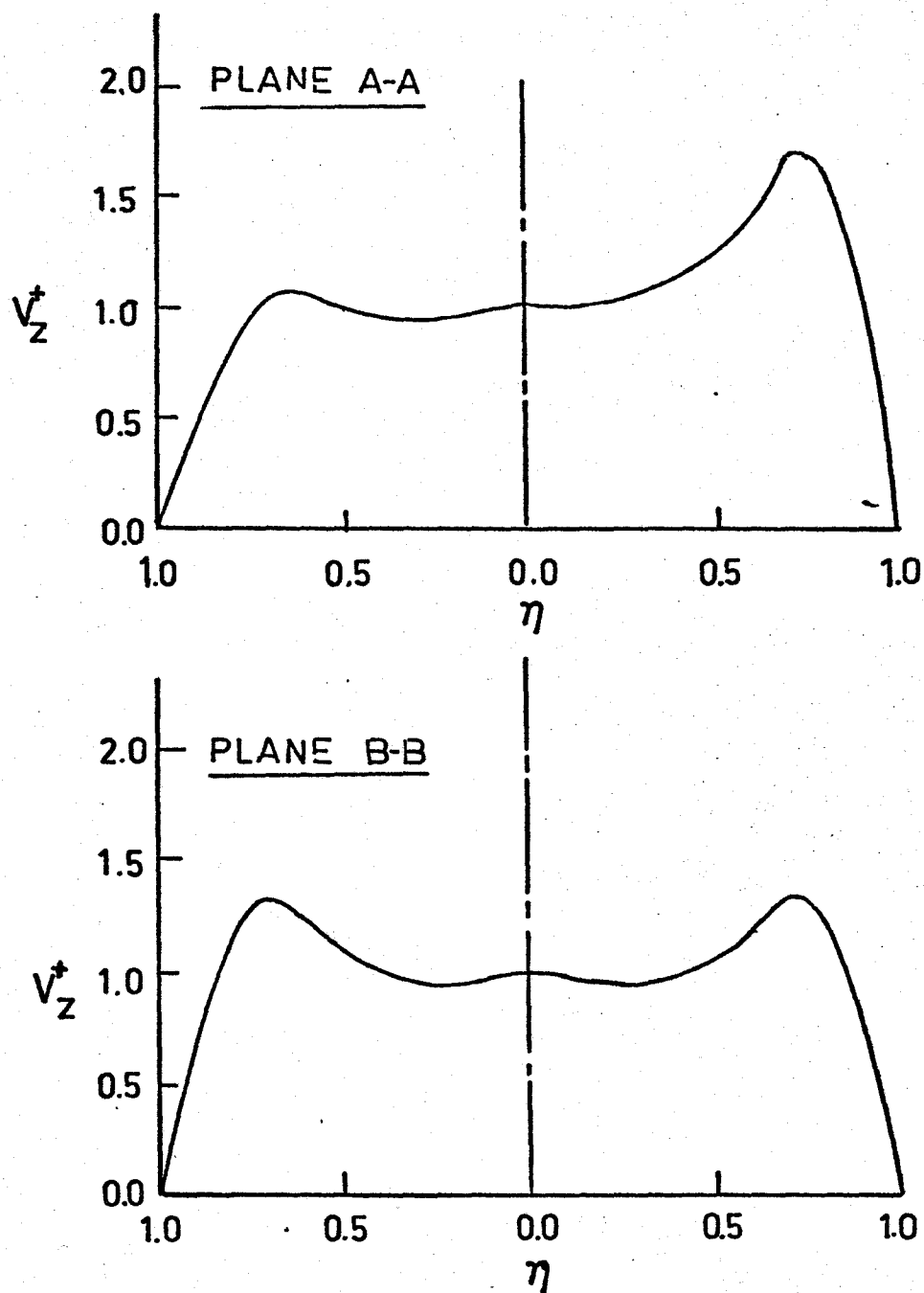


Figure 17. Non-dimensional Velocity Profiles for Experiment (II-M-2).  
( $\alpha = 1.02$ ,  $Re_N = 800$ ,  $Z/d = 4$ )

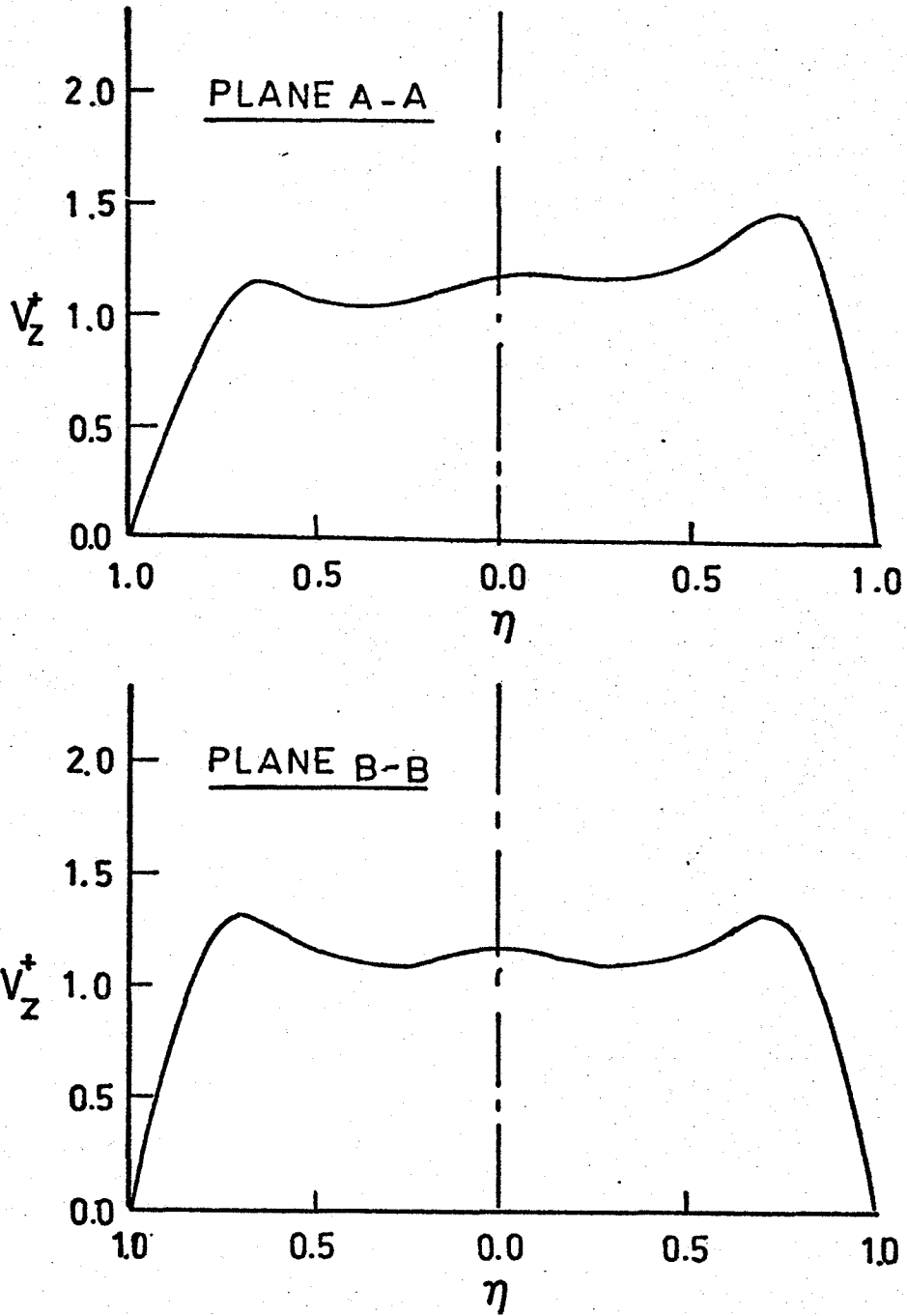


Figure 18. Non-dimensional Velocity Profiles  
for Experiment (II-M-3).  
( $\alpha = 1.02$ ,  $Re_N = 800$ ,  $Z/d = 6$ )

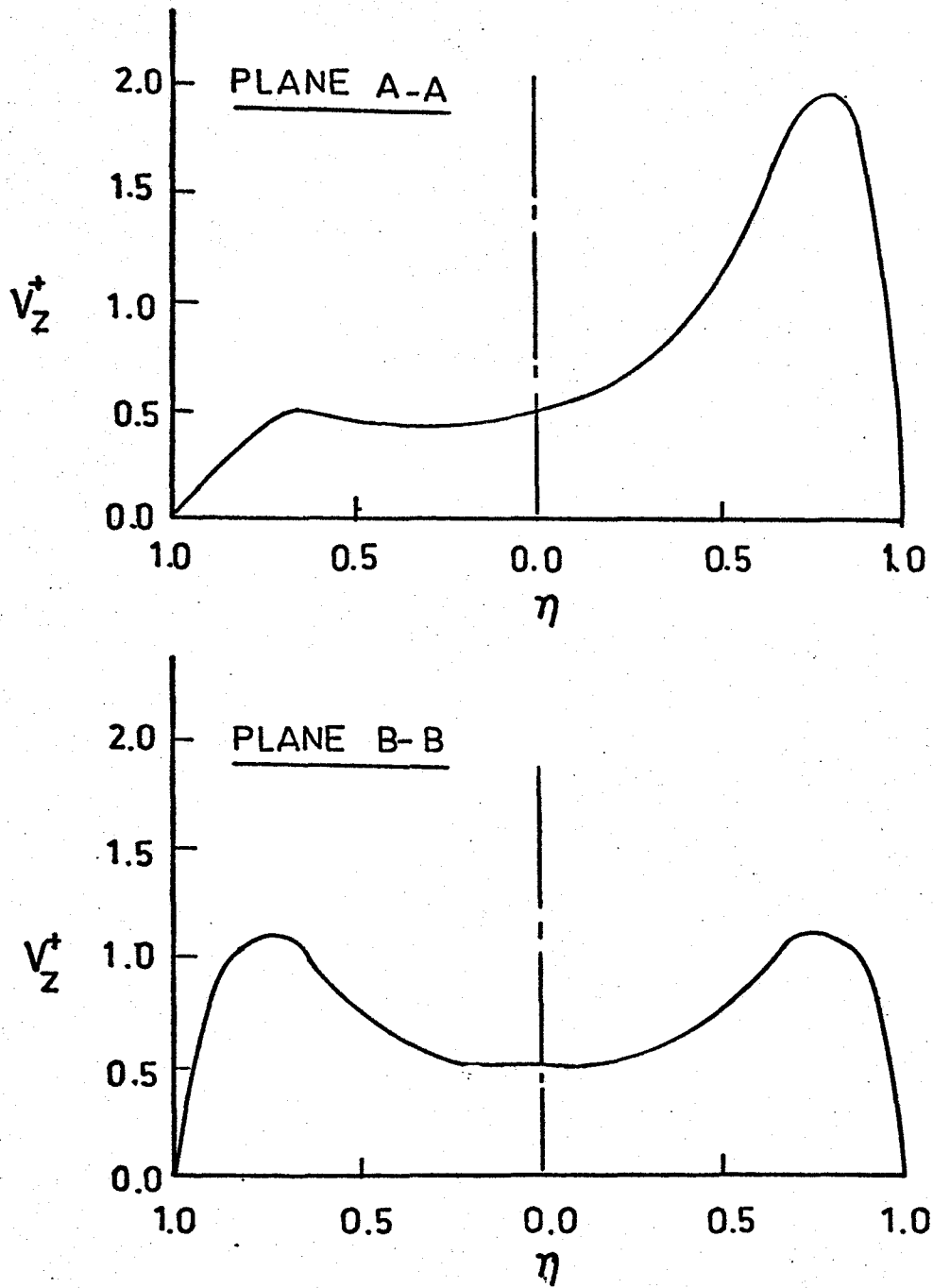


Figure 19. Non-dimensional Velocity Profiles for Experiment (III-M-1).  
( $\alpha = 1.29$ ,  $Re_N = 800$ ,  $Z/d = 2$ )

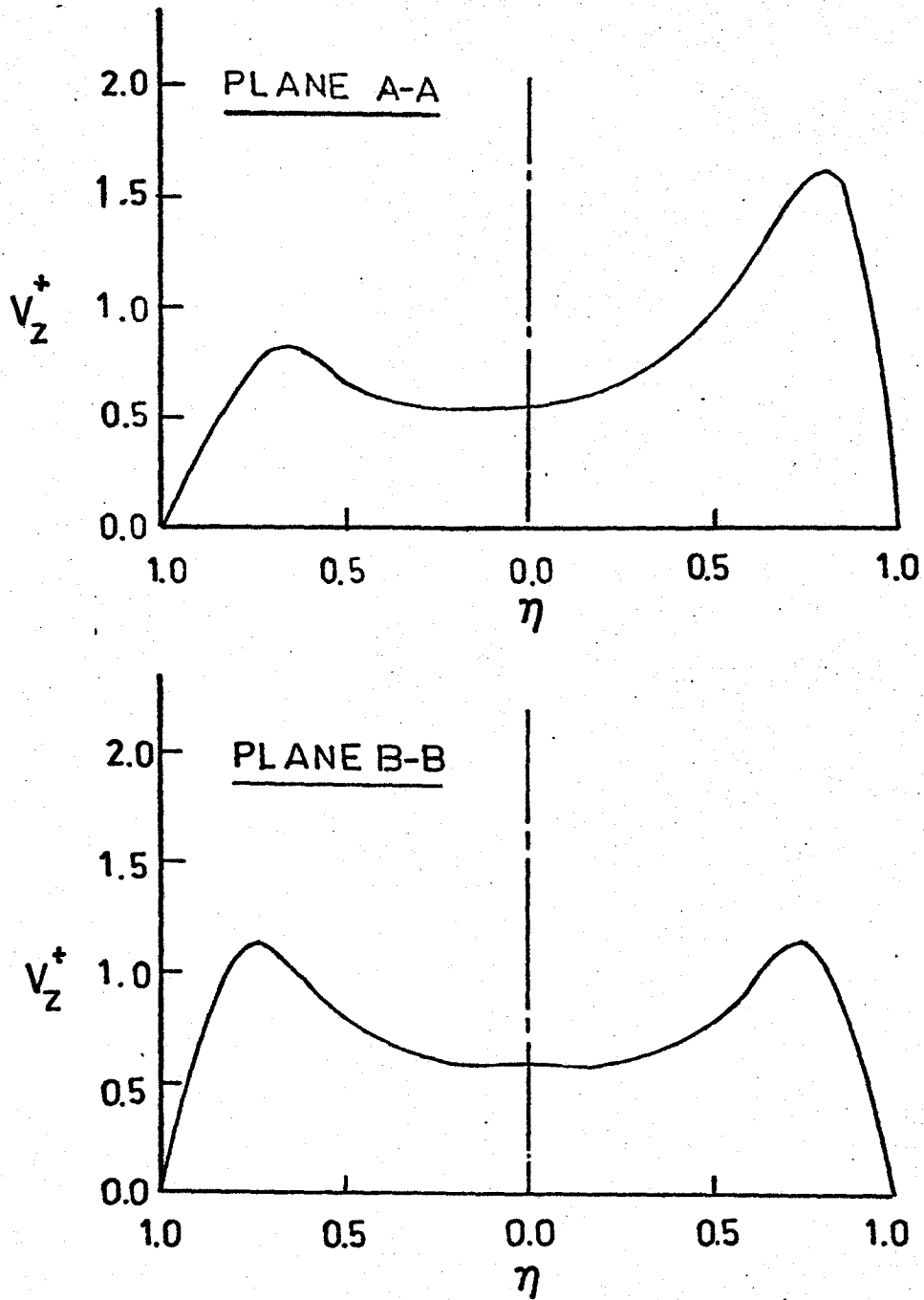


Figure 20. Non-dimensional Velocity Profiles for Experiment (III-M-2). ( $\alpha = 1.29$ ,  $Re_N = 800$ ,  $Z/d = 4$ )

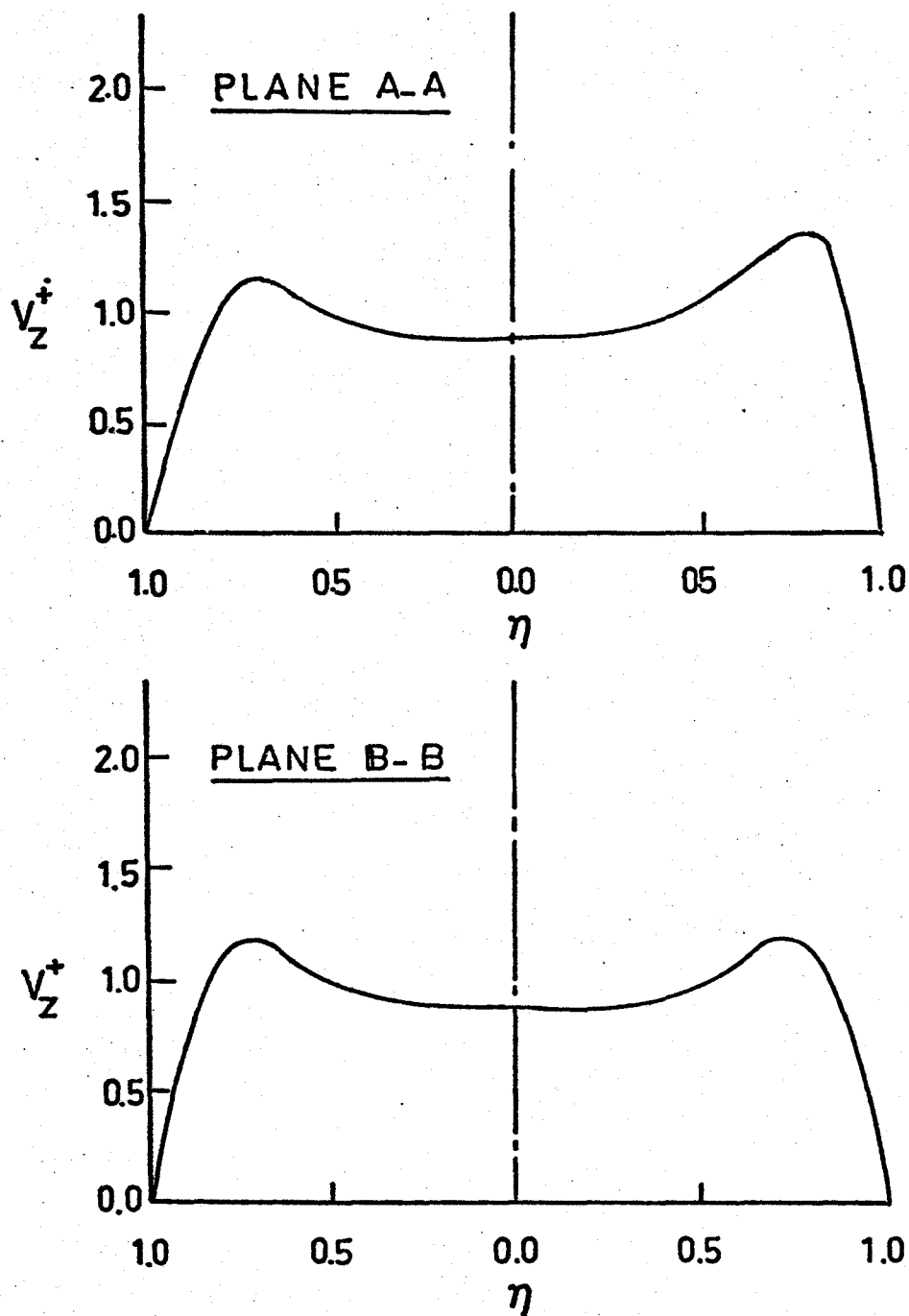


Figure 21. Non-dimensional Velocity Profiles for Experiment (III-M-3). ( $\alpha = 1.29$ ,  $Re_N = 800$ ,  $Z/d = 6$ )

drop downstream between the two limbs could divide the flow unevenly. (See Table 8 for values of  $\frac{(V_m)c}{V_m}$ ).

#### 4.2. Wall Shear Rate

Since several theories for the formation of early atherosclerotic lesions are dependent on the magnitude of wall shear rate, it was important to obtain the wall shear rate distribution along the branch daughter tube.

In general, the shear rate in laminar flow of a Newtonian fluid is defined by its components:

$$\begin{aligned}\dot{\omega}_{r\theta} &= \dot{\omega}_{\theta r} = - \left[ r \frac{\partial}{\partial r} \left( \frac{V_{\theta}}{r} \right) + \frac{1}{r} \frac{\partial V_r}{\partial \theta} \right] \\ \dot{\omega}_{z\theta} &= \dot{\omega}_{\theta z} = - \left[ \frac{\partial V_{\theta}}{\partial z} + \frac{1}{r} \frac{\partial V_z}{\partial \theta} \right] \\ \dot{\omega}_{zr} &= \dot{\omega}_{rz} = - \left[ \frac{\partial V_z}{\partial r} + \frac{\partial V_r}{\partial z} \right]\end{aligned}\tag{4.8}$$

The velocity derivatives with respect to both  $z$  and  $\theta$  are zeros at the wall. This reduces the shear rate components at the wall to

$$\begin{aligned}\dot{\omega}_{\theta r} &= - \left[ r \frac{\partial}{\partial r} \left( \frac{V_{\theta}}{r} \right) \right] \\ \dot{\omega}_{zr} &= - \left( \frac{\partial V_z}{\partial r} \right)\end{aligned}\tag{4.9}$$

It has been shown from the analysis given in Table 4 that the tangential velocity component was in general small

Experiment #	Area Ratio ( $\alpha$ )	Re <sub>N</sub>	$\frac{(V_m)_c}{V_m}$
I-L-1	0.75	394	1.02
I-L-2	0.75	404	1.06
I-L-3	0.75	404	1.08
I-M-1	0.75	825	1.08
I-M-2	0.75	803	1.07
I-M-3	0.75	803	1.09
I-H-1	0.75	1202	1.01
I-H-2	0.75	1202	1.04
I-H-3	0.75	1219	1.05
II-M-1	1.02	786	1.07
II-M-2	1.02	786	1.04
II-M-3	1.02	787	1.02
III-M-1	1.29	792	1.00
III-M-2	1.29	792	1.04
III-M-3	1.29	803	1.09

Table 8 Values of  $\frac{(V_m)_c}{V_m}$

compared to the mean axial velocity and presumably its derivatives will also be small and can be neglected.

Thus,

$$\dot{\omega} = - \left( \frac{\partial V_z}{\partial r} \right)_{\text{wall}} \quad (4.10)$$

The wall shear rate can also be written as a function of non-dimensional axial velocity.

$$\dot{\omega} = - \frac{2V_m}{d} \left( \frac{\partial V_z^+}{\partial \eta} \right)_{\eta=1.0} \quad (4.11)$$

where  $V_m$  is the mean velocity in the daughter tube and  $d$  its diameter. The non-dimensional form of the axial velocity in the outer boundary section is given by Equation (4.3). The wall shear rate around the inside wall of the branch daughter tube can be calculated from the expression

$$\dot{\omega} = C_0 (1 + C_1 \cos \theta) \quad (4.12)$$

where  $C_0 = \frac{2V_m}{d} (A_1 + 2 A_2 + 3 A_3)$

$$C_1 = A_4$$

and  $A_1$ ,  $A_2$ ,  $A_3$  and  $A_4$  are the fitted parameters of the non-dimensional velocity function (given in Table 6). Values of  $C_0$  and  $C_1$  are summarized for the fifteen locations in Table 9. Figures 22-26 show the distribution of the wall shear rate as a function of angle  $\theta$  for the locations, area ratios and Reynolds numbers studied.

Experiment	$\alpha$	$Re_N$	$Z/d$	$Z$ (cm)	$C_0$	$C_1$
I-L-1	.75	394	2	2.28	278.3430	.5130
I-L-2	.75	404	4	4.57	328.0969	.2629
I-L-3	.75	404	6	6.85	236.2703	.1805
I-M-1	.75	825	2	2.28	1007.0728	.6221
I-M-2	.75	803	4	4.57	762.8030	.3326
I-M-3	.75	803	6	6.85	613.3499	.2566
I-H-1	.75	1202	2	2.28	1830.1601	.4381
I-H-2	.75	1202	4	4.57	1787.8042	.3123
I-H-3	.75	1219	6	6.85	1720.5393	.2193
II-M-1	1.02	786	2	2.68	648.9026	.6619
II-M-2	1.02	786	4	5.36	468.7546	.3368
II-M-3	1.02	797	6	8.04	475.3613	.2792
III-M-1	1.29	792	2	3.00	555.8280	.7885
III-M-2	1.29	797	4	6.00	397.9579	.5167
III-M-3	1.29	803	6	9.01	416.8982	.2607

Table 9. Coefficients of Shear Rate Equation.  
 $\dot{\omega} = C_0 (1 + C_1 \cos\theta)$

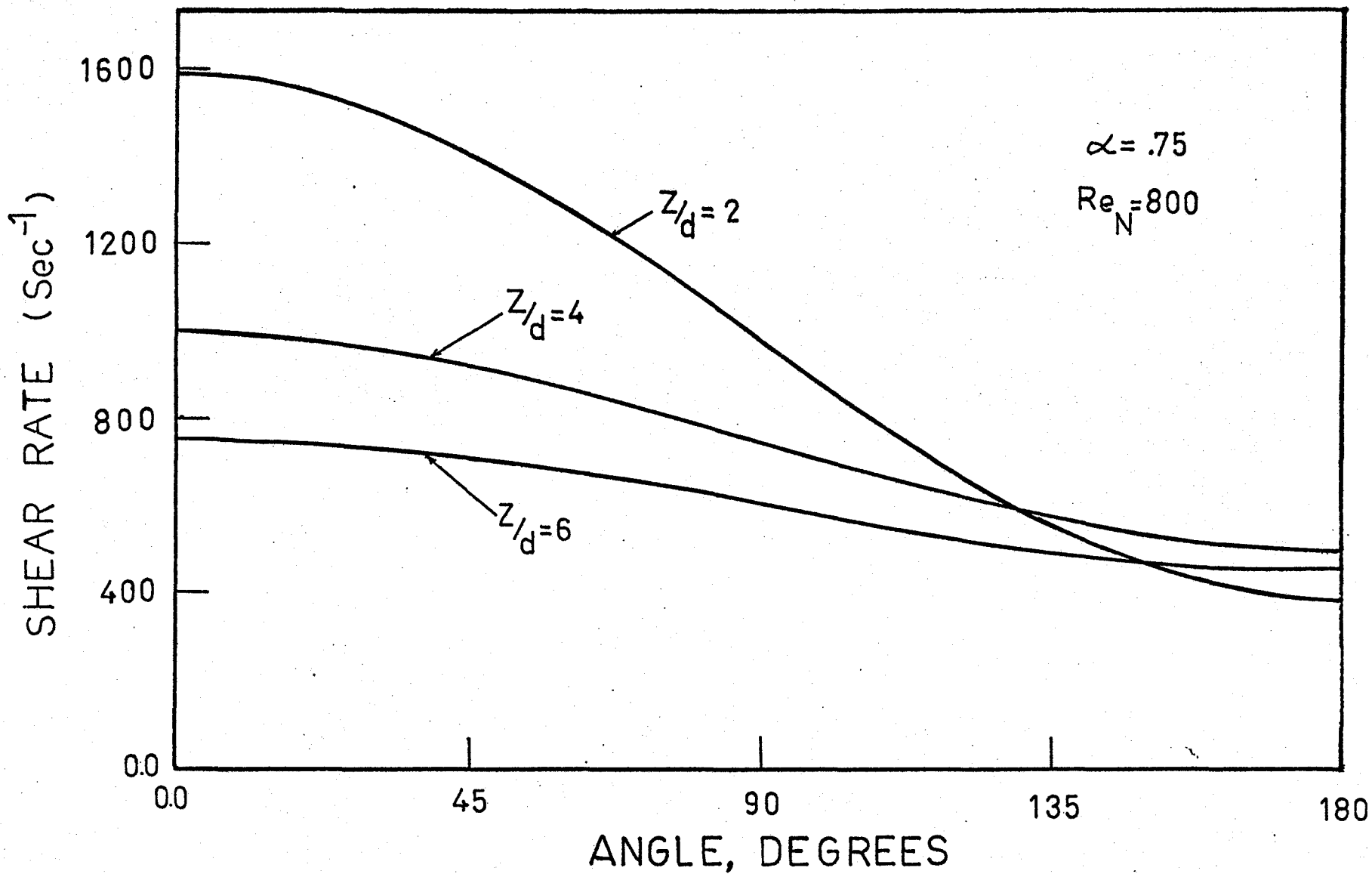


Figure 22. Wall Shear Rate Distribution around the Daughter Tube.

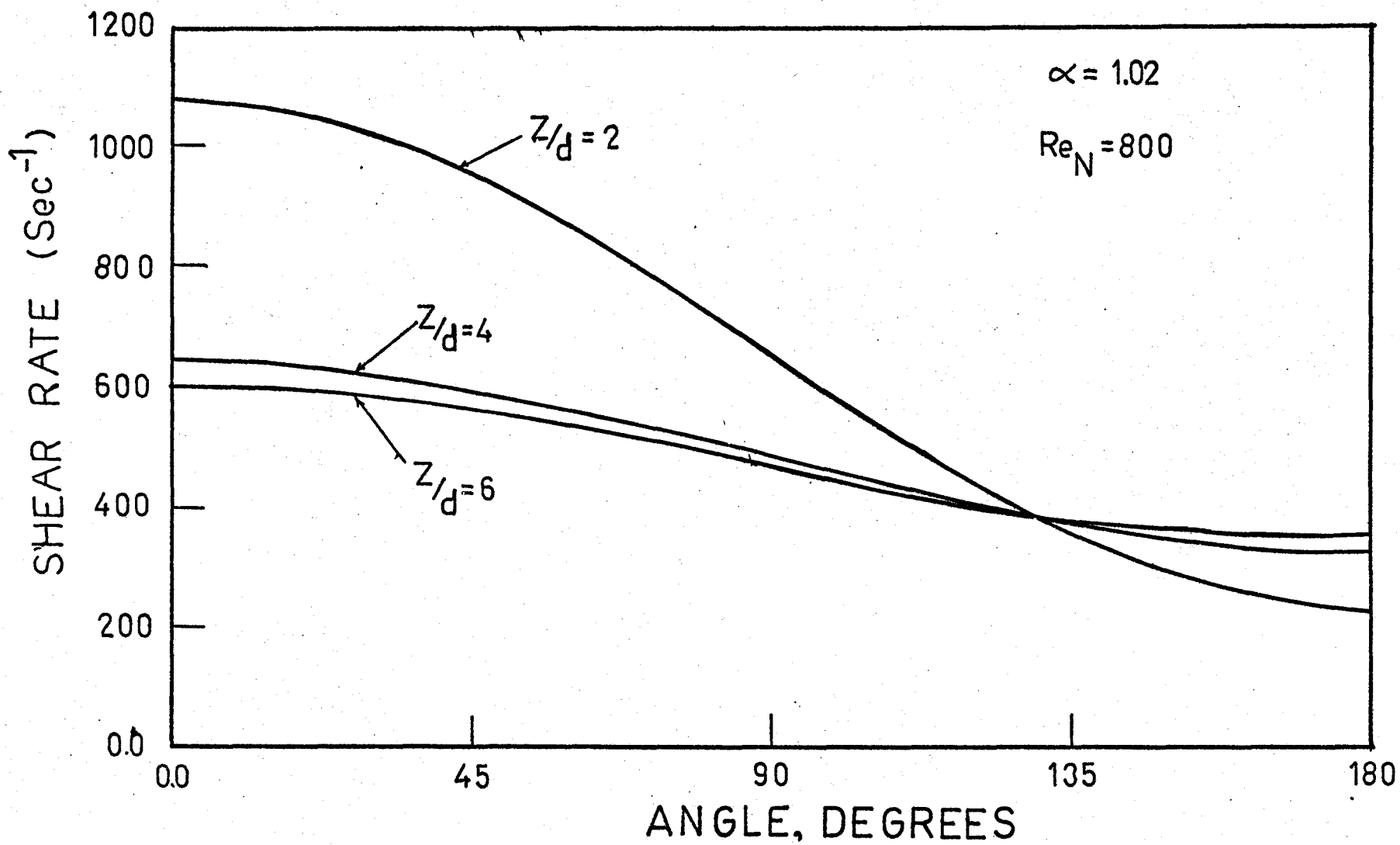


Figure 23. Wall Shear Rate Distribution around the Daughter Tube.

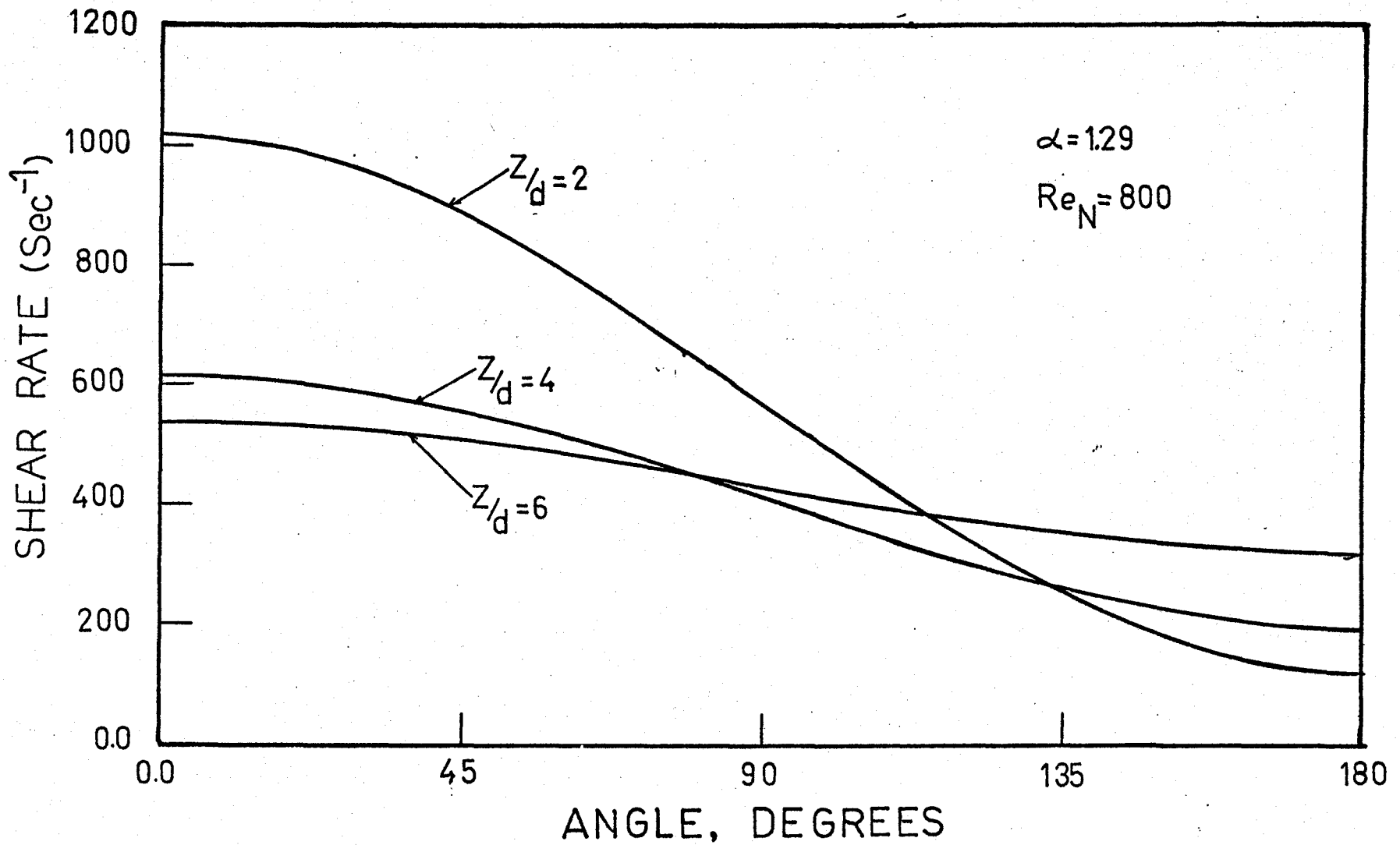


Figure 24. Wall Shear Rate Distribution around the Daughter Tube.

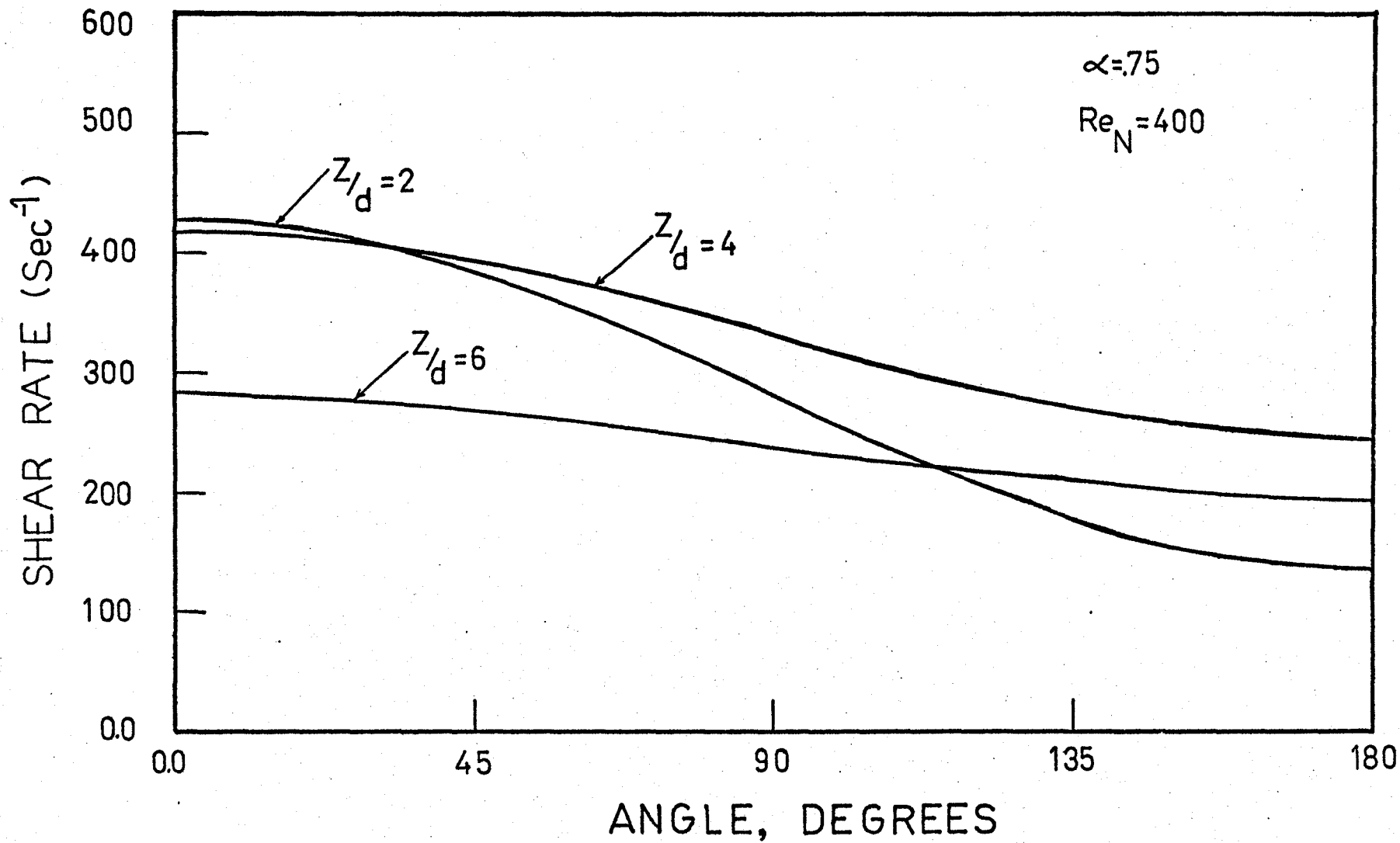


Figure 25. Wall Shear Rate Distribution around the Daughter Tube.

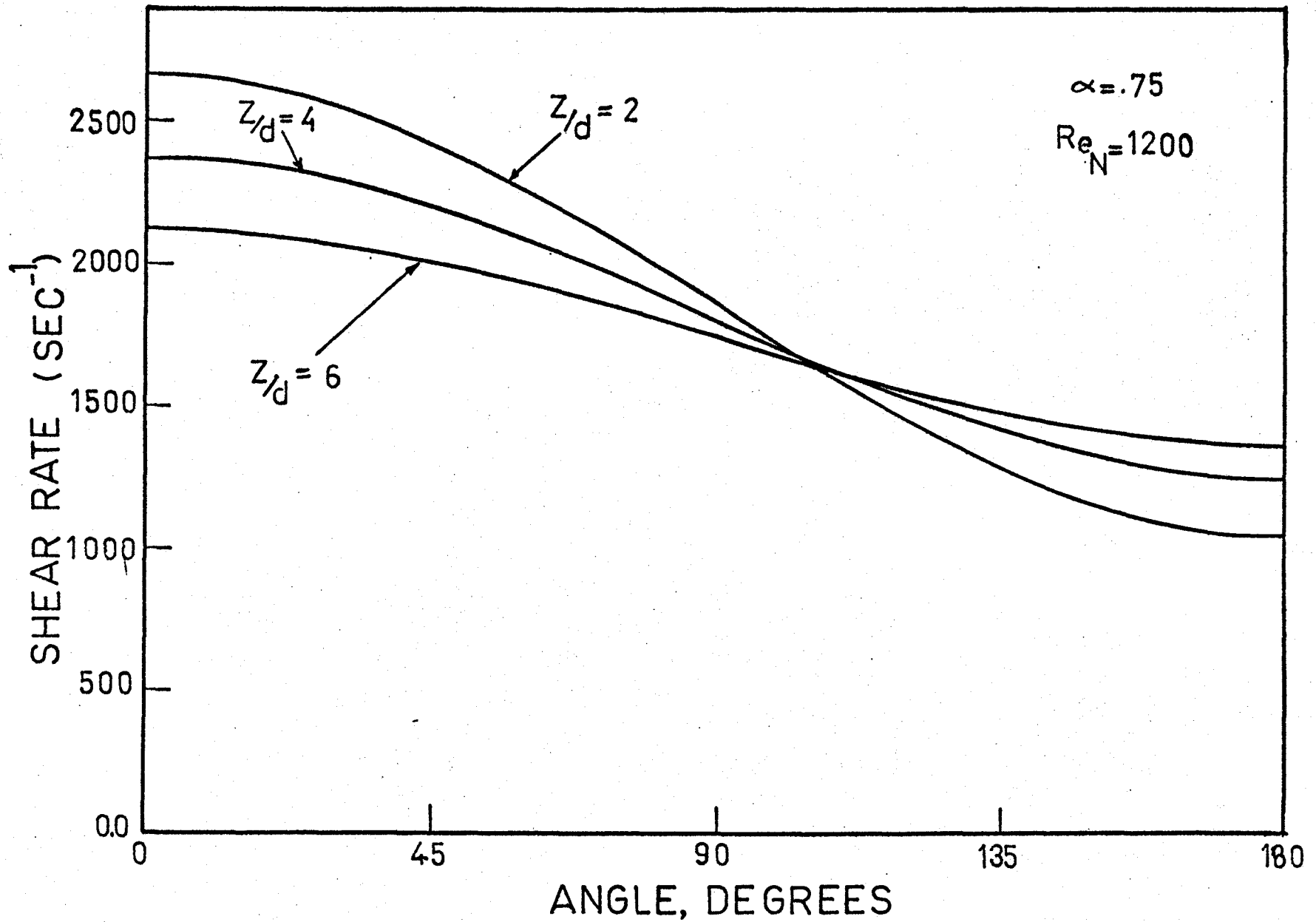


Figure 26. Wall Shear Rate Distribution around the Daughter Tube.

## CHAPTER 5

### ANALYSIS AND DISCUSSION

#### 5.1. Axial Velocity Development

The carina splits the oncoming parabolic flow diverting half down each daughter tube. Thus, at the beginning of each daughter tube the velocity profile is expected to be akin to a distorted paraboloid with the peak near the inside wall of the daughter tube and a low axial velocity region near the outside wall (see branch notation). As the flow moves downstream, the high peak starts to convect tangentially towards the low velocity region. The high peak extends around the outside of the tube within a narrow band of  $\eta$  value, giving rise to two symmetric peaks in plane B-B and a small peak near the outside wall in plane A-A. This can be seen from the velocity profiles in plane A-A and plane B-B. Figures 27 and 28 show a typical axial velocity development in the plane of the bifurcation (A-A) and the plane normal to the plane of the bifurcation (B-B) respectively.

With distance downstream, the flow convects fluid tangentially from the region near the inside wall (carina side) to the region near the outside wall trying to balance the mass flow rate distribution over the tube cross-section. This results in the two-peaked velocity profile in plane A-A at positions  $Z/d = 4$  and  $Z/d = 6$ . At the same time

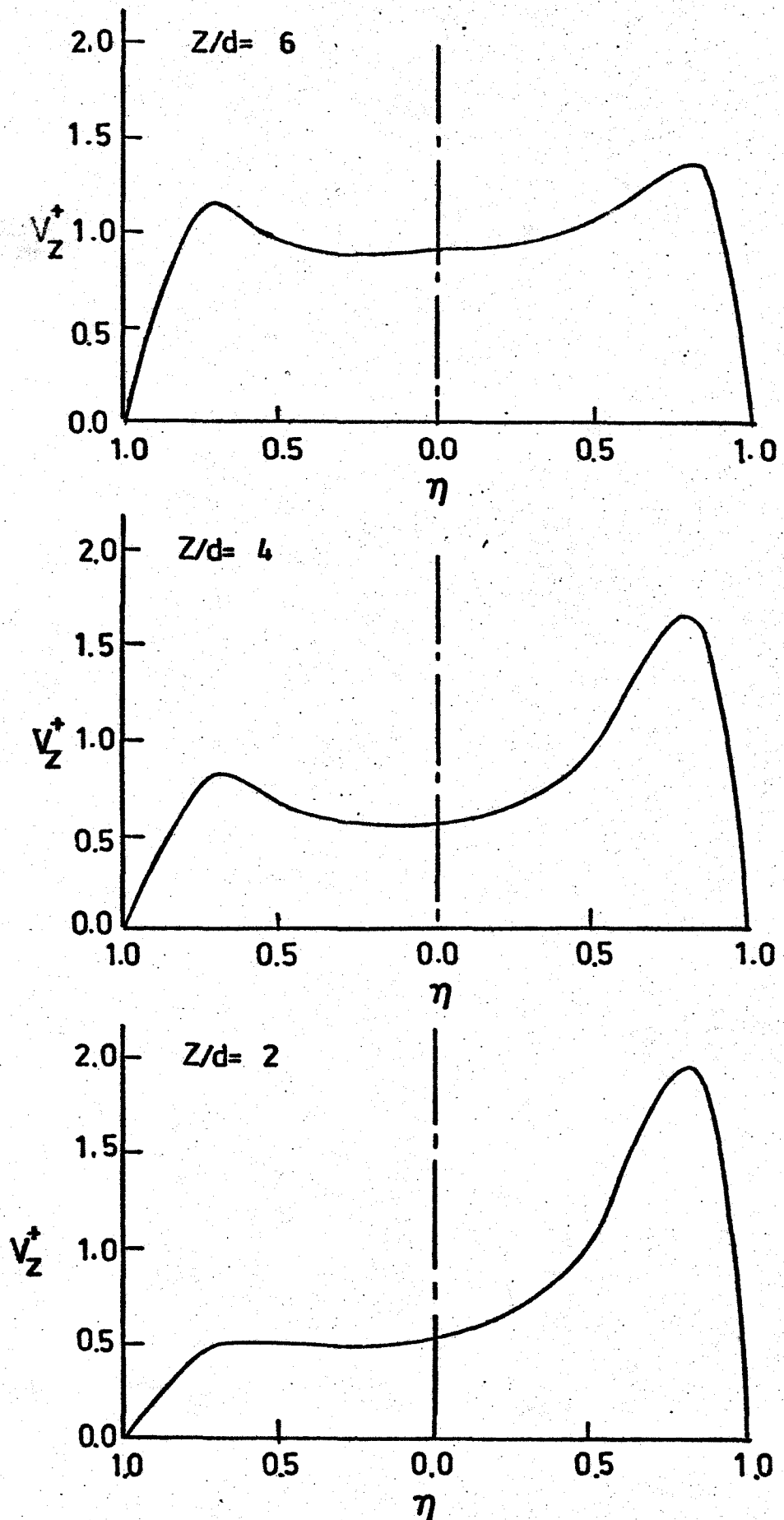


Figure 27.  
Axial Velocity Development in Plane A-A. ( $\alpha = 1.29$ ,  $Re_N = 800$ )

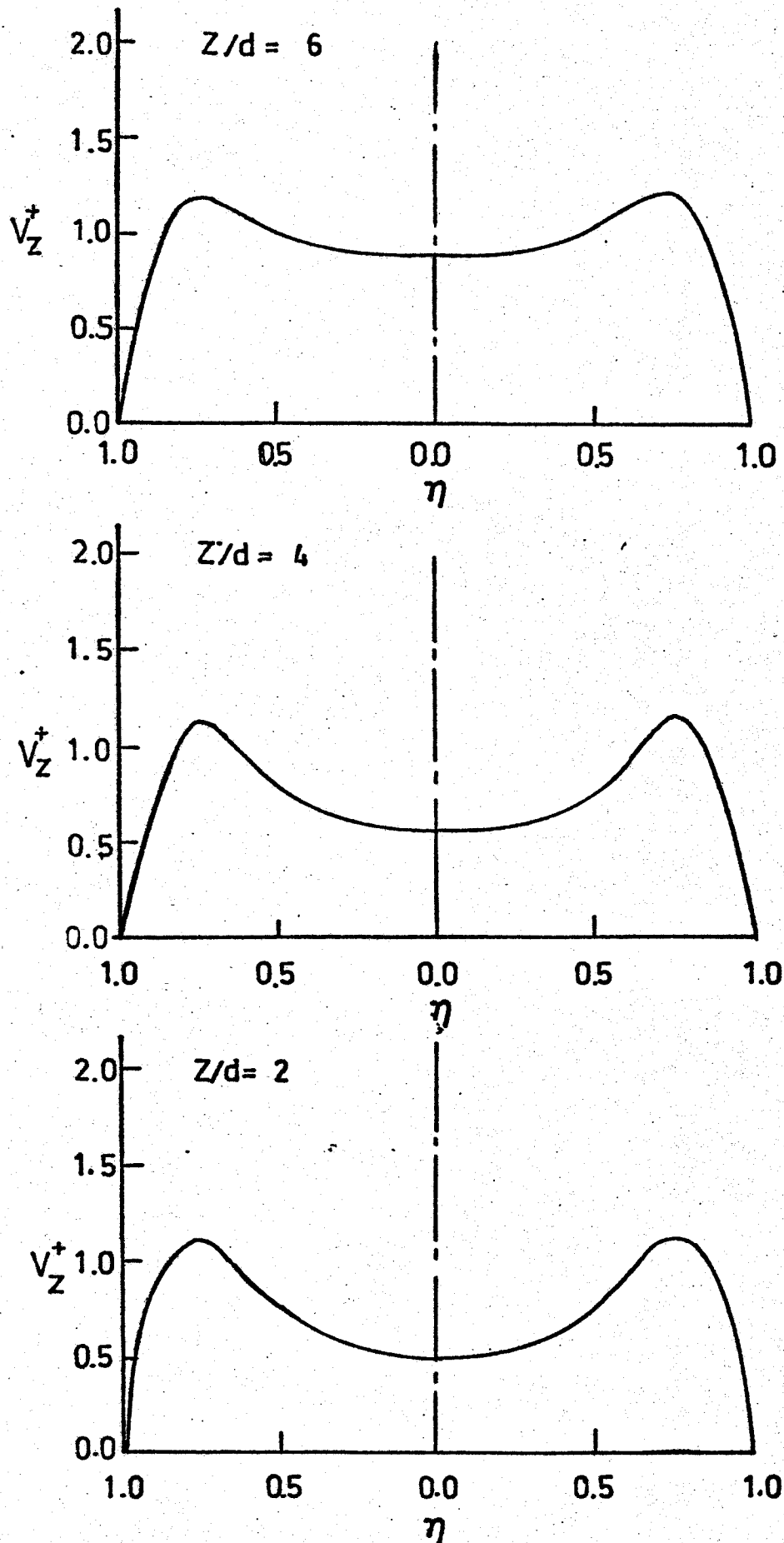


Figure 28.  
Axial Velocity Development in Plane B-B. ( $\alpha = 1.29$ ,  $Re_N = 800$ )

viscous action increases the centreline velocity. At position  $Z/d = 6$ , the profiles are almost axially symmetric.

In general, the velocity profiles obtained in this study were similar to those obtained by Schroter and Sudlow (2) and Brech (9). Schroter and Sudlow have obtained velocity profiles downstream of a  $70^\circ$  branch with area ratio 1.22 and at Reynolds numbers 450 and 1090 (based on parent tube) using a hot-wire anemometer. Their velocity profiles at  $Z/d = 2$  downstream for Reynolds number 1090 showed a high peak near the inside wall and a smaller peak near the outside in the plane of the bifurcation and two symmetric peaks in the plane normal to the plane of the bifurcation. Brech (9) also obtained velocity profiles downstream of a  $90^\circ$  branch with area ratio 1.15 at Reynolds numbers 390, 780 and 1550 (based on parent tube). His profiles also show the same shape of multiple peaks, as shown in this study, by 6 diameters downstream from the carina.

#### 5.1.1. Effect of Cross-Sectional Area Ratio

With an input Reynolds number 800, the velocity profiles at  $Z/d = 2$  in the three models, with area ratios .75, 1.02 and 1.29, showed the same general shape. In each case, there was a velocity peak near the inside wall of the tube and a low axial velocity region near the outside wall. The high peak was approximately twice the mean axial velocity. At location  $Z/d = 4$  the high peak dropped to a value approximately equal to  $1.8 V_m$  and a new peak started to form near the

outside wall. At the same time the centreline velocity increased. The increase of the centreline velocity in the accelerating flow ( $\alpha < 1$ ) was found to be more rapid than that in the decelerating flow ( $\alpha > 1$ ). Figure 29 shows the axial velocity development in model I ( $\alpha = 0.75$ ). At position  $Z/d = 6$  a significant difference can be seen when comparing the velocity profiles for model III (Figure 27) and model I (Figure 29). In model I the two peaks were shifted towards the tube centre, though the peak near the inside wall was still relatively high ( $1.65 V_m$ ). In contrast, the velocity profile in model III showed an almost flat profile for  $0 \leq \eta \leq 0.5$ . The high peak near the inside wall dropped to a value approximately  $1.4 V_m$ . This shows that the accelerating flow ( $\alpha < 1$ ) may help in shifting the high velocity peak towards the centre of the tube while not decreasing its value significantly. The decelerating flow ( $\alpha > 1$ ), over the same dimensionless distance, helps in flattening the velocity profile in the central region while creating an axially symmetric profile.

#### 5.1.2. Effect of Parent Tube Reynolds Number

The effect of the parent tube Reynolds number on the flow development can be seen from Figure 30, which shows the flow development in model I ( $\alpha = 0.75$ ) at Reynolds number 400, and Figure 31, which shows the flow development in the same model at Reynolds number 1200. At position  $Z/d = 2$ , the velocity profile showed a high peak near the

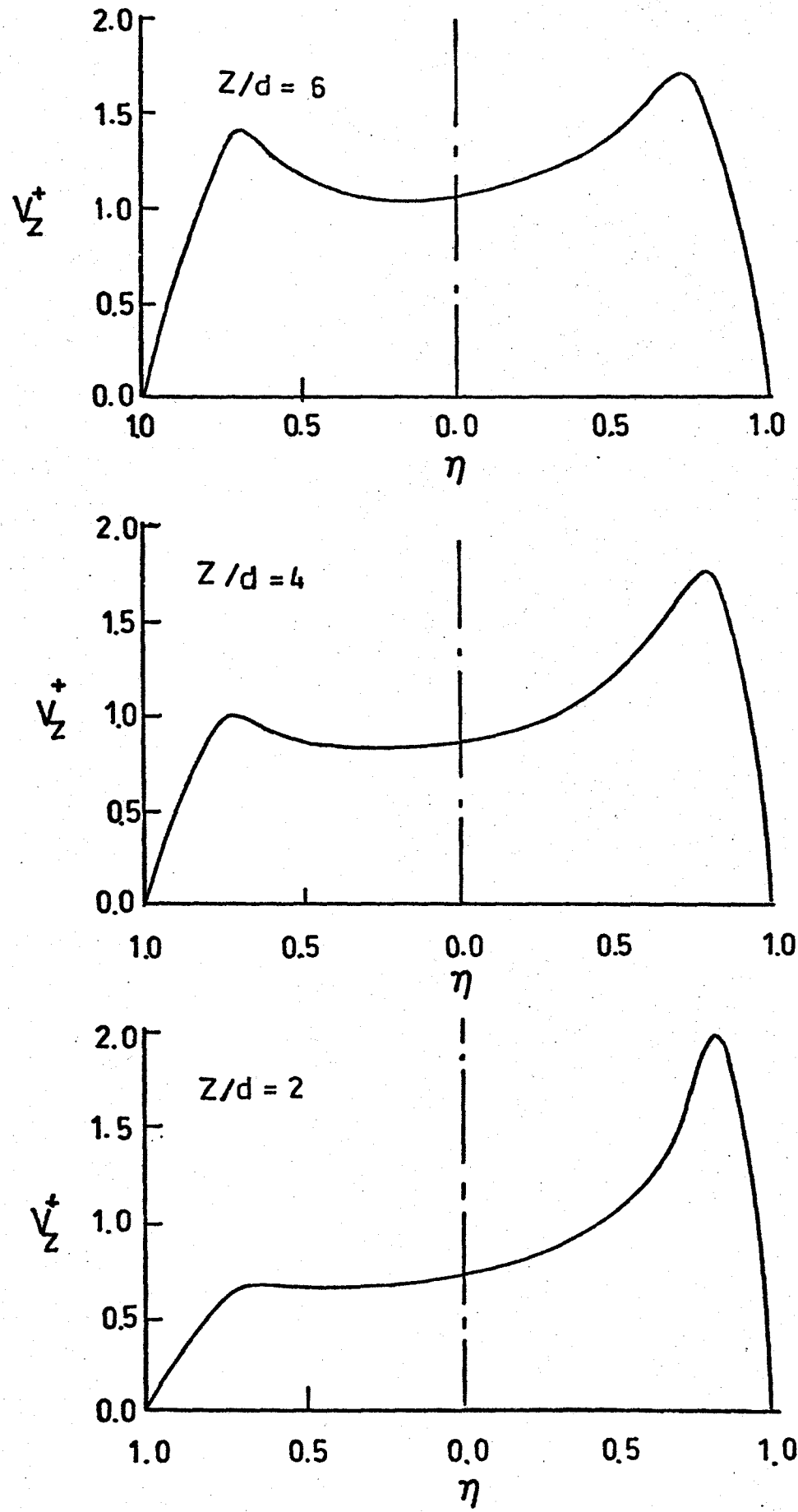


Figure 29. Axial Velocity Development in Plane A-A.  
( $\alpha = 0.75, Re_N = 800$ )

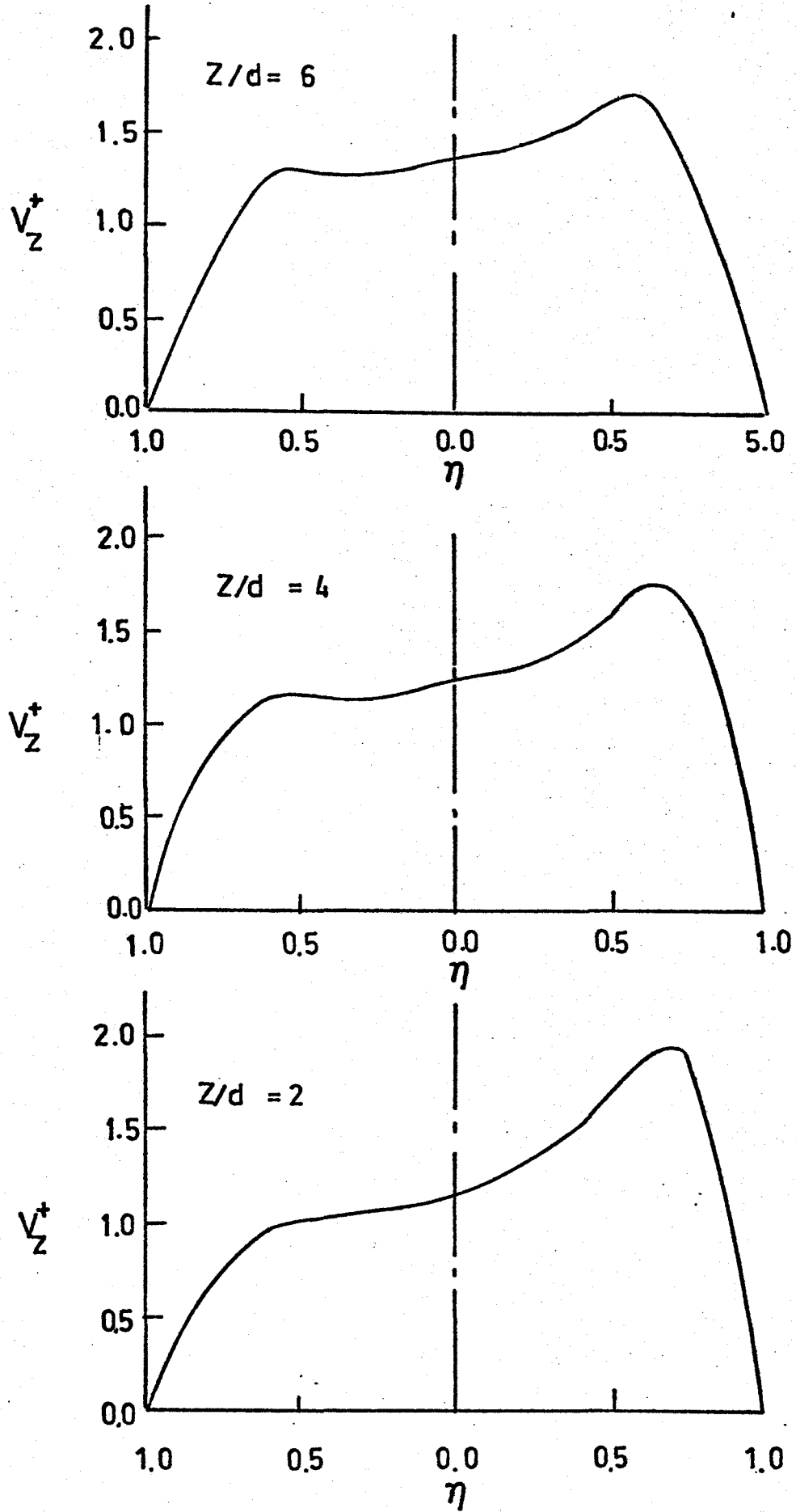


Figure 30. Axial Velocity Development in Plane A-A. ( $\alpha = 0.75, Re_N = 400$ )

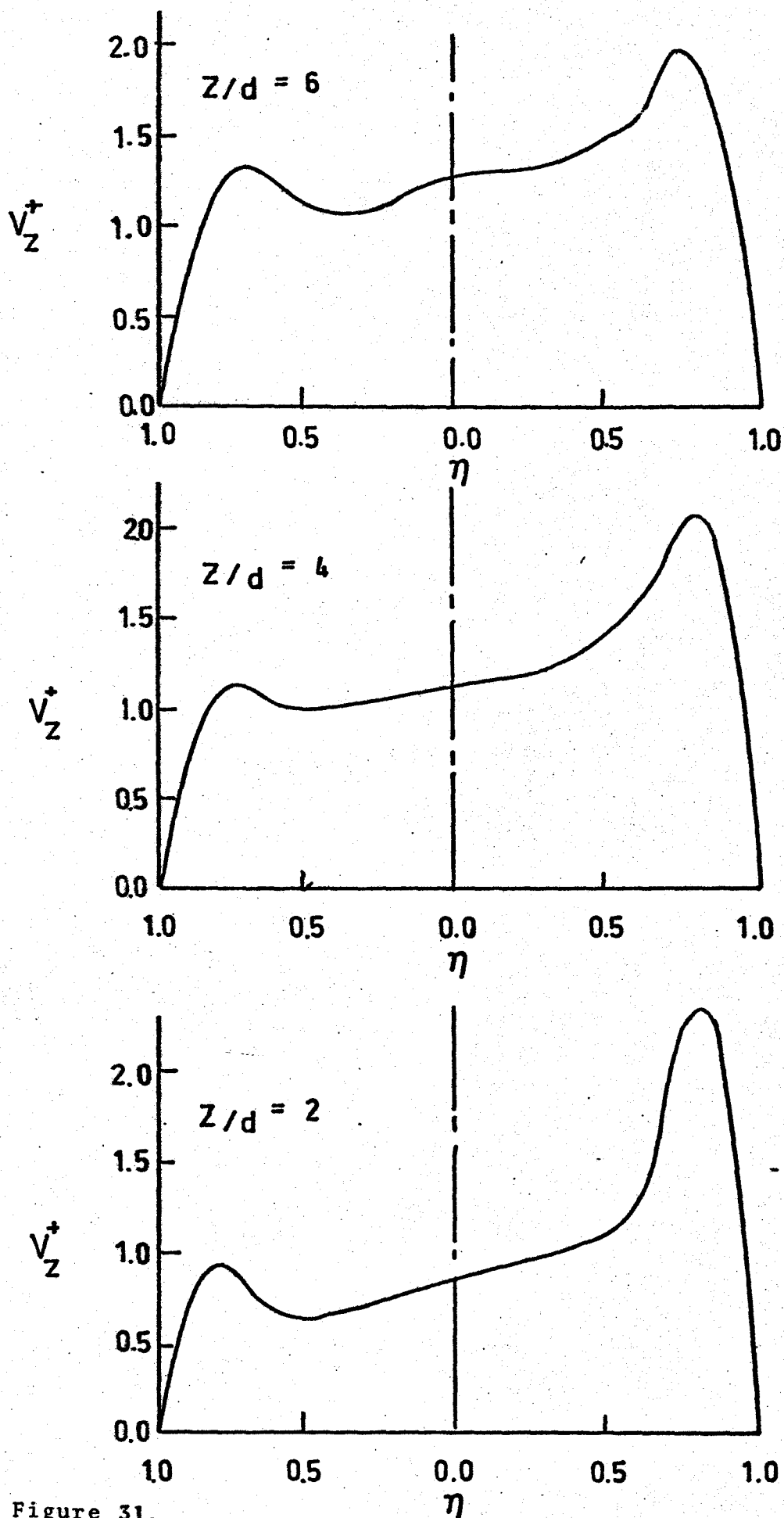


Figure 31.  
Axial Velocity Development in Plane A-A. ( $\alpha = 0.75$ ,  $Re = 1200$ )

inside wall ( $2.3 V_m$ ) for the higher Reynolds number with a small peak near the outside wall. For the lower Reynolds number, there was a high peak ( $1.9 V_m$ ) near the inside wall with no smaller peak near the outside wall. As the flow moved downstream, one can see that the flow for the low Reynolds number developed more rapidly towards the expected parabolic profile than the flow for the high Reynolds number. At position  $Z/d = 6$ , the high Reynolds number profile still showed a distinct peak near the outside wall while the profile for the lower Reynolds number showed a tendency to develop towards the parabolic profile.

## 5.2. Wall Shear Rate Distribution

Several workers have proposed a relationship between wall shear rate and the formation of atheroma at certain focal regions near branches. It is therefore important to examine the wall shear rate around and along the branch daughter tube and compare its values with the developed flow values upstream and downstream of the branch.

The wall shear rate for fully developed flow in a circular tube can be calculated from the expression

$$\dot{\omega} = \frac{8 V_m}{d} \quad (5.1)$$

where  $V_m$  is the flow mean velocity and  $d$  is the tube diameter. Table 10 gives the wall shear rate values for developed flow in the parent and daughter tubes at the conditions of this study.

Model	Area Ratio ( $\alpha$ )	Flowrate <sup>+</sup> (cm <sup>3</sup> /sec)	D (cm)	d (cm)	Developed Shear Rate (sec <sup>-1</sup> )	
					$\dot{\omega}$ parent	$\dot{\omega}$ daughter
I	.75	44.4	1.867	1.142	69	151
I	.75	85	1.867	1.142	133	288
I	.75	122	1.867	1.142	191	415
II	1.02	85	1.867	1.339	133	182
III	1.29	85	1.867	1.501	133	130

+ Total flowrate in the parent tube

Table 10 Developed Wall Shear Rate Values.

At constant axial position, the wall shear rate as a function of  $\theta$  can be approximated by a displaced cosine function (Figures 22-26). The highest shear rate always occurred on the inside wall of the daughter tube ( $\theta=0.0^\circ$ ) and the lowest on the outside wall ( $\theta=180^\circ$ ). This qualitatively agrees with the work of Brech (9). The shear rate values on the top and bottom of the cross-section were midway between the values at the inside and outside walls.

The longitudinal distribution of wall shear rate along the daughter tube can be seen from Figures 32-36. Wall shear rates were plotted as a function of non-dimensional axial position  $Z/d$  for the inside wall (I.W.), outside wall (O.W.) and top and bottom (T. & B).

#### 5.2.1. Effect of Cross-Sectional Area Ratio on Wall Shear Rate Distribution

Figures 32-34 show the longitudinal wall shear rate distribution in the three models studied for Reynolds number 800.

The largest positive deviation from the developed daughter and parent tube values was found on the inside wall of the smallest area ratio bifurcation and the lowest value was found on the outside wall of the largest area ratio bifurcation. Extrapolating the shear rate curve on the outside wall of the largest area ratio model (Figure 34) back to  $Z/d = 0$ , indicates the possible presence of a wall shear rate close to zero along with the possibility of flow reversal. The same curve for the lower area ratio model did not indicate

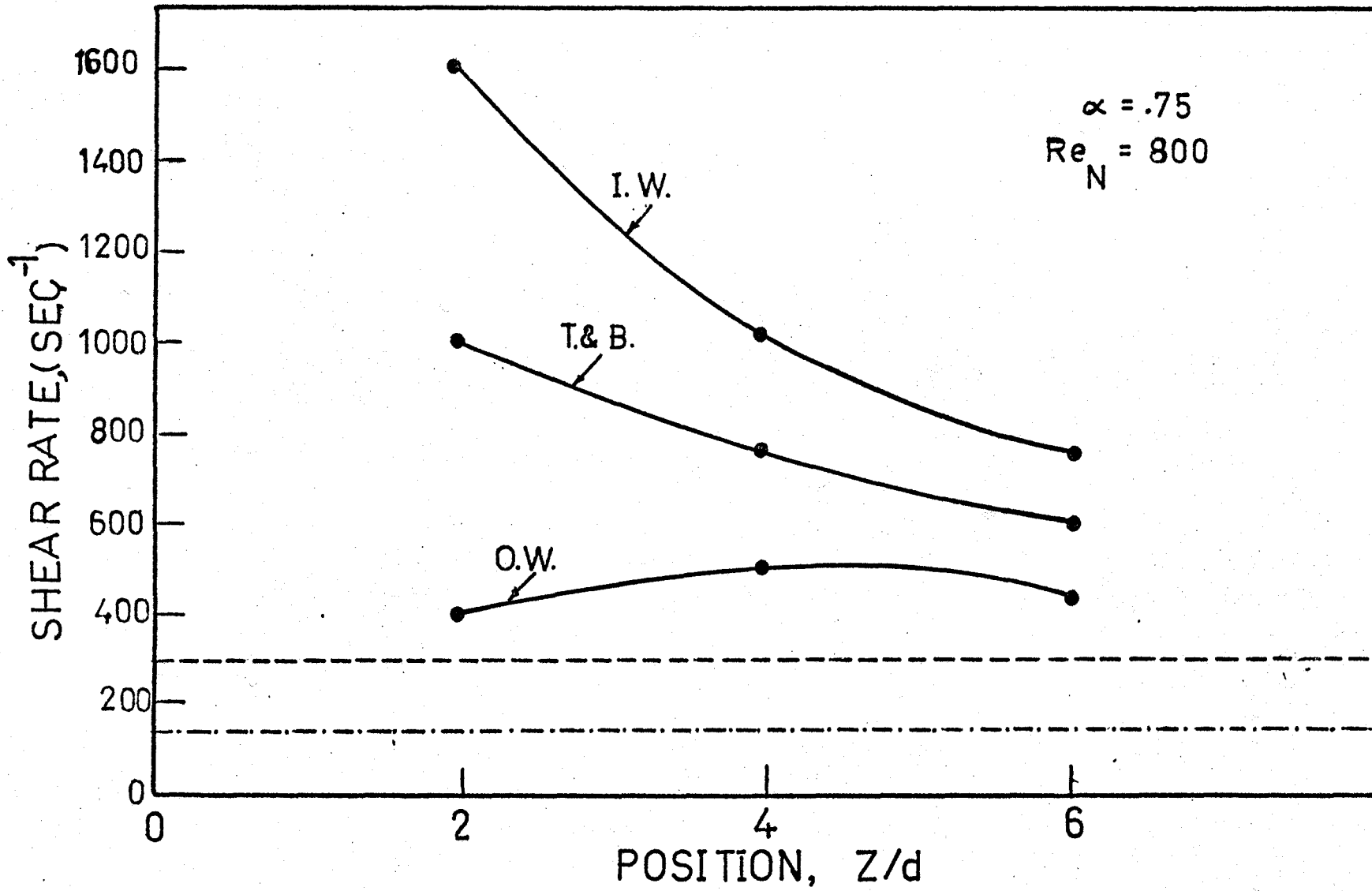


Figure 32. Longitudinal Wall Shear Rate Distributions.  
 (----- Parent Tube and ----- Daughter  
 Tube Developed Values)

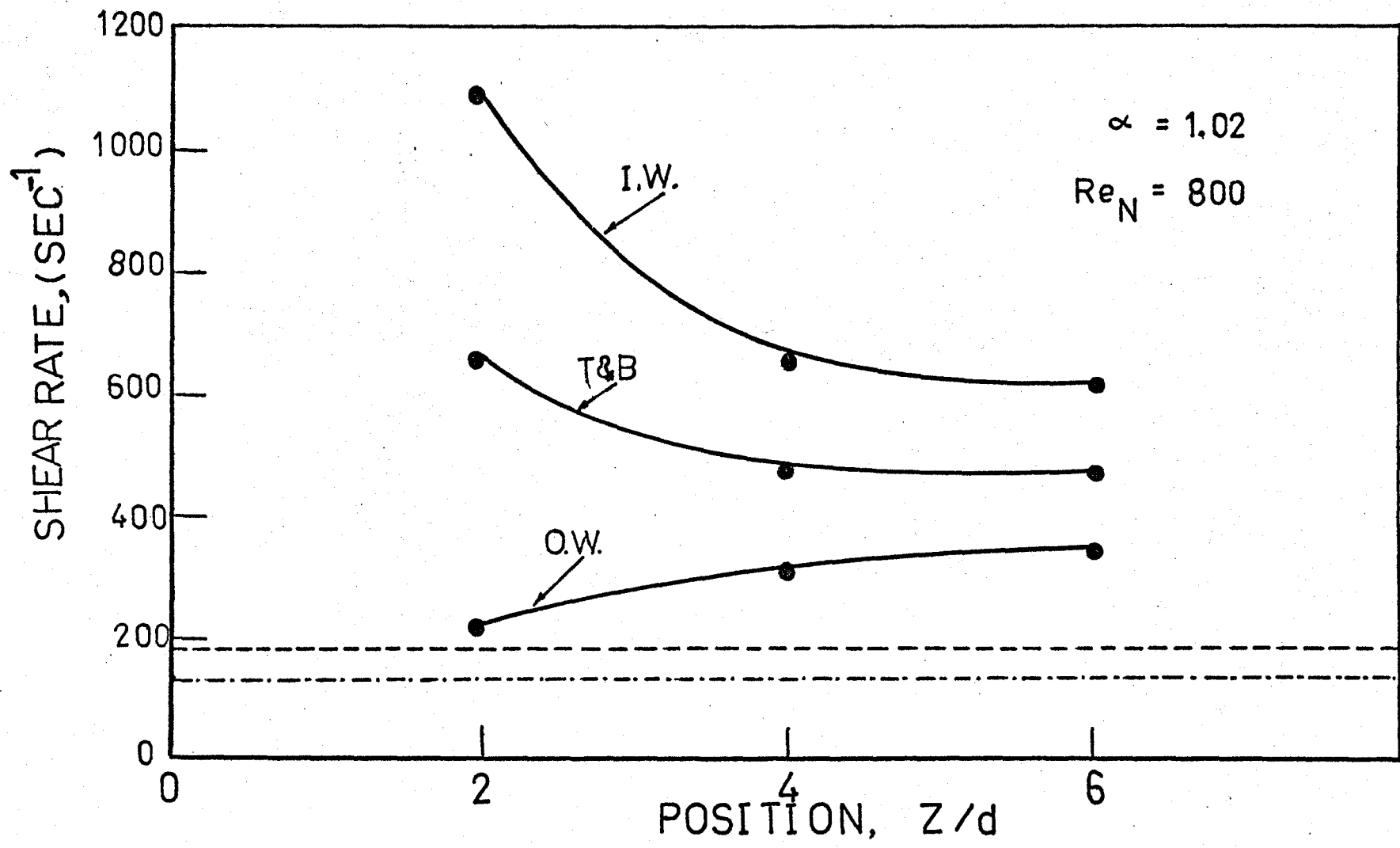


Figure 33. Longitudinal Wall Shear Rate Distributions.  
 (----- Parent Tube and ----- Daughter Tube Developed Values)

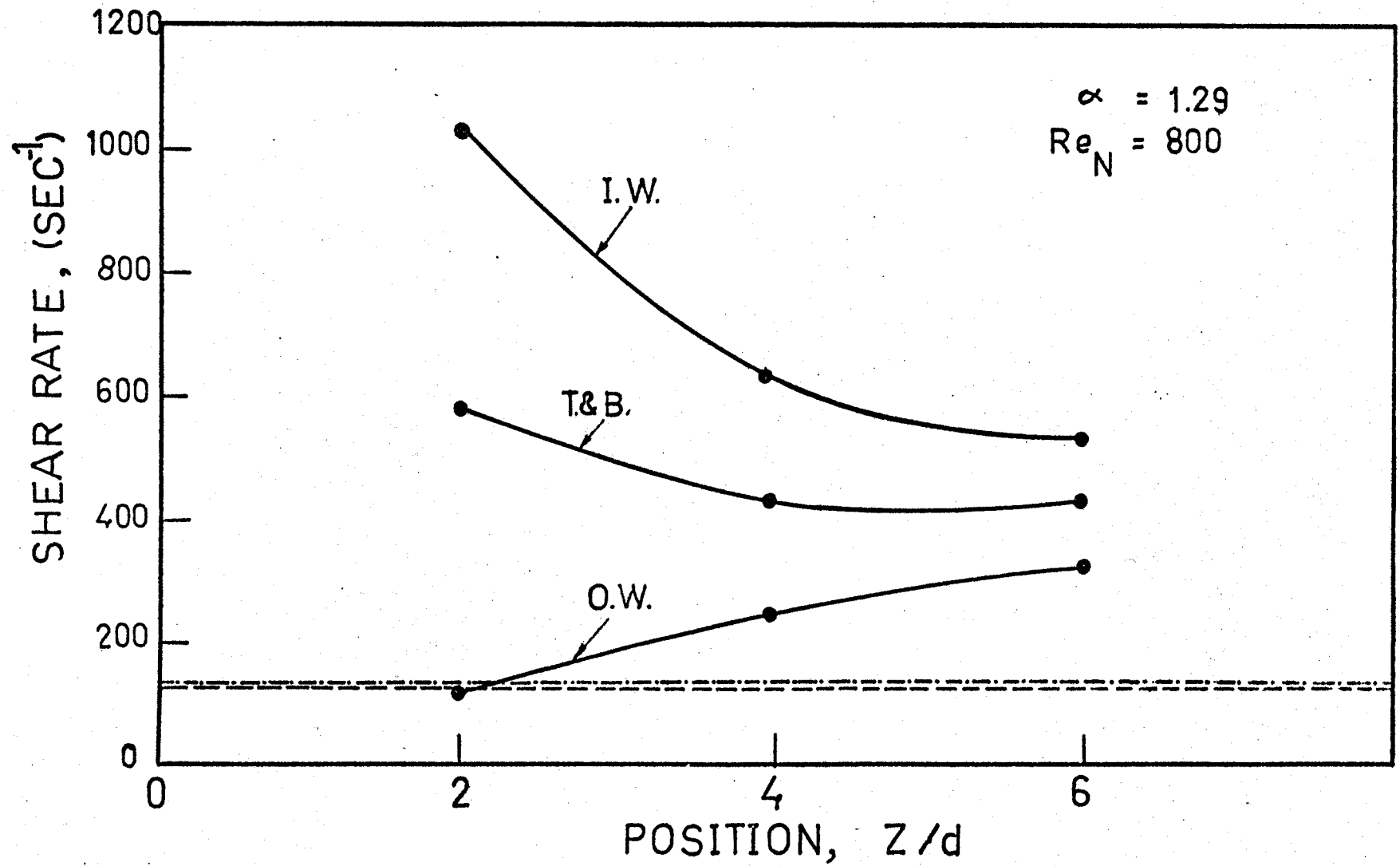


Figure 34. Longitudinal Wall Shear Rate Distributions.  
 (----- Parent Tube and -.-.-.- Daughter Tube Developed Values)

this possibility. One may speculate that boundary layer separation is most likely to occur in bifurcations with large area ratios ( $\alpha > 1$ ).

With distance downstream the shear rate on the inside wall continued to decrease approaching the developed value in the daughter tube asymptotically. On the outside wall the shear rate was lower than the developed value in the region between the carina and  $Z/d = 2$ . It then increased to higher values with distance downstream. However, this increase was followed by an observed decrease only in the case of the large area ratio model ( $\alpha = 1.29$ ). This decrease, towards the daughter tube developed value, is also expected for the other two area ratio models further downstream. Brech (9) claims for all the conditions he studied that the shear stress on the outside wall reaches and maintains the developed value within one diameter downstream of the carina. This was not observed in any case studied in this work.

#### 5.2.2. Effect of Reynolds Number on Wall Shear Rate Distribution

Figures 35 and 36 show the shear rate distributions in model I ( $\alpha = 0.75$ ) for Reynolds numbers 400 and 1200 respectively. For Reynolds number 1200, the highest wall shear rate value was approximately  $2800 \text{ sec}^{-1}$  compared to a value of  $425 \text{ sec}^{-1}$  at the same position ( $Z/d = 2$ ) for Reynolds number 400. This indicates that wall shear rate increases with increasing Reynolds number. The relation between wall shear rate and Reynolds number is not a simple

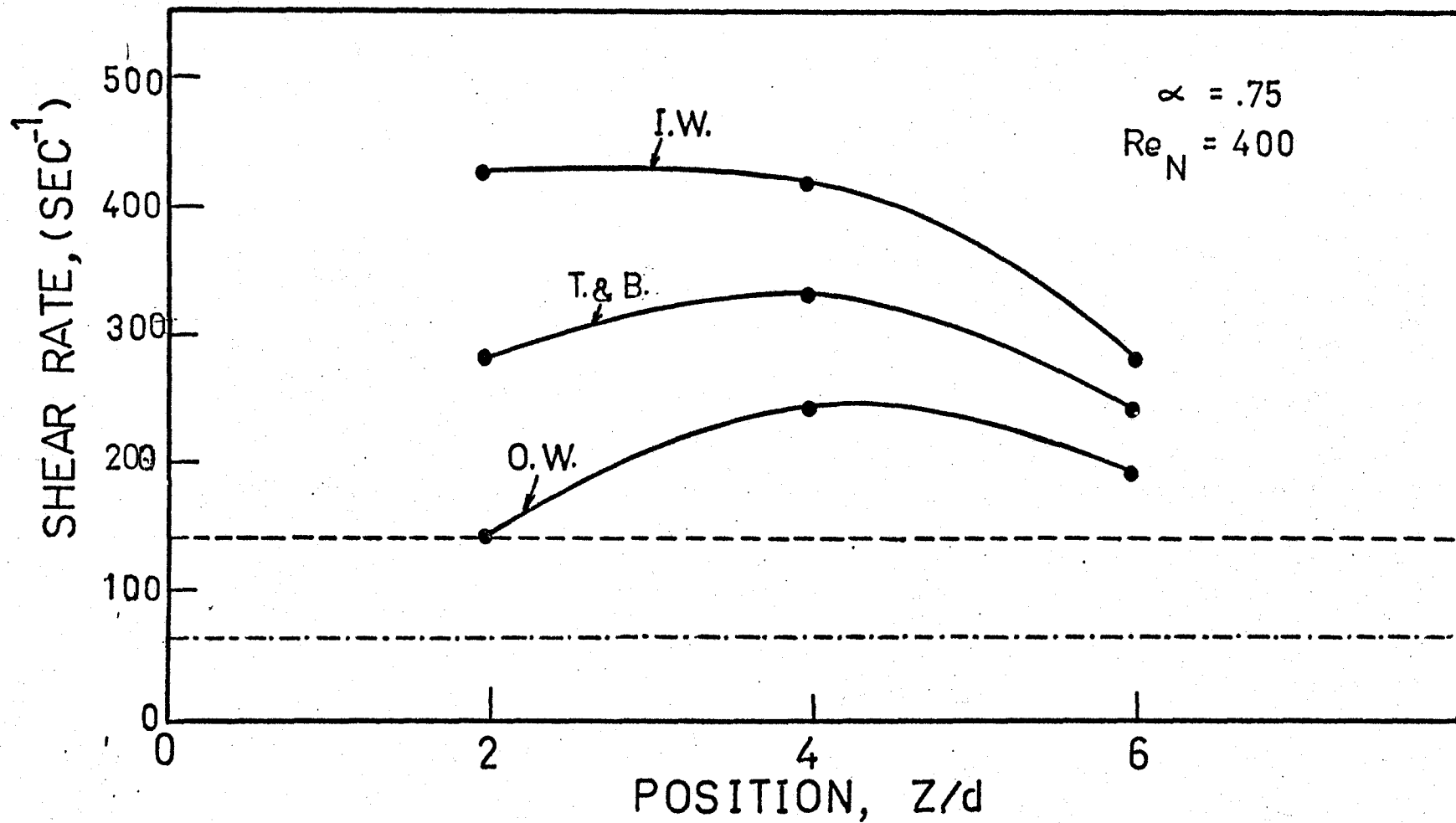


Figure 35. Longitudinal Wall Shear Rate Distributions.  
 (----- Parent Tube and----- Daughter Tube  
 Developed Values)

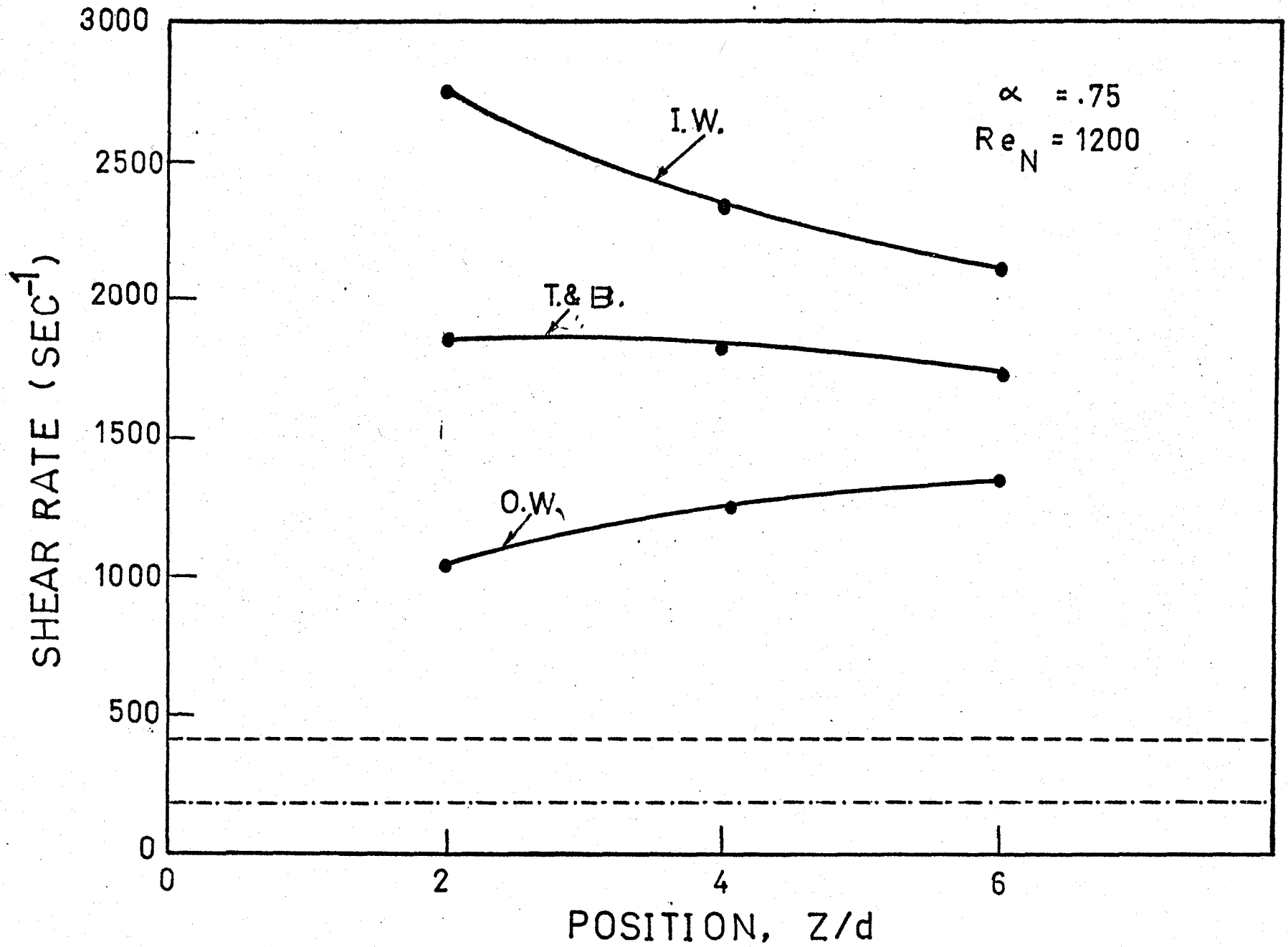


Figure 36. Longitudinal Wall Shear Rate Distributions.  
 (----- Parent Tube and - - - - - Daughter Tube  
 Developed Values)

linear relation as reported by Brech (9).

Extrapolating the shear rate curve on the outside wall for Reynolds number 400 back to  $Z/d = 0$ , indicates the possibility of boundary layer separation. This effect is present at either Reynolds number 800 or 1200. This indicates that the possibility of boundary layer separation is greater in the low Reynolds number flows. This conclusion does not agree with the work of Zamir and Roach (14) who indicate that flow reversal is most likely to occur for high Reynolds number flows. This discrepancy may very well be due to the simplifications used by Zamir and Roach (two dimensional flow, zero bifurcation angle and use of the boundary layer equations).

### 5.3 Biological Discussion

Since the motivation of this work is biomedical, it is pertinent to examine the applicability of the results to the physiological case where blood flows through blood vessels. This can be done after careful review of the assumptions drawn to simplify the problem.

The results represented throughout this study have been obtained for steady flow of a Newtonian fluid using rigid-walled models. Blood in general is a non-Newtonian fluid consisting of particles suspended in fluid plasma. The non-Newtonian behaviour of blood is significant only when the vessel diameter is small. The blood flowing in large

arteries with mean shear rates higher than  $100 \text{ sec}^{-1}$  is likely to be represented by a Newtonian fluid [Whitmore (15)]. The Reynolds number range chosen for this study (400-1200) is applicable to large arteries (0.4-2.1 cm. in diameter) where the mean shear rate is higher than  $100 \text{ sec}^{-1}$  [Whitmore (15)]. This justifies the use of a Newtonian fluid for the fluid mechanical evaluations in this study.

The blood vessels are distensible and the extent of distensibility varies with the origin of the artery and with age [Burton (21)]. The actual change in arterial diameters is quite small [McDonald (22)] and the effect of this change on the velocity field and wall shear rates may be neglected [Caro et al. (6) - Sandler and Bourne (23)]. On the basis of this evidence, it was felt that the vessel distensibility can be neglected.

Another point which seems to be important from the physiological point of view is that the blood flow in the cardiovascular system is pulsatile. It was logical to consider the steady-state problem first with a wide range of Reynolds numbers covering a good portion of the cardiac cycle.

### 5.3.1. Thrombus and Atheroma Formation

Fluid mechanics in general and wall shear rate in particular have been thought to be determining factors in thrombus and atheroma formation [Mustard et al. (24), Fry (25), and Caro et al. (6)]. The mechanism of the formation

of such deposits is not yet understood, however, many widely differing theories implicating fluid mechanical and biochemical effects have been proposed. Some of these theories can be examined in the light of this study.

Mitchell and Schwartz (5) have implicated turbulence as being causative. This work does not present proof of this theory since turbulence was never observed at inlet Reynolds numbers up to 1200. The boundary layer separation theory [Fox and Hugh (4)] may be accepted to a certain extent. In the region studied in this work  $Z/d = 2$  to  $Z/d = 6$  no boundary layer separation was observed, however, there is the possibility of zero shear rate on the wall in the region  $Z/d = 0$  to  $Z/d = 2$ . This possibility is greatest in the cases of the large area ratio branches (Section 5.2.1) and low Reynolds number (Section 5.2.2).

Caro et al. (6) suggested that the development of atheroma is associated with shear rate dependent mass transport and that early atheroma is coincident with those regions in which the arterial wall shear rate is expected to be relatively low. If this is the case, the disease will tend to occur in large area ratio branches where regions of wall shear rate less than the developed values of both parent and daughter tubes were found. Moreover, low Reynolds number flows would further magnify this effect. No biological work has yet been carried out to study the effect of area ratio on the formation of atheroma and this leaves the low shear rate theory

in doubt.

Fry (25) has examined mass transfer under controlled flow conditions evaluating wall shear stress as a function of position from pressure measurements. He concluded that high shear stress at the blood-wall interface is associated with architectural change in the interface, an increased flux of fat particles across the interface and an increased affinity of this surface for blood cellular elements and fibrin. If this is true, the high shear regions then will be likely sites of early atheroma formation. Fry (26) also estimated the yield stress for damage of endothelial cells to be less than  $420 \text{ dynes/cm}^2$ . Recalling the values of wall shear rate obtained in this study, one can note that the maximum shear rate recorded was approximately  $2800 \text{ sec}^{-1}$  (Figure 36) on the inside wall of the branch of area ratio 0.75 and Reynolds number 1200. The shear stress corresponding to this value (assuming blood viscosity of 4 centipoise) is  $112 \text{ dynes/cm}^2$ . This value is well below the yield stress.

## CHAPTER 6

### CONCLUSIONS

A neutrally buoyant tracer particle technique was used to study the flow patterns and wall shear rate distribution in symmetrical bifurcations. It was possible to determine the three velocity components at a number of locations along the branch daughter tube. An analytical representation of the axial velocity as a function of the radial and tangential coordinates was obtained for each location studied via non-linear regression techniques. These analytical functions permit evaluation of velocity profiles and wall shear rates distributions. The following observations and conclusions have been drawn:

1. The axial velocity profiles were found to be symmetric with respect to the plane of bifurcation.
2. In the locations studied, both the tangential and radial velocity components were small compared to the mean axial velocity.
3. In all cases studied, the axial velocity profile at a position two tube diameters downstream from the carina showed a high peak near the branch inside wall and a low axial velocity region near the outside wall. As the flow moved downstream the peak was convected tangentially evening out the

profile towards an axially symmetric profile at about 6 tube diameters downstream.

4. The development of downstream flow was dependent on the input Reynolds number; smaller Reynolds number leads to more rapid flow development.
5. Wall shear rate at constant axial position can be represented by a displaced cosine function. High shear rates always occur on the inside wall of the daughter tube and low shear rates on the outside wall. Significant differentials in shear rate only occur near the carina.
6. With respect to thrombus and atheroma formation; if high shear rates are disposed to thrombus and atheroma formation then the disease will tend to occur in small area ratio branches where the largest positive deviation from developed wall shear rate values are found. If low shear rates are disposed to thrombus and atheroma formation then the disease will occur in large area ratio branches where the lowest shear rate values are found.
7. Possible presence of wall shear rates close to zero is expected along with the possibility of flow reversal in large area ratio bifurcations. Low Reynolds number flows would further magnify this effect.
8. In the locations studied the highest shear stress was found to be well below the yield stress for damage of endothelial cells.

## REFERENCES

1. Knox, W. R., "An Experimental Investigation of the Steady Flow of a Viscous Fluid in Circular, Branched Tubes", MS Thesis, University of Minnesota (1962).
2. Schroter, R. C. and Sudlow, M. F., "Flow Patterns in Models of the Human Bronchial Airways", *Respiration Physiology*, Vol. 7, pp. 341-355 (1969).
3. Pedley, T. J., Schroter, R. C. and Sudlow, M. F., "Flow and Pressure Drop in Systems of Repeatedly Branching Tubes", *J. Fluid Mechanics*, Vol. 46, pp. 365 (1971).
4. Fox, J. A. and Hugh, A. E., "Localization of Atheroma: A Theory based on Boundary Layer Separation", *British Heart J.*, Vol. 28, pp. 288 (1966).
5. Mitchell, J. R. A. and Schwartz, C. J., "Arterial Diseases", Blackwell Scientific Publications, Oxford (1965).
6. Caro C. G., Fitz-Gerald, J. M. and Schroter, R. C., "Atheroma and Arterial Wall Shear", *Proc. Roy. Soc., Ser. B.*, Vol. 177, pp. 109 (1971).
7. French, J. E., "Atherosclerosis", In *General Pathology*, Ed. H. Florey, London (1970).
8. Texon, M., "The Hemodynamic Concept of Atherosclerosis", *Bulletin of the New York Academy of Medicine*, Vol. 36, pp. 263 (1960).
9. Brech, R., "Aspects of Steady and Pulsatile Flow in Branched Tubes with Particular Reference to Blood Flow", Report No. 1020/71, University of Oxford, Oxford, England (1971).
10. Lew, H. S., "Low Reynolds Number Equi-bifurcation Flow in Two-dimensional Channel", *J. Biomechanics*, Vol. 4, pp. 559 (1971).
11. Lew, H. S., "The Use of Entry Flow Equations in Studying the Uniform Entry Flow", *J. Biomechanics*, Vol. 6, pp. 205 (1973).
12. Lew, H. S., "The Dividing Streamline of Bifurcation Flows in a Two-dimensional Channel at Low Reynolds Number", *J. Biomechanics*, Vol. 6, pp. 423 (1973).
13. Lynn, N. S., Fox, V. G. and Ross, L. W., "Computation of Fluid-dynamic Contributions to Atherosclerosis at Arterial Bifurcations", *Biorheology*, Vol. 9, pp. 61 (1972).

14. Zamir, M. and Roach, M. R., "Blood Flow of a Two-dimensional Bifurcation", J. Theor. Biol., Vol. 42, pp. 33 (1973).
15. Whitmore, R. L., "Rheology of the Circulation", Pergamon Press (1968).
16. Goldsmith, H. L., "Microscopic Flow Properties of Red Cells", Federation Proc., Vol. 26, pp. 1813 (1967).
17. Knowles, S. R., Woods, D. R. and Feuerstein, I. A., "The Velocity Distribution within a Hydrocyclone Operating without an Air Core", Can. J. C. E., Vol. 51, pp. 263 (1973).
18. Pike, G. K., "Laminar Flow Development Downstream of an Abrupt Circular Channel Expansion", M.Eng. Thesis, McMaster University, Hamilton, Canada (1973).
19. Feuerstein, I. A. and Woods, D. R., "A Photographic Technique for Measuring Fluid Velocities with Tracer Particles", J. SMPTE, Vol. 82, 916 (1973).
20. Siddall, J. N., "Analytical Decision-Making in Engineering Design", Prentice-Hall, Inc., New Jersey, 1972.
21. Burton, A. C., "Physical Principles of Circulatory Phenomena, Handbook of Physiology", Sect. 2, Circulation, Am. Physiol. Soc., Washington (1962).
22. McDonald, D. A., "Blood Flow in Arteries", Edward Arnold Ltd., London (1960).
23. Sandler, M. and Bourne, G. H., "Atherosclerosis and Its Origin", Academic Press, New York (1963).
24. Mustard, J. F., Murphy, E. A., Rowsell, H. C. and Downie, H. G., "Factors Influencing Thrombus Formation", The American Journal of Medicine, Vol. 33, pp. 621 (1962).
25. Fry, L. D., "Certain Histological and Chemical Responses of the Vascular Interface to Acutely Induced Mechanical Stress in the Aorta of the Dog", Circulation Research, Vol. 24, pp. 93 (1969).
26. Fry, L. D., "Acute Vascular Endothelial Changes Associated with Increased Blood Velocity Gradients", Circulation Research, Vol. 22, pp. 165 (1968).

## APPENDIX 1

### PARENT TUBE VELOCITY PROFILE

In order to check the flow velocity profile upon entering the bifurcation region, a section of the parent tube was filmed at the three flow rate settings used in this study (44.4, 85 and 127 cm<sup>3</sup>/sec.). The velocity profiles obtained were used to check the flowmeter readings.

The section of the parent tube under investigation was 20 centimeters upstream of the carina. The moving particles in this section and its image in a mirror positioned parallel to the tube (see "Viewing Cell" - Section 3.2.1) were recorded in a cine film. Point axial fluid velocity was obtained for each particle by analyzing the film frame by frame. (Experimental procedure and film analysis may be found in Chapter 3).

The axial velocity profile in the parent tube was fit to the functional form

$$V_z = A [1 - (\eta)^B] \quad (A1)$$

where A and B are parameters of the function and  $\eta$  is the non-dimensional radial coordinate. A non-linear least squares fitting program was used to obtain values of these parameters. This yielded the values shown below for A, B, and the volumetric flowrate as computed from an integration of Equation (A1).

$Q_D$	A	B	$2\pi R^2 \int_{\eta=0}^1 v_z \eta \, d\eta$
44.5	33.32	2.01	45.72
85.0	68.81	1.98	86.90
122.0	92.01	2.00	125.95

It may then be concluded that the flow is essentially parabolic since the values of B are within 1% of 2.00. The volumetric flow as obtained from these velocity profiles is within 3% of the values obtained from the flowmeter, providing a check on the accuracy of the flowmeters. Figure 37 shows the velocity profiles obtained for the three different flow rates.

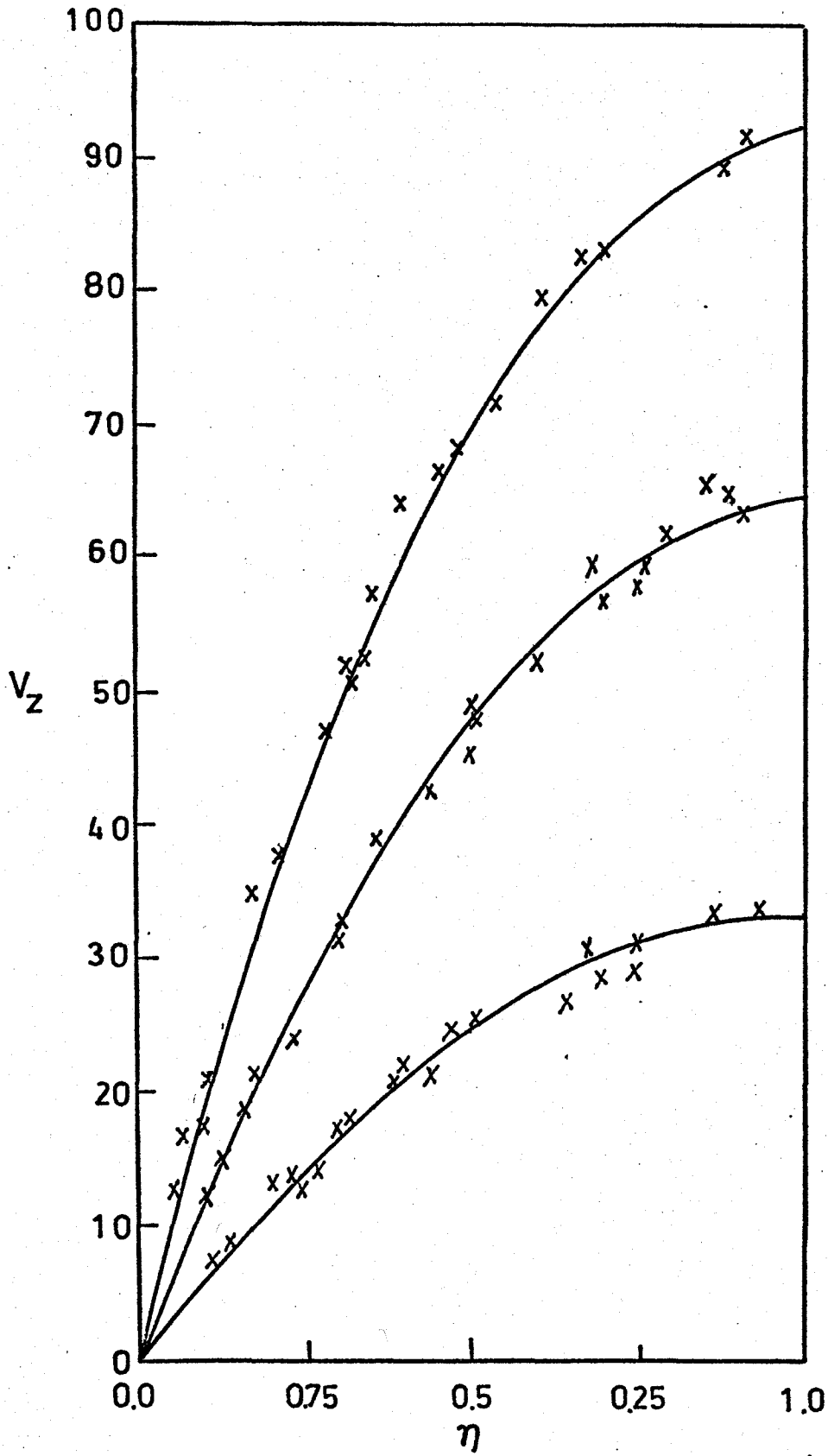


Figure 37 Parent Tube Velocity Profile.

APPENDIX 2  
ERROR ANALYSIS

The quantities subjected to error analysis are:

- (1) Tube Diameters
- (2) Flowrate
- (3) Refractive Index
- (4) Fluid Viscosity
- (5) Particle Velocities

Tube Diameters

Internal diameters were measured at the end of each tube with the aid of a vernier caliper (accuracy  $\pm 0.0005$  cm.). The mean of the two diameters was taken as the diameter,  $d$ , (Table 1) and the out-of-roundness expressed as (largest diameter-smallest diameter)/mean. The largest value of this parameter was 0.4%.

Flowrate

Maximum error in reading the manometer head =  $\pm 1.25\%$   
Accuracy of Venturimeter calibration curve =  $\pm 3\%$   
Total error in measuring parent tube flowrate =  $\pm 4.25\%$

Refractive Index

Refractive index of both the suspending fluid and the glesrol solution was measured using an Abbe refractometer with maximum error, .005%.

Fluid Viscosity

Maximum error incurred in making a viscosity measurement at  $T^{\circ}C = 1\%$  of full scale reading =  $\pm 0.1$  cp  
 Lowest viscosity value recorded = 4.8 cp  
 Therefore instrument error =  $\pm 2\%$

Particle Velocity

Axial velocity component was obtained as the axial distance travelled by the particle in time  $\Delta T$ .

The distance between particle centres was measured to within 0.5mm. The Smallest distance measured = 20 mm.

Error in measuring a distance directly from the screen =  $\pm 2.5\%$ .

The magnification factor was obtained to within 2%.

Therefore the maximum error in obtaining the distance travelled by a particle in time  $\Delta T = \pm 4.5\%$ . The error in  $\Delta T$  depends upon the error in filming speed. Frame rate was obtained to within  $\pm 3\%$ .

APPENDIX 3  
TABULATED EXPERIMENTAL DATA TABLES

$\eta$	$\theta$	$V_z^+$	$V_\theta^+$	$V_r^+$
.15	1.89	1.21	-.01	-.00
.17	5.50	1.31	.02	.03
.22	.94	1.43	-.01	.02
.23	4.72	1.21	.00	.00
.23	.42	1.43	.00	.03
.24	5.57	1.34	.02	.02
.27	1.75	1.36	-.02	.01
.30	.01	1.54	-.00	.02
.31	3.38	1.02	.00	-.04
.32	4.33	1.19	.03	-.01
.32	3.52	1.00	.01	-.03
.33	4.72	1.24	-.01	.01
.35	3.48	.99	.01	-.03
.39	6.13	1.53	.00	.02
.43	.69	1.54	.00	.02
.45	4.72	1.38	-.00	.01
.46	5.42	1.54	.01	.01
.46	4.23	1.24	-.01	-.02
.53	3.61	.95	-.01	-.03
.53	1.11	1.62	0.00	0.00
.55	.97	1.62	-.00	.02
.56	4.88	1.51	-.02	.01
.57	5.94	1.78	-.01	.02
.58	1.37	1.60	.02	.02
.60	2.21	1.30	.01	-.00
.61	5.50	1.66	.00	.01
.61	4.22	1.42	-.03	-.02
.61	5.39	1.70	0.00	0.00
.62	1.69	1.49	.02	.01
.63	1.42	1.70	.04	.01
.64	4.23	1.34	-.04	-.01
.65	4.72	1.54	.01	.00
.65	4.24	1.22	-.04	-.02
.68	2.59	.70	.01	-.02
.69	2.38	1.13	.03	-.02
.72	3.44	.72	-.01	-.00
.73	5.43	1.78	-.02	.00
.73	.42	1.71	.02	.00
.75	2.49	.93	.02	-.01
.78	5.55	1.70	-.02	-.00
.78	1.74	1.29	.04	.01
.80	3.75	.70	-.02	-.01
.82	2.02	.98	.03	-.00
.85	3.57	.37	-.01	-.01
.86	.89	1.03	.03	-.00
.86	1.05	.71	.02	.00
.90	1.41	.53	.02	-.00

.91	4.74	.66	-.02	-.00
.91	2.74	.42	.01	-.00
.94	1.70	.42	.01	.00
.95	5.06	.61	-.02	.00

Table 11 Velocity Data for Experiment (I-L-1).

$n$	$\theta$	$V_z^+$	$V_\theta^+$	$V_r^+$
.04	3.08	1.06	.01	.09
.08	.03	1.25	-.02	.03
.13	2.36	1.27	-.01	-.02
.15	5.61	1.31	.01	.02
.25	4.96	1.27	.03	.01
.26	5.30	1.27	.02	.02
.26	3.13	1.10	-.00	-.03
.30	5.78	1.37	.01	.02
.32	1.56	1.50	0.00	0.00
.37	.92	1.59	.01	-.00
.39	3.55	1.07	.00	-.02
.39	1.23	1.62	.01	.01
.46	4.84	1.44	.01	.01
.47	2.19	1.49	.02	-.01
.47	.82	1.62	-.00	.01
.48	1.70	1.55	0.00	0.00
.49	.51	1.70	.01	.00
.56	2.03	1.51	.02	-.01
.57	6.03	1.63	0.00	0.00
.57	3.99	1.29	-.01	-.01
.58	4.59	1.44	-.01	.00
.61	6.15	1.70	-.00	.01
.61	2.83	1.07	-.12	-.11
.62	2.26	1.24	.02	-.01
.62	5.11	1.63	-.00	.01
.62	5.11	1.51	0.00	0.00
.64	2.30	1.14	.03	-.02
.64	2.16	1.33	.02	-.01
.65	4.94	1.58	-.02	.00
.65	.60	1.60	.00	-.02
.65	.58	1.53	.01	.01
.66	4.68	1.63	-.01	.00
.66	3.18	.79	.01	-.00
.66	.22	1.67	.02	-.00
.67	.00	1.43	-.00	.01
.67	3.93	1.01	-.02	-.02
.67	2.13	1.18	.02	-.00
.68	3.91	1.14	-.00	-.01
.69	.24	1.53	0.00	0.00
.69	4.38	1.47	-.02	.00
.71	.52	1.33	.01	-.01
.72	3.06	.77	.01	-.00
.74	5.62	1.62	-.01	.02
.74	4.45	1.51	-.03	.01
.76	2.89	.59	.01	-.00
.76	.67	1.05	0.00	0.00
.77	2.37	.85	.01	-.00

.80	5.10	1.46	-.02	.01
.82	4.36	1.18	-.02	-.01
.86	5.65	1.35	-.01	-.01
.86	5.17	1.32	-.02	.00
.92	4.75	1.13	-.01	.01
.99	5.45	.64	-.00	.00
.99	5.08	.66	-.00	-.00

Table 12      Velocity Data for Experiment (I-L-2).

$n$	$\theta$	$V_z^+$	$V_\theta^+$	$V_r^+$
.17	4.25	1.37	.03	-.01
.19	.69	1.41	-.01	.02
.29	2.85	1.15	-.01	-.02
.25	.14	1.44	-.00	.02
.27	1.56	1.55	.00	.01
.27	1.56	1.57	0.00	0.00
.29	5.22	1.44	.01	.02
.37	4.72	1.48	.01	.00
.39	3.61	1.25	.00	-.03
.36	2.23	1.42	-.01	-.01
.32	4.32	1.42	.02	-.01
.42	3.00	1.17	-.00	-.02
.44	4.91	1.50	.00	.00
.40	5.62	1.51	.02	.01
.50	3.24	1.06	.00	-.02
.45	4.82	1.51	.00	-.01
.43	1.75	1.44	-.03	.00
.45	1.41	1.57	.00	.01
.45	1.38	1.50	-.00	.01
.46	4.85	1.51	-.00	.00
.44	.44	1.59	.01	.03
.52	.12	1.60	.01	.02
.58	1.68	1.49	.02	-.00
.56	2.45	1.48	-.00	-.01
.56	4.21	1.44	.00	-.02
.63	5.25	1.52	-.00	.00
.64	1.86	1.36	-.00	.01
.62	1.65	1.47	.01	.01
.68	.29	1.42	.02	.01
.63	4.14	1.33	-.01	-.02
.70	3.79	.99	-.01	-.00
.64	1.47	1.36	.01	.01
.66	2.29	1.39	0.00	0.00
.68	4.26	1.24	-.01	.00
.61	5.24	1.54	-.00	.01
.64	3.40	.89	-.00	-.00
.70	1.80	1.14	.01	.00
.71	5.76	1.37	0.00	0.00
.74	5.46	1.05	-.01	.01
.74	3.04	.72	0.00	0.00
.74	.00	1.37	0.00	0.00
.70	.42	1.22	.00	.00
.77	.67	1.37	.01	.01
.71	.51	1.44	.02	.01
.71	.90	1.25	.01	.00
.80	.63	.99	.01	.01
.73	3.56	.87	-.00	-.01

.85	.45	.70	.00	.00
.84	5.50	1.03	-.00	.00
.88	5.40	.77	-.00	.00
.85	2.85	.52	-.00	-.00
.83	.53	.87	.01	-.00
.80	4.81	.47	0.00	0.00
.80	1.80	.46	.00	.00
.93	.50	.47	.01	.01
.91	5.89	.65	0.00	0.00
.91	5.22	.52	-.00	-.00
.92	5.87	.57	0.00	0.00

Table 13 Velocity Data for Experiment (I-L-3).

$n$	$\theta$	$V_z^+$	$V_\theta^+$	$V_r^+$
,05	3,00	1,07	=,00	=,02
,05	1,52	1,96	=,01	=,02
,11	4,73	1,04	=,00	=,02
,15	,46	2,36	=,03	=,15
,17	1,85	1,13	=,02	=,00
,23	,79	2,28	,04	=,03
,28	5,86	1,31	,03	,02
,28	4,10	1,06	,03	=,02
,29	5,21	1,27	,02	,02
,34	3,97	,92	,03	=,03
,39	5,07	1,32	,02	,02
,40	,23	1,72	,01	,02
,41	5,54	1,57	,00	,03
,42	1,06	1,41	=,02	,02
,47	1,00	1,63	,01	,02
,54	2,66	1,33	,03	=,02
,54	3,62	1,33	=,03	=,01
,55	,00	1,76	=,01	,01
,58	4,30	1,31	=,02	,01
,59	6,09	1,81	,01	,02
,60	3,06	,78	,01	=,03
,60	,81	2,82	=,00	=,01
,62	6,02	1,97	,01	,01
,62	3,14	,68	,00	=,03
,63	,94	1,78	,02	,02
,64	2,43	1,88	0,00	0,00
,64	,25	1,95	=,00	,01
,64	2,53	1,34	,05	=,01
,68	,31	2,02	,04	,00
,68	1,26	1,77	,05	,01
,69	5,44	1,91	=,02	,02
,72	1,86	1,46	,07	,01
,75	2,31	1,45	,08	,00
,77	3,44	,61	=,01	=,02
,79	,15	1,97	,03	,02
,81	1,13	1,32	,05	,01
,82	5,82	2,01	=,00	,01
,84	4,43	1,58	=,06	=,01
,86	4,55	1,55	=,03	=,00
,93	,52	,78	,02	=,00
,93	5,93	,92	=,00	,01
,93	6,11	1,38	=,02	,00

Table 14 Velocity Data for Experiment (I-M-1),

$\eta$	$\theta$	$V_z^+$	$V_\theta^+$	$V_r^+$
.00	.79	1.04	-.00	.01
.04	1.52	1.10	-.00	-.07
.05	1.11	1.77	-.01	-.10
.06	3.93	1.16	-.01	-.03
.09	3.93	1.19	-.01	-.02
.09	3.93	.94	-.01	-.05
.14	.46	1.31	-.01	-.08
.15	3.93	1.71	-.03	-.06
.15	.79	1.71	-.03	-.10
.15	3.93	1.10	.02	-.05
.15	.98	1.15	-.03	.01
.18	.95	1.03	-.02	-.02
.18	.95	1.40	-.03	-.03
.20	3.85	1.07	-.01	-.05
.21	3.93	1.71	-.04	-.08
.24	.79	1.69	-.04	-.06
.26	.61	.92	-.02	-.05
.30	.79	.68	-.02	-.04
.30	3.83	1.29	.00	-.02
.30	3.83	1.29	.00	-.02
.33	3.93	.96	.00	.02
.26	.79	1.84	-.04	-.08
.37	4.03	1.15	-.02	.00
.38	3.97	1.69	-.05	-.05
.38	.83	1.77	-.05	-.09
.38	3.97	.56	-.02	-.03
.41	3.96	1.20	.09	.03
.42	.79	1.52	-.05	-.08
.44	3.82	1.24	.00	.00
.46	3.86	1.22	.02	.00
.49	.72	1.42	-.02	-.01
.50	.82	1.56	-.01	-.01
.50	.88	1.13	.04	.01
.50	4.02	1.01	.01	.02
.53	.87	1.91	.06	.02
.56	4.01	1.24	.06	.05
.58	3.93	1.71	-.04	-.04
.59	3.85	.95	-.02	-.02
.62	.70	1.43	-.01	.02
.62	.81	1.23	.11	.11
.64	.83	1.69	-.03	-.02
.65	3.95	1.54	-.05	-.05
.68	3.90	.67	-.01	-.01
.70	3.93	.86	-.02	-.03
.73	.83	2.27	-.03	-.04
.82	.75	.50	-.01	-.00
.82	3.85	1.34	.03	.06

.83	3.95	.58	-.01	-.01
.82	.73	1.32	.02	.07
.80	.80	1.77	.15	.07
.02	.80	1.36	.04	.02
.04	3.80	.90	.01	.04
.07	3.93	1.59	.14	.07
.97	3.93	1.40	.31	.14

Table 15 Velocity Data for Experiment (I-M-2).

$\eta$	$\theta$	$V_z^+$	$V_\theta^+$	$V_r^+$
.00	.79	.99	-.00	.01
.04	1.52	1.05	-.00	-.07
.05	1.11	1.68	-.01	-.09
.09	3.93	.89	-.01	-.05
.14	.46	1.25	-.01	-.07
.15	.79	1.62	-.03	-.09
.15	3.93	1.04	.02	-.05
.15	.98	1.10	-.03	.01
.18	.95	.98	-.02	-.02
.18	.95	1.42	-.03	-.03
.19	3.85	1.02	-.01	-.05
.24	.79	1.60	-.03	-.05
.26	.61	.87	-.02	-.04
.30	3.83	1.23	.00	-.02
.30	3.83	1.23	.00	-.02
.30	.79	.65	-.02	-.04
.33	3.93	.91	.00	.02
.35	.79	1.75	-.04	-.07
.36	4.03	1.10	-.02	.00
.37	.83	1.68	-.05	-.08
.37	3.97	.54	-.02	-.03
.40	3.96	1.14	.09	.03
.41	.79	1.45	-.05	-.07
.43	3.82	1.18	.00	.00
.44	3.86	1.16	.01	.00
.47	.72	1.35	-.02	-.01
.49	.82	1.48	-.01	-.01
.49	.88	1.07	.04	.01
.49	4.02	.96	.00	.02
.52	.87	1.81	.06	.02
.55	4.01	1.18	.06	.04
.58	3.85	.91	-.02	-.01
.60	.70	1.36	-.01	.01
.61	.81	1.17	.10	.10
.62	.83	1.60	-.02	-.02
.64	3.95	1.46	-.04	-.04
.67	3.90	.64	-.01	-.01
.68	3.93	.82	-.02	-.03
.71	.83	2.16	-.03	-.04
.80	.75	.47	-.01	-.00
.80	3.85	1.27	.02	.06
.81	.73	1.25	.02	.06
.87	.80	1.68	.14	.06
.90	.80	1.30	.04	.02
.92	3.89	.94	.01	.04
.95	3.93	1.52	.13	.07
.95	3.93	1.42	.29	.13
.98	3.90	1.02	.02	.05
.99	.80	.84	.02	.01

Table 16 Velocity Data for Experiment (I-M-3).

$\eta$	$\theta$	$V_z^+$	$V_\theta^+$	$V_r^+$
.18	1.89	1.00	-.02	-.02
.26	3.13	1.10	-.00	-.06
.27	2.71	1.23	-.02	-.05
.34	6.17	1.31	.00	-.00
.36	.16	1.34	-.00	.01
.36	1.20	1.09	.02	-.00
.37	2.15	1.03	.01	-.01
.38	4.03	1.00	-.01	-.02
.41	.42	1.06	-.00	.02
.44	2.89	1.19	.00	-.03
.46	5.21	1.21	-.03	.00
.47	2.82	1.23	.01	-.02
.48	5.47	1.60	-.02	.01
.49	2.44	1.32	.02	-.02
.52	4.35	1.36	-.02	.01
.52	4.50	1.32	-.02	-.00
.52	.24	1.93	0.00	0.00
.56	4.07	1.34	-.02	-.01
.56	.60	1.56	.01	.01
.57	4.72	1.49	.00	-.01
.57	1.93	1.41	.02	-.01
.57	1.31	1.72	.02	-.01
.58	.39	1.91	.00	.02
.58	.16	1.94	.01	.01
.58	4.52	1.61	-.03	-.00
.60	.59	1.73	.02	.01
.62	1.39	1.66	.02	-.00
.64	3.76	1.09	-.01	-.01
.64	5.48	1.51	-.02	.01
.65	6.17	1.82	.00	.01
.67	1.91	1.43	.02	-.00
.69	.90	1.62	.03	-.00
.69	.54	1.94	-.00	.00
.70	.50	.74	0.00	0.00
.70	1.38	1.66	.03	.00
.71	1.33	1.51	.02	-.01
.72	4.71	1.51	.00	-.01
.74	2.81	.76	-.01	-.00
.76	6.28	1.76	0.00	0.00
.77	1.01	1.17	.02	-.01
.77	.17	1.64	0.00	0.00
.79	2.39	.84	.02	-.00
.80	6.28	1.15	-.00	-.00
.80	1.03	0.00	.08	.18
.80	5.90	1.45	.00	.00
.82	1.06	.94	.01	-.00
.82	.64	.66	.00	.00

.87	.21	1.56	.02	.00
.87	4.66	1.82	-.01	.01
.04	.40	.46	.00	.00
.95	.75	.47	.01	-.00

Table 17 Velocity Data for Experiment (I-H-1).

$\eta$	$\theta$	$V_z^+$	$V_\theta^+$	$V_r^+$
.20	1.89	1.13	-.02	-.02
.20	2.12	1.34	-.00	-.07
.21	2.71	1.38	-.02	-.07
.22	6.05	1.55	-.02	.06
.26	4.27	1.21	-.02	.01
.42	1.20	1.22	.03	-.00
.42	4.11	1.11	-.00	-.02
.44	2.15	1.15	.01	-.01
.45	4.03	1.12	-.01	-.02
.47	.42	1.19	-.00	.03
.51	2.89	1.34	.00	-.04
.54	5.21	1.36	-.03	.01
.55	2.82	1.38	.02	-.03
.57	5.47	1.80	-.03	.01
.57	2.44	1.48	.02	-.02
.60	4.35	1.53	-.02	.01
.62	4.50	1.48	-.02	-.01
.63	6.15	1.83	-.01	.02
.65	4.07	1.50	-.03	-.02
.65	.60	1.75	.01	.01
.67	4.72	1.67	.00	-.01
.67	1.93	1.58	.02	-.01
.67	1.31	1.94	.03	-.01
.68	4.52	1.81	-.04	-.01
.69	5.06	1.92	-.03	-.01
.70	.59	1.94	.02	.01
.72	1.39	1.87	.03	-.01
.74	2.76	1.22	-.02	-.01
.75	.81	1.70	.02	.01
.76	2.22	1.10	.01	-.00
.76	4.97	1.92	-.02	.00
.76	.11	2.04	-.00	.01
.78	1.91	1.60	.03	-.01
.80	.90	1.82	.04	-.00
.81	.50	.84	0.00	0.00
.81	1.38	1.87	.04	.01
.82	1.33	1.70	.03	-.01
.84	1.57	1.70	-.00	-.01
.87	2.81	.85	-.01	-.00
.89	6.28	1.98	0.00	0.00
.89	3.21	.89	.00	.00
.89	1.01	1.31	.03	-.01
.90	4.98	1.15	-.02	-.01
.90	.17	1.84	0.00	0.00
.92	2.39	.94	.03	-.00
.93	6.28	1.29	-.00	-.00
.93	1.03	0.00	.10	.23
.93	.38	1.62	-.00	.00
.97	1.06	1.06	.02	-.00

Table 18 Velocity Data for Experiment (I-H-2).

$n$	$\theta$	$V_z^+$	$V_\theta^+$	$V_r^+$
.12	.39	.75	-.00	.01
.19	.00	.81	-.00	.01
.23	5.47	.76	.01	.01
.25	5.50	.87	.01	.01
.32	.41	1.23	.00	.01
.35	1.36	.93	.00	.01
.41	6.17	1.38	-.00	.02
.46	.70	1.46	-.00	.00
.46	.08	1.55	-.00	.01
.46	5.51	1.22	.00	.01
.46	4.03	.74	.01	-.00
.48	4.52	.70	.00	.01
.52	5.37	1.38	.00	.01
.54	3.96	.81	-.01	.00
.54	.70	1.60	.01	.01
.56	1.02	1.46	.01	-.01
.56	1.15	1.48	.01	.01
.57	3.43	.56	.00	-.05
.59	3.14	.60	-.01	-.04
.59	5.29	1.42	-.01	.01
.59	1.73	1.23	.02	.01
.64	5.12	1.44	-.02	.01
.65	2.14	.95	.02	.01
.66	1.16	1.68	.03	.00
.68	2.43	.91	.04	.00
.69	4.42	1.10	-.03	.01
.71	1.21	1.68	.03	.01
.73	5.92	1.90	.00	.01
.73	5.43	1.71	-.01	.00
.73	.41	1.92	.02	-.00
.73	1.56	1.45	.01	.01
.73	.02	1.95	.02	.02
.75	.21	1.97	.02	.00
.75	.67	1.87	.01	.00
.76	5.87	1.92	-.00	.01
.77	5.99	1.98	-.01	.01
.77	.55	1.60	.02	.01
.77	1.02	1.79	.04	-.00
.79	2.11	1.25	.05	.01
.79	4.78	1.50	-.03	-.01
.80	4.50	1.26	-.04	-.01
.81	5.13	1.67	-.02	.01
.82	.56	1.21	-.02	-.03
.83	.79	1.21	.02	-.01
.86	4.09	1.04	-.06	-.01
.86	4.17	1.08	-.05	-.00
.86	.79	.70	.01	-.00

.86	4.88	1.35	-.05	.00
.86	6.28	1.40	.01	-.00
.87	4.45	1.14	-.04	-.01
.88	5.34	1.52	-.02	-.00
.90	.02	1.31	.00	-.00
.90	4.65	.97	-.03	-.00
.91	5.27	1.36	-.03	.00
.91	5.34	1.33	-.03	.01
.91	.71	.61	.01	-.00
.92	2.21	.78	.04	.01
.92	6.20	1.08	.00	-.00
.93	4.89	.61	.03	-.00
.93	6.05	.97	.00	.00
.94	5.41	1.21	-.02	-.00
.94	5.56	.95	-.02	.01
.95	2.36	.61	.03	.01
.96	3.71	.41	-.02	-.00
.97	5.00	.58	-.02	.00

Table 19 Velocity Data for Experiment (II-M-1).

n	$\theta$	$V_z^+$	$V_\theta^+$	$V_r^+$
.14	2.86	1.00	-.02	-.03
.17	.46	.97	-.01	.04
.17	5.70	.90	.02	.02
.26	.22	1.06	-.00	.03
.29	6.12	.97	.01	.03
.30	4.72	.89	.00	-.01
.31	4.99	.95	-.00	.00
.32	3.76	1.04	.03	-.01
.32	.62	.98	.00	.03
.33	5.48	.96	.00	.02
.33	6.14	.98	-.01	.02
.36	2.71	1.04	-.01	-.03
.37	5.43	1.02	-.00	-.02
.38	3.79	1.10	.00	-.03
.39	4.47	.99	-.01	.00
.42	1.91	.97	.01	.00
.46	4.00	1.12	-.01	-.01
.47	4.01	1.10	-.01	-.02
.47	4.07	1.15	-.01	-.01
.48	4.27	1.15	-.01	-.01
.49	2.76	1.10	.00	-.02
.49	.52	1.29	.01	.01
.50	3.99	1.17	-.02	-.02
.52	1.57	1.17	-.01	.00
.52	1.37	1.26	.01	.02
.55	1.89	1.15	.02	.00
.57	.00	1.61	-.00	.02
.57	3.74	1.17	-.02	-.02
.57	1.87	1.24	.02	.00
.58	5.61	1.53	-.01	.01
.59	4.97	1.46	-.02	-.01
.59	5.78	1.61	-.00	.01
.62	5.19	1.61	-.01	-.00
.63	3.95	1.22	-.02	-.01
.65	4.57	1.44	-.02	-.01
.66	6.21	1.82	.02	.01
.68	.13	1.85	.02	.01
.69	.61	1.83	.02	.01
.73	1.07	1.71	.02	.00
.73	4.20	1.24	-.02	-.01
.74	.05	1.85	0.00	0.00
.74	4.52	1.38	-.02	-.01
.77	1.17	1.37	.02	.01
.77	.63	1.71	.01	.01
.77	5.74	1.68	-.00	.01
.78	5.86	1.87	.00	.01
.79	1.94	1.40	.03	.00

.79	.07	1.64	.01	.01
.81	.23	1.54	.01	.00
.82	4.17	.89	-.02	-.00
.82	.96	1.44	.01	.00
.84	3.53	.69	-.00	-.00
.85	3.37	.56	.00	-.01
.88	2.88	.62	.00	-.00
.88	.85	.87	.01	-.00
.88	.98	.80	.02	-.01
.89	.11	.82	0.00	0.00
.90	5.89	1.56	-.01	.00
.93	1.33	.62	.01	-.00
.95	5.30	.62	-.00	-.00
.96	5.79	.65	-.01	.00

Table 20 Velocity Data for Experiment (II-M-2).

$\eta$	$\theta$	$V_z^+$	$V_\theta^+$	$V_r^+$
.08	.79	1.21	-.02	.03
.15	4.72	1.31	.00	-.01
.15	3.39	1.25	-.00	-.03
.16	5.20	1.26	.03	.00
.17	4.37	1.34	.00	-.00
.20	.42	1.23	-.01	.04
.27	.35	1.32	-.00	.03
.29	4.09	1.42	-.01	-.02
.34	2.45	1.34	-.00	-.02
.34	1.10	1.23	-.01	.02
.34	5.35	1.26	0.00	0.00
.36	6.03	1.19	.01	.03
.37	.01	1.23	-.00	.03
.40	3.88	1.37	-.01	-.02
.42	4.84	1.48	-.00	-.01
.45	.90	1.19	.01	.02
.46	3.87	1.37	-.00	-.01
.47	3.04	1.13	0.00	0.00
.47	5.65	1.34	0.00	0.00
.48	4.97	1.53	-.02	-.00
.49	2.42	1.41	.01	-.01
.50	5.60	1.31	-.01	.00
.56	1.20	1.34	.02	.00
.57	3.73	1.16	-.00	-.01
.59	1.28	1.42	.02	-.00
.59	1.52	1.53	.02	-.00
.61	.58	1.37	.01	.01
.61	3.37	.97	.00	-.00
.61	5.14	1.64	-.01	-.01
.61	6.21	1.44	-.01	.01
.65	5.74	1.80	-.02	.01
.65	4.74	1.54	-.01	-.01
.65	3.98	1.14	-.01	-.01
.66	3.14	1.03	-.00	-.00
.67	4.22	1.26	-.00	-.00
.67	.60	1.56	.02	.01
.68	2.39	1.34	.02	-.01
.69	.00	1.64	-.00	.01
.70	2.28	1.38	.02	-.01
.71	1.77	1.50	.03	-.01
.73	3.27	.82	.00	-.00
.74	.39	1.64	.01	.01
.75	2.62	1.08	.01	-.00
.78	.44	1.89	0.00	0.00
.78	6.24	1.60	0.00	0.00
.79	2.06	1.24	.02	-.00
.80	3.29	.69	.00	.00

.81	5.95	1.45	-.01	.00
.85	1.70	1.05	.01	-.00
.87	.94	.99	.01	.00
.89	2.00	.77	.01	.00
.89	1.86	.74	.01	-.00
.89	2.07	.67	.01	-.00
.92	5.43	.63	-.01	.00
.92	1.09	.72	.01	-.00
.93	1.97	.69	.01	.00
.95	2.20	.53	.01	-.00
.95	1.06	.58	.01	-.00
.95	5.78	.48	-.00	.00

Table 21 Velocity Data for Experiment (II-M-3).

$\eta$	$\theta$	$V_z^+$	$V_\theta^+$	$V_r^+$
.02	.55	.97	-.16	-.04
.19	.38	1.41	.01	-.00
.36	5.13	.42	.00	-.01
.37	2.99	.51	.01	-.04
.40	1.29	.41	.01	.01
.44	1.36	1.83	.06	.05
.48	1.00	.79	.01	.00
.53	5.40	1.03	-.01	.02
.53	5.70	1.22	-.01	.01
.55	5.45	1.12	-.01	.01
.56	.07	1.08	-.00	.01
.57	5.85	1.27	.00	.01
.58	3.93	.71	-.01	-.01
.60	1.70	.63	.02	.01
.60	1.70	.67	.02	.01
.60	4.87	1.09	-.02	-.01
.60	1.26	1.28	.02	.01
.62	5.65	1.58	-.01	.02
.62	4.07	.74	-.02	-.01
.62	5.11	1.09	-.01	.01
.64	.39	1.51	.01	.00
.69	5.35	1.56	-.02	.00
.72	6.28	1.83	.00	.01
.73	3.73	.65	-.03	-.01
.75	5.59	1.78	-.02	.00
.76	.38	2.09	.02	.01
.76	.75	1.88	.02	.02
.78	.55	1.72	.02	.00
.79	4.45	1.24	-.04	-.00
.79	.19	2.17	0.00	0.00
.80	1.90	1.27	.05	-.00
.82	5.74	2.12	-.02	.00
.83	5.69	2.14	-.03	.01
.83	1.57	1.48	0.00	0.00
.84	1.09	1.72	.04	.00
.84	5.87	2.17	.00	.00
.85	1.02	2.01	.04	.01
.85	2.54	.61	.03	-.01
.86	5.39	1.97	-.04	.00
.87	1.01	2.12	.03	.01
.88	.61	1.68	.04	-.01
.89	.65	2.06	.02	.01
.89	6.05	2.16	0.00	0.00
.90	1.91	.82	.04	.00
.91	5.99	1.65	-.01	.00
.91	4.06	1.92	-.11	-.02
.96	.48	.69	.01	.00

.97	.21	2.23	0.00	0.00
.97	.35	2.10	.02	.02
.97	2.98	.49	-.03	-.00
.07	.61	.93	.02	.01

Table 22 Velocity Data for Experiment (III-M-1).

$n$	$\theta$	$V_z^+$	$V_\theta^+$	$V_r^+$
.05	2.82	.69	.01	-.14
.14	5.66	.66	.02	.02
.16	5.36	.75	.03	.01
.18	4.89	.11	.06	-.01
.19	5.93	.70	.02	.03
.19	4.29	.81	.03	-.02
.19	1.74	.66	-.01	.01
.19	5.32	.77	.03	.01
.23	5.60	.72	.02	.02
.24	2.01	.75	-.00	-.03
.26	.66	.65	-.00	.02
.27	.70	.57	-.00	.03
.29	1.91	.65	.00	-.01
.30	1.47	.62	.00	.00
.31	4.92	.70	.01	-.00
.33	5.39	.66	.01	.01
.35	3.10	.79	.00	-.03
.36	1.98	.65	.01	-.01
.37	3.90	.94	.01	-.03
.43	5.82	.65	-.00	.02
.44	2.15	.78	.02	-.01
.44	1.90	.75	.01	-.00
.47	2.06	.80	.02	-.00
.48	4.81	.77	-.01	-.00
.48	.72	.68	.00	.01
.62	2.57	1.11	.03	-.01
.65	5.00	1.20	-.02	-.00
.65	1.52	1.40	-.02	.00
.65	1.47	1.46	.03	-.00
.66	2.97	.84	.01	-.00
.66	4.05	1.07	-.01	-.01
.67	3.14	.72	-.00	-.00
.68	4.67	1.16	-.02	-.00
.71	.98	1.66	.02	.00
.71	.98	1.59	.02	.00
.71	4.93	1.40	-.02	-.00
.73	.20	1.65	-.00	.01
.75	1.57	1.42	0.00	0.00
.75	3.10	.63	.01	-.01
.75	.21	.10	.01	-.00
.75	.37	1.74	.01	.00
.77	2.83	.77	.02	-.00
.78	.68	1.51	.01	.00
.78	1.06	1.17	.02	.00
.80	1.19	1.32	.02	.01
.81	1.91	1.06	.03	-.00
.81	.10	1.75	0.00	0.00

.82	.88	1.10	.01	-.01
.83	2.95	.60	0.00	0.00
.86	.34	1.64	.02	.01
.86	1.05	1.09	.01	.00
.87	.64	.96	.01	-.00
.81	4.60	1.10	-.02	-.01
.94	5.63	.80	-.01	.00

Table 23 Velocity Data for Experiment (III-M-2).

n	$\theta$	$V_z^+$	$V_\theta^+$	$V_r^+$
.09	2.60	1.08	-.02	-.02
.26	2.62	1.08	-.00	-.02
.37	2.54	1.11	-.00	-.01
.37	1.88	.98	.00	-.01
.42	5.02	.93	.00	.00
.47	3.93	1.27	-.01	-.02
.49	.23	.97	-.00	.01
.49	2.08	1.11	.02	-.00
.52	5.54	1.07	-.02	-.00
.52	.55	.95	-.01	.02
.63	.44	.96	-.00	.01
.65	5.03	1.44	-.01	-.00
.69	1.22	1.43	.01	-.00
.72	4.56	1.17	-.01	-.01
.75	5.15	1.35	-.01	-.01
.76	4.06	.90	-.00	-.00
.78	1.47	1.02	.01	-.00
.83	.64	1.29	.02	.00
.83	1.03	1.25	.01	.00
.85	2.17	.66	0.00	0.00
.85	5.62	1.16	-.01	-.01
.85	3.71	.67	.00	.00
.85	.84	1.08	.01	-.00
.86	.71	1.16	.01	.01
.86	5.23	1.09	-.01	.00
.86	2.49	.85	.00	-.00
.86	.92	1.06	0.00	0.00
.86	1.17	1.28	.02	-.01
.87	2.73	.74	.01	-.00
.87	2.77	.75	.01	-.00
.89	4.97	.91	-.00	-.00
.89	1.75	1.00	.02	.00
.89	1.79	.75	.01	-.00
.90	5.42	.94	-.00	-.00
.90	2.26	.82	.01	-.01
.92	6.13	.96	-.01	.00
.94	.98	1.05	.01	.00
.95	2.97	.44	0.00	0.00
.95	5.96	.77	-.01	.00
-0.00	5.96	.77	-.01	.00

Table 24 Velocity Data for Experiment (III-M-3).